

PhD. 27599

**Shock and ballistic properties of bainitic steels  
and tungsten alloys**

Ruth Hammond  
Churchill College



This dissertation is submitted for the degree of Doctor of Philosophy

June 2004



When asked for the ideal armour for a particular situation, a well-known Professor queried "what is the range of the missile". Upon hearing the range was 14 km, he replied "I would recommend 14.1 km of air".

## Acknowledgements

This dissertation is based on research that I carried out in the Physics and Chemistry of Solids Group at the Cavendish Laboratory, Cambridge, between October 2001 and June 2004 under the supervision of Professor John E. Field and Dr William G. Proud. Both of whom have provided unerring support and guidance; this research would not have been possible without either of them.

I acknowledge both financial support and supply of materials from QinetiQ, Farnborough. P. M. Brown, D. Baxter and T. D. Andrews of QinetiQ, Farnborough and I. G. Cullis and P. D. Church of QinetiQ, Fort Halstead provided invaluable support over the course of this research. It has provided a great opportunity to work with very experienced researchers from an industrial background in contrast to the very academic environment that I, myself am more familiar with.

F. Clarke and M. Vickers of Materials Science and Metallurgy at the University of Cambridge are thanked for their technical help. D. L. A. Cross, R. Marrah, R. Flaxman and other members of the Mott workshop at the Cavendish Laboratory provided valuable technical support. The electronics department, especially H. Thompson were essential to much of this research. TWI were very helpful, offering use of their x-ray equipment, J Blunt of the Cavendish was invaluable in being able to operate it for me. D Townsend, of BAe Systems, was extremely generous, providing me with samples to cover a shortfall at the end of this research. Professor H. K. D. H. Bhadeshia is thanked for his comments on the research. I would also like to thank the Newton Trust for their grant.

On a more personal level, I am very grateful to all the emotional support that I received over this period of my life. My brother, David, has been a great person to bounce ideas off, members of the Fracture Group who have made the day to day experience of studying for a Ph.D. pleasurable and of course to my fiancé, Austin for his continuous support.

This dissertation is the result of my own work and includes nothing which is the outcome of work done in collaboration, except where specifically indicated in the text. This dissertation does not exceed the word limit of 60 000 words.

Ruth Hammond

Ruth Hammond  
June 2004

This dissertation is the result of my own work and includes nothing which is the outcome of work done in collaboration, except where specifically indicated in the text. This dissertation does not exceed the word limit of 60 000 words.

Ruth Hammond

Ruth Hammond  
June 2004

## **Abstract**

This dissertation reports the shock and ballistic properties of a selection of bainitic steels. In order to attain these data a number of experimental techniques were developed and the dynamic properties of two sintered tungsten alloys were measured.

The shock properties of the two bainitic steels considered in this research were found to be similar, there were however some important differences. Whilst the upper bainitic samples were recovered either whole or in a few fragments, the lower temperature bainite exhibited a great deal of brittle fracture. A very interesting difference was that while the ferrite in the lower temperature bainite underwent a pressure induced phase transition at 13 GPa as would be expected in a low alloy steel, the upper bainite did not appear to. Whether the phase transition has in fact been suppressed or so fast as to be non-observable is discussed in this dissertation. Given the only difference between these two alloys is microstructural, this must be the overriding factor in whether this characteristic transition is observed.

Using both classic and symmetric Taylor tests, two sintered tungsten alloys were characterised, remarkably, tensile surface strains of almost 5 % were recorded. These materials are under consideration as an environmentally friendly penetrator material, a replacement for the depleted uranium currently used, making them ideal projectile material for this study of the ballistic properties of potential and current armour steels.

Ballistics experiments were performed in order to compare one of the bainitic steels with both an existing armour steel and also to mild steel using tungsten penetrators. The existing armour steel exhibited a 'plugging' behaviour. The bainitic steel failed by a combination of the 'plugging' mechanism and fragmentation.

The bainitic steels under consideration in this research are potential replacements for the current more expensive steels that are used on armoured vehicles. Whilst this study does not try to conclude whether they do in fact offer more protection than existing products to such vehicles, it does provide sufficient data for modellers to help make informed decisions.

## Contents

1. Introduction	9
1.1 Fundamentals of shock wave physics	
1.2 Taylor impact test	
1.3 Penetration and perforation/ballistic studies	
1.4 Conclusion	
References	
2. Materials	45
2.1 Bainitic steels	
2.2 Tungsten alloys	
2.3 Rolled Homogeneous Armour (RHA) Steel	
References	
3. Experimental techniques	56
3.1 Determination of static properties	
3.2 The Cambridge impact facility	
3.3 Stress measurements	
3.4 Strain measurements	
3.5 VISAR (Velocity Interferometer System for Any Reflector)	
3.6 High-speed photography	
3.7 The small gas gun	
3.8 Microstructural studies	
References	
4. Shock properties of bainitic steels	81
4.1 Measurement of static properties	
4.2 Measurement of the Hugoniot	
4.3 Lateral stress measurement and calculation of shear strength	
4.4 Spall strength	
4.5 Recovered debris	
4.6 Microstructural studies	

4.7 Conclusions	
References	
5. Ballistic properties of bainitic steels	106
5.1 Impacts on free plates	
5.2 Depth of penetration studies	
6. Taylor impact of tungsten alloys	124
6.1 Experimental	
6.2 Results and discussion	
6.3 Conclusions	
References	
7. Technique Development	145
7.1 Dependence of measured lateral stress on thickness of protective “padding” around gauges	
7.2 Does this protective “padding” actually improve the survivability of lateral gauges?	
References	
8. Conclusions and further work	153

## Chapter 1

### Introduction

Materials have been tested for many years, however, much of this early work is not relevant to fast loading conditions. Impulsive loading needs to be considered in many applications including structural strength of vehicles during crash situations, lightweight armour for personnel or military vehicles, aero-engines and spacecraft. As impact situations arise under diverse conditions, there is a need for this to be reflected in the materials selection and design process. To do this effectively, it is necessary to understand material response under high stress loading. As is evident from figure 1.1, the physical properties of a material can be highly dependent upon the strain rate and loading conditions to which they are subjected.

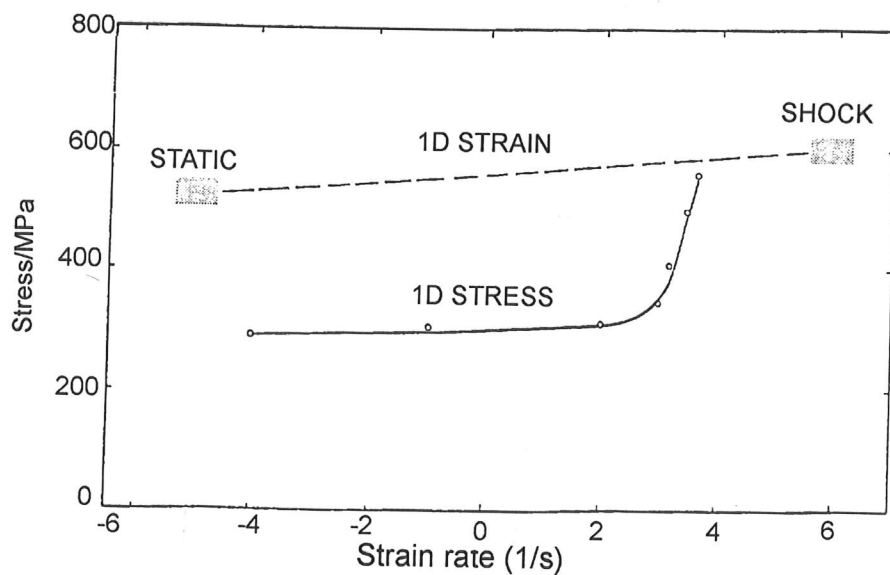


*Figure 1.1* A plot of failure stress of limestone both as a function of strain rate and loading state, taken from (Brace and Jones 1971). The upper line represents the stress at a strain value of 0.7 %, being 1-dimensional strain the sample is laterally constrained. The lower line is for experiments carried out under uniaxial stress.

The differences between uniaxial stress and strain need to be considered in order to understand the results of the research presented in this dissertation.

Plate impact experiments lead to conditions of uniaxial strain. The diameter of the plate is large compared to its thickness, the material is constrained laterally. The stress can therefore increase regardless of the yield stress. An idealised stress-strain plot of

final states would take the form shown in figure 1.2. Generally for metals, the bulk modulus increases when the material is subjected to greater pressures (refer to section 3.1). Higher stress increments travel faster and will overtake the lower ones. A single 'discontinuous' shock front is formed. Refer to section 1.1 for a detailed discussion of shock waves.

Uniaxial stress conditions considered in this research occur when a slender rod, length to diameter ratio of 10:1, impacts normally. Under these conditions, the material is not constrained laterally which leads to a triaxial strain state. When the length of the loading pulse is long compared to the rod diameter, the direction of wave propagation is the only stress component that needs be considered. Refer to figure 1.2 for a typical loading path.

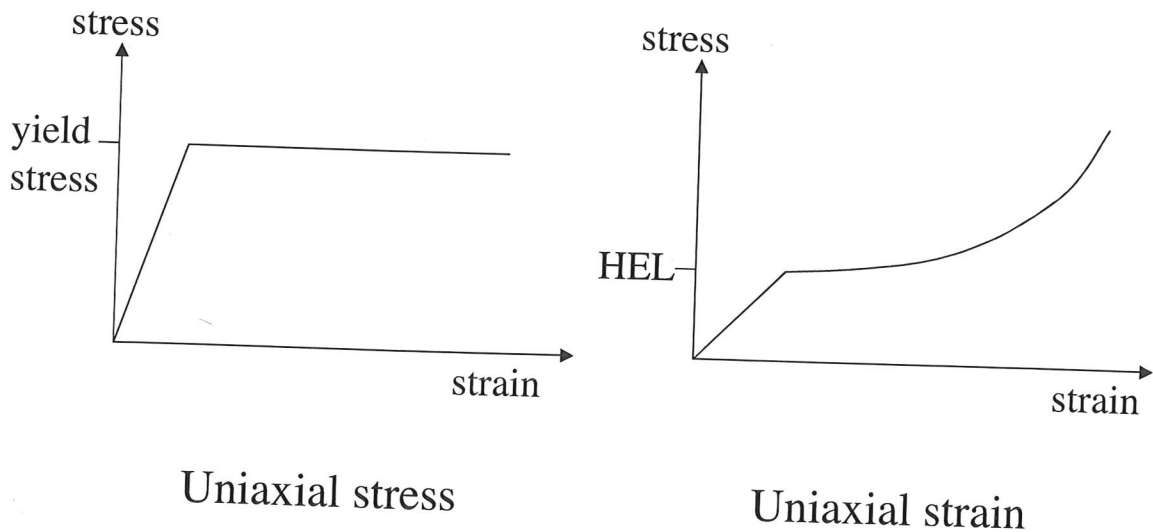


**Figure 1.2** Schematic for idealised loading path for uniaxial stress and path of final states for uniaxial strain. The Hugoniot Elastic Limit (HEL is discussed later in this chapter.

Much of the fundamental data recorded in this research are invaluable to modellers. By measuring the behaviour of a material in a relatively simple situation such as in shock experiments, a combination of analytical and hydrocode models have been able to predict the behaviour of materials in more complex situations. This is, of course, very important when considering how an armoured vehicle would behave if it were to be protected by a combination of materials including bainitic steels.

The main subjects of this dissertation are the shock and ballistic properties of a selection of bainitic steels that are described in chapter 2. These can be made relatively cheaply due to their low alloy composition and yet potentially will be able to be at least as good as conventional armour steels. Armour materials need to be tested and modelled in both shock and ballistic situations due to the nature of their potential practical use.

This dissertation, for clarity, will begin with a discussion of both the relevant theory and materials used; chapters 1 and 2 respectively. Chapter 3 outlines the experimental techniques used, in order to circumvent repetition in the ensuing chapters. A discussion of the shock properties of two of the bainitic steels is to be found in chapter 4. This covers longitudinal and lateral stress measurements, calculated shear stresses and dynamic tensile strength measurements. It is based on a paper that has been accepted for publication in Proceedings A of the Royal Society (Hammond 2004).

Chapter 5 presents the ballistic research carried out on a bainitic steel and compares its response to other steels. In order to examine the ballistic properties of bainitic steel it was necessary to carry out extensive characterisation of the impactor material, a sintered tungsten alloy. Two different alloys were tested in Taylor tests, both classic and symmetric geometries and these are discussed in chapter 6, which is based on (Hammond et al. 2003a).

In order to carry out much of this research, there were inevitably various preparatory experiments that were carried out. These include studying the effect of padding around gauges (Hammond et al. 2003b), examining the stress measured and also the survivability of the gauge. These data are presented in chapter 7.

Studying both the shock and ballistic properties of a material leads to both an understanding of, and an ability to model how it behaves, across a wide range of strain rates. Shock experiments provide a simple, initially one-dimensional, geometry in which to study material response to high stress and high strain rates. It provides good input parameters for relatively simple models. These models can then be

extended to predict more complex situations such as those encountered in ballistics experiments. These ballistic experiments provide an opportunity to study three dimensional problems. In order to model these precisely however, the parameters have to be found very accurately. The Taylor tests provide lower strain rate regimes in which to gain data. By studying a variety of strain rates, modellers can predict material behaviour in all types of situations. If the tungsten alloys considered in this research are to be used as an environmentally friendly replacement for depleted uranium penetrators, then it is, of course, essential to predict their behaviour once incorporated in a complicated long rod system. This would not be possible without both the experimental data and modelling.

A basic review of the theory of shock wave physics and ballistic impact is presented in the remainder of this chapter. Firstly, the shock experiment is discussed. This provides a means of subjecting a material to one-dimensional strain at strain rates of up to  $10^8 \text{ s}^{-1}$ . Secondly, Taylor tests are considered. These provide large stress and large strain tests at strain rates of up to  $10^5 \text{ s}^{-1}$ . Finally, some of the ideas behind ballistics experiments are explained. These experiments are ideal for studying the behaviour of materials from quasi-static to the shock regime. Studying both the shock and ballistic properties of a material leads to an understanding of how it behaves across a wide range of strain rates. Those readers already familiar with shock and ballistic physics may choose to proceed directly to chapter 2.

## 1.1. Fundamentals of shock wave physics

### Shock waves

A shock wave is a front across which a discontinuous change in density, pressure, particle velocity, temperature, energy and entropy is found. At these stress levels, wave speed increases with stress so a ramped wave will steepen until a shock wave forms. In a real material, effects such as viscosity and the finite speed of deformation cause the wave to have a finite rise time.

### Release waves or release fans

These take the material from the high-pressure state to ambient conditions. A release wave, which is isentropic, removes the increments of stress and can be considered as a collection of wavelets. The release wave is dispersive, as the wave-speed reduces with pressure. As the wave propagates it spreads, consequently release waves are not discontinuous and must be treated differently from shocks. They are sometimes referred to as release fans. Since they propagate through stressed material, they can travel faster than the primary shocks.

### Jump relations

The variables used are

$u_p$  (mm  $\mu\text{s}^{-1}$ ), the particle velocity, which defines the motion of the particles such as atoms in the material.

$U_s$  (mm  $\mu\text{s}^{-1}$ ), the shock velocity, the velocity at which the shock moves through the material.

$\rho$  (g  $\text{cm}^{-3}$ ) is the density of the material.

$\sigma$  (GPa) is the stress in the direction of propagation of the shock.

$e$  (J  $\text{g}^{-1}$ ) is the energy stored in the material per unit mass.

In the analysis of shock waves it is important to remember that mass, momentum and energy are conserved across the shock front. The passage of a shock wave through a material leads to adiabatic compression. It is possible to write relations between changes in the thermodynamic variables. Such relations, while important, yield no information about the material or the shock structure; they only give the ultimate

## 1.1. Fundamentals of shock wave physics

### Shock waves

A shock wave is a front across which a discontinuous change in density, pressure, particle velocity, temperature, energy and entropy is found. At these stress levels, wave speed increases with stress so a ramped wave will steepen until a shock wave forms. In a real material, effects such as viscosity and the finite speed of deformation cause the wave to have a finite rise time.

### Release waves or release fans

These take the material from the high-pressure state to ambient conditions. A release wave, which is isentropic, removes the increments of stress and can be considered as a collection of wavelets. The release wave is dispersive, as the wave-speed reduces with pressure. As the wave propagates it spreads, consequently release waves are not discontinuous and must be treated differently from shocks. They are sometimes referred to as release fans. Since they propagate through stressed material, they can travel faster than the primary shocks.

### Jump relations

The variables used are

$u_p$  ( $\text{mm } \mu\text{s}^{-1}$ ), the particle velocity, which defines the motion of the particles such as atoms in the material.

$U_s$  ( $\text{mm } \mu\text{s}^{-1}$ ), the shock velocity, the velocity at which the shock moves through the material.

$\rho$  ( $\text{g cm}^{-3}$ ) is the density of the material.

$\sigma$  (GPa) is the stress in the direction of propagation of the shock.

$e$  ( $\text{Jg}^{-1}$ ) is the energy stored in the material per unit mass.

In the analysis of shock waves it is important to remember that mass, momentum and energy are conserved across the shock front. The passage of a shock wave through a material leads to adiabatic compression. It is possible to write relations between changes in the thermodynamic variables. Such relations, while important, yield no information about the material or the shock structure; they only give the ultimate

equilibrium state of the material, not the pathway. In this section, everything is considered in a laboratory frame of reference where the subscripts  $0$  and  $1$  denote the undisturbed and shocked materials respectively.

If we consider the simplest scenario of an isotropic material with negligible strength compared to the shock wave, i.e. hydro-dynamic behaviour, we can examine the basic response of the material.

Considering a steady shock travelling at speed  $U_s$  traversing a material which is initially stationary ( $u_p = 0$ ) with density  $\rho_0$ . The amount of material,  $M$ , crossed by *unit area* of the shock wave per unit time is

$$M = \rho_0 U_s. \quad (1.1)$$

Conservation of mass requires that material emerges at the same rate behind the shock front;

$$\rho_0 U_s = \rho_1 (U_s - u_1), \quad (1.2)$$

which is the mass jump relation.

The pressure difference across the shock front leads to a change in momentum which, by Newton's second law, the jump relation is

$$\rho_0 U_s u_1 = P_1 - P_0. \quad (1.3)$$

The energy rise is assumed to be in two parts, kinetic ( $KE$ ) and internal ( $e_1 - e_0$ ). The  $KE$  change is entirely due to the change in particle velocity in the mass of material which has been accelerated.

$$KE = \frac{1}{2} \rho_0 U_s (u_1)^2. \quad (1.4)$$

Adding this to the change in internal energy gives the total energy change which is equal to the amount of work done on the shock,  $W$ , where  $W$  is calculated as force multiplied by distance.

$$W = \rho_0 U_s \left( \frac{1}{2} u_1^2 + e_1 - e_0 \right) = P_1 u_1. \quad (1.5)$$

By substitution of equations (1.2) and (1.3) into (1.5) the energy jump relation is obtained

$$e_1 - e_0 = \frac{1}{2} (P_1 - P_0) (V_0 - V_1). \quad (1.6)$$

Given the three conservation relations contain only five variables, knowledge of two of them will define the other three.

### The Hugoniot

When combined with an equation of state, where energy is expressed as a function of both pressure and volume, and relevant boundary conditions a Hugoniot curve results. Such a curve describes the possible *end states*, *not the pathway*, resulting from a single shock on material in a given initial state. It also represents the material under high-rate compressive loading and so can be used to measure the compressive strength; shear and tensile strength will be discussed later.

For an impact between two materials of known Hugoniots at a given impact velocity, the values of the thermodynamic variables can be defined. Plotting any shock parameter against any other would lead to a unique curve for a particular material, the most common Hugoniot plots are  $P$  vs.  $u_p$ ,  $U_s$  vs.  $u_p$  or  $P$  vs.  $V$ . The first of which is used extensively in this dissertation because they are variables that have to be conserved at a shock interface whether or not it is discontinuous itself.

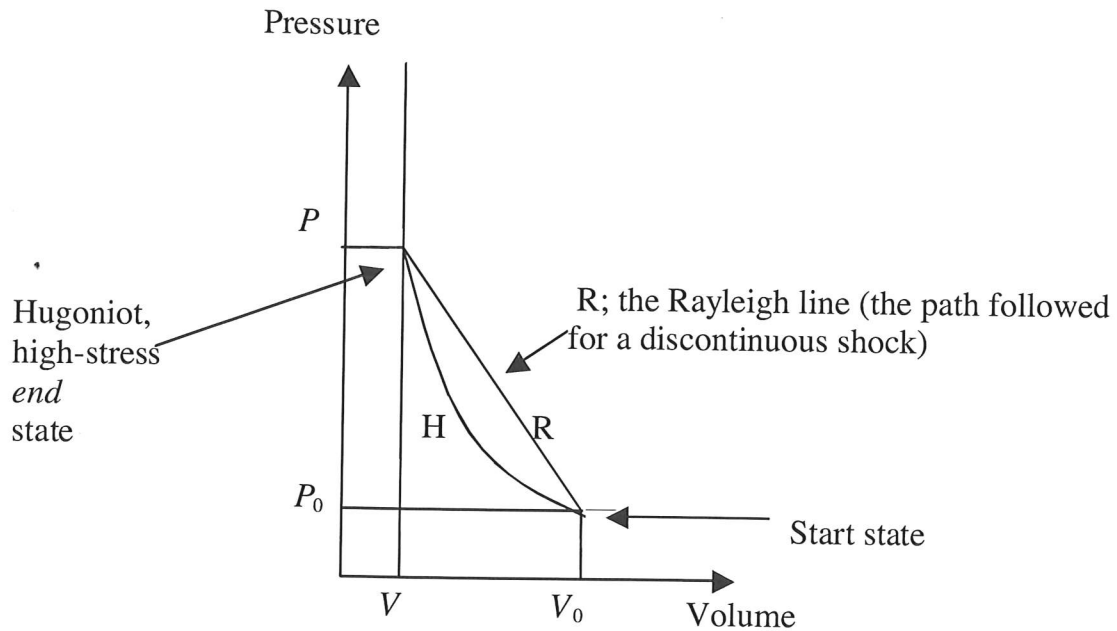


**Figure 1.1.1** A schematic  $P$ - $V$  Hugoniot,  $H$ , for shock pressure  $P$ . The loading line,  $R$ , in the material is the Rayleigh line.

Figure 1.1.1 shows a schematic  $P$  versus  $V$  Hugoniot, labelled  $H$ . This curve is concave, reflecting the assumption that wave speed increases with pressure. Loading occurs along a chord, the Rayleigh line  $R$ , to this curve starting at the initial state and finishing at the final state. The Rayleigh line is not a thermodynamic path but is obtained from the conservation of mass and momentum. The slope of this chord in the  $P$ - $V$  plane can be found by rearranging equations (1.3) and (1.5), (1.6)

$$U_s = V_0 \sqrt{\frac{P - P_0}{V_0 - V}} \quad (1.7)$$

Hence the slope of the Rayleigh line in the  $P$ - $V$  plane is proportional to the square of the shock impedance ( $\rho_0 U_s$ ).

Figure 1.1.2 shows four Hugoniots which differ only in direction of shock and initial particle velocity. The figure is a schematic showing four different representations of the same Hugoniot in the  $P$ - $u_p$  plane.  $H_2$  is the principal Hugoniot (taken at standard conditions; RTP) centred on an initial particle velocity of zero and moving to the right.  $H_1$  is for an identical shock in the opposite direction,  $H_4$  is the Hugoniot for a

shock moving into a material which is already moving, so it is a translation of  $H_2$  along the  $u_p$  axis.  $H_3$  is shock moving in the opposite direction travelling into a material which is already moving. The fact that such translations and reflection of Hugoniot along the  $u_p$  axis are valid is a result of the fact that an isotropic material's response is not dependent on the direction of the shock.

Empirically Hugoniot have been expressed in the form

$$U_s = c_0 + Su_p + Qu_p^2 + \dots \quad (1.8)$$

where  $c_0$  is the bulk sound speed.

$S$  and  $Q$  can be found by a least squares method on the data (Marsh 1980). It should be noted that in general the second order term in  $U_p$  is only necessary when phase transitions occur.

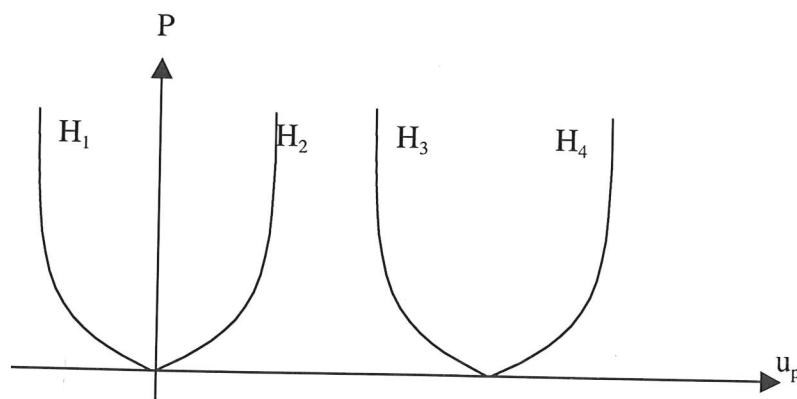


*Figure 1.1.2 Schematic showing four different representations of the same Hugoniot in the  $P-u_p$  plane.*

### Calculating pressure and particle velocity during an impact

The stress and particle velocity resulting from an impact between two materials can be calculated using their Hugoniot. This is most easily done graphically, as shown in figure 1.1.3.

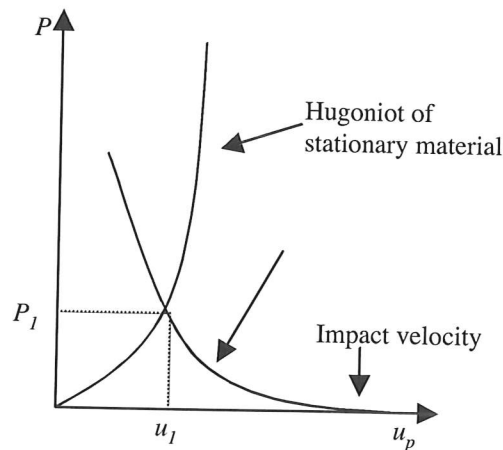


**Figure 1.1.3** Graphical means of calculating the pressure and particle velocity at an impact between two materials.

The stationary material has its velocity increased and the impactor is slowed to a lower velocity. The pressure and particle velocity at impact are those defined by the intersection of the two Hugoniot, at  $P_I, u_I$ . The loading paths in the two materials are chords joining the initial state of the material and the final state. Two materials in contact cannot maintain a stationary discontinuity in either pressure or particle velocity, waves would be created to carry the discontinuity away leaving behind a region of constant pressure and particle velocity irrespective of material boundaries. In order to conserve mass and momentum, it is therefore necessary that there must be continuity in pressure and particle velocity at the impact plane, ie. at the intersection of the two Hugoniot. Other shock parameters can now be calculated using the jump relations discussed earlier.

### Real Hugoniot

Above a certain stress, the Hugoniot Elastic Limit (HEL), the material no longer behaves elastically. The effect is that the shock loads up via two Rayleigh lines, as the gradients are different this implies the wave velocity is different. Therefore two waves are produced whose velocities are dependent on the slopes of the Rayleigh lines (refer to figure 1.1.4). The waves separate if the velocity of the elastic wave is greater than that of the plastic. Some materials exhibit a phase transition, so above the stress that causes the transition a third wave may be observed (figure 1.1.5).

Iron being a prime example of this (Barker and Hollenbach 1974), at the phase transition stress the body-centred-cubic ferrite transforms into hexagonal-close-packed  $\epsilon$  by a martensitic (rapid, diffusionless) transformation.

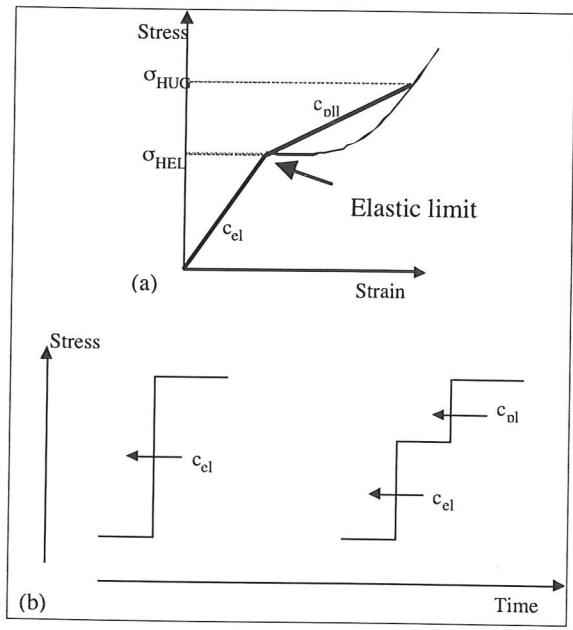


**Figure 1.1.4** (a) Two wave structure. (b) Splitting of shock front into two waves, elastic and plastic as time progresses. Where,  $c_{el}$  is the speed of the elastic part of the wave and  $c_{pl}$  that of the plastic.

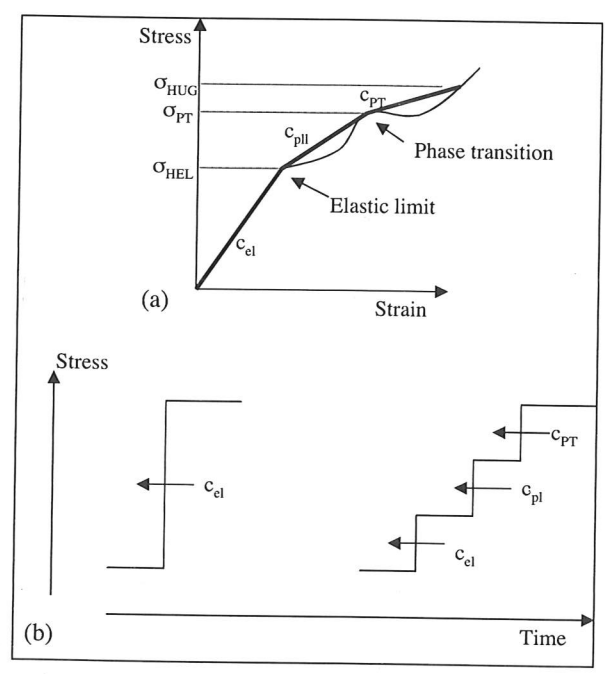


**Figure 1.1.5** (a) Three wave structure. (b) Splitting of shock front into three waves, elastic, plastic and phase transition, as time progresses. Where,  $c_{PT}$  is the speed of the phase transition wave.

Iron being a prime example of this (Barker and Hollenbach 1974), at the phase transition stress the body-centred-cubic ferrite transforms into hexagonal-close-packed  $\epsilon$  by a martensitic (rapid, diffusionless) transformation.

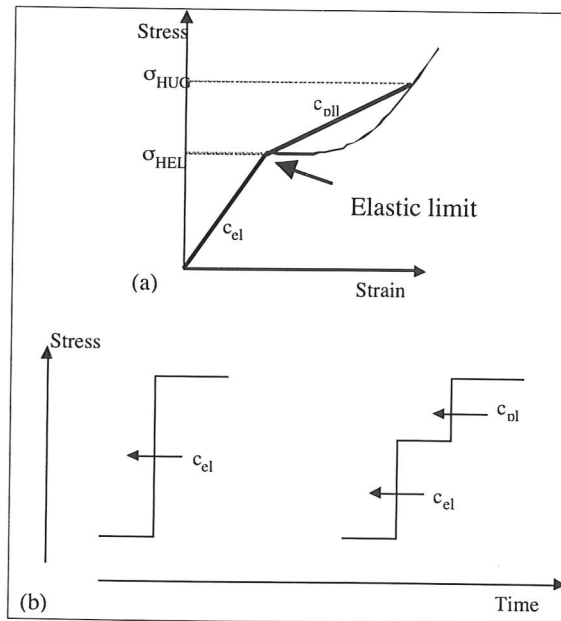


**Figure 1.1.4** (a) Two wave structure. (b) Splitting of shock front into two waves, elastic and plastic as time progresses. Where,  $c_{el}$  is the speed of the elastic part of the wave and  $c_{pl}$  that of the plastic.

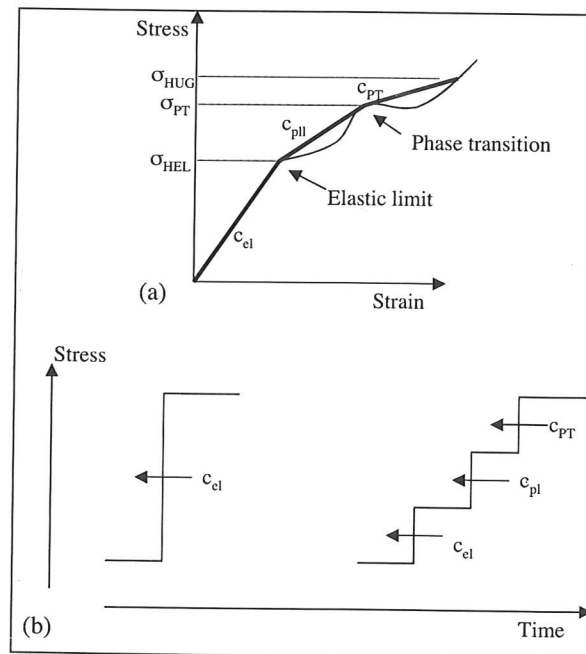


**Figure 1.1.5** (a) Three wave structure. (b) Splitting of shock front into three waves, elastic, plastic and phase transition, as time progresses. Where,  $c_{PT}$  is the speed of the phase transition wave.

### Lateral Stress and Shear Strength

If the lateral stress,  $\sigma_y$ , is also measured under the same impact conditions as the longitudinal stress,  $\sigma_x$ , then the shear strength,  $\tau$ , can be calculated.

$$2\tau = \sigma_x - \sigma_y = Y, \quad (1.9)$$

where  $Y$  is the yield strength of the material.

For an elastic material,

$$\sigma_y = \frac{\nu}{1-\nu} \sigma_x, \quad (1.10)$$

where  $\nu$  is the Poisson's ratio of the material.

Substituting into equation (1.9) gives

$$2\tau = \frac{(1-2\nu)}{(1-\nu)} \sigma_x. \quad (1.11)$$

This can be plotted as a comparison to the experimental data.

### Dynamic tensile strength

When determining the dynamic properties of a material, the dynamic tensile or spall strength is frequently measured. Much of the work in this field is summarised in review articles (Davison and Graham 1979; Grady 1988).

The spall strength is the dynamic tensile strength of a material at high strain rates. It is most commonly encountered in plate impact and explosive loading scenarios. The spall strength of the material is taken from a stress pulse measured by a gauge, usually embedded in a back surface configuration, or from a VISAR (Velocity Interferometer

System for Any Reflector, discussed in section 3.5) trace. In either case the signal has the form shown below. The value taken for the spall strength ( $\sigma_{spall}$ ) is indicated in the figure 1.1.6.

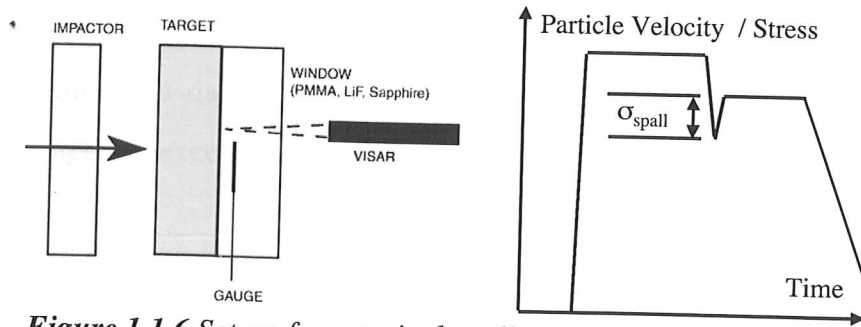


**Figure 1.1.6** Set-up for a typical spall experiment (left) and a schematic of an ideal trace (right).

The following description shows how spall strength can be related to the Hugoniot of the material and explains why the so called "pull-back" signal can be used as the measure of this parameter.

It is assumed that the Isentrope and the Hugoniot are straight lines. Secondly, at low stress levels they follow the same path. The x-t diagram for the experiment is shown in figure 1.1.7.

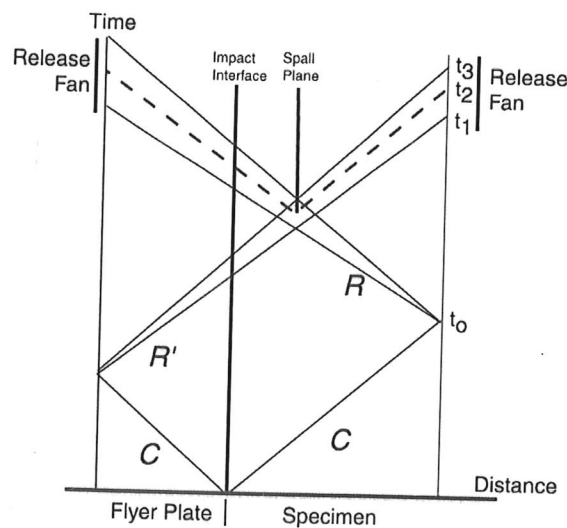


**Figure 1.1.7** A wave diagram for the spall process.

The release fans from R and R' combine in one of three cases:

- (i) where the material is taken to peak tension but  $\sigma_{spall}$  is not exceeded

- (ii) spall occurs
- (iii) the material has no spall strength

Spall is initiated by nucleation of voids or cracks or by existing microstructural defects. These defects continue to grow until they coalesce forming a spall plane. The kinetics and damage growth mechanisms can be such that the dynamic tensile strength far exceeds the quasi-static tensile strength.

There have been many attempts at modelling including attempts based on void growth (Johnson 1981; Johnson et al. 1995; Roy et al. 2002) and crack-straining based models (Chen et al. 1997). In both cases it was concluded that a two-stage model was required in which void nucleation is also considered. Calculations behind void nucleation, growth and coalescence are reviewed in (Curran et al. 1987). Two well established codes are CHARADE and DYNA-2D. CHARADE involves ductile growth and coalescence of voids, examples of its use are found in (Tonks et al. 1999) and (Murray 1996). DYNA-2D has also been compared favourably with experimental results, for example in (Church et al. 2001).

## 1.2 Taylor impact test

The classic Taylor test is a high-strain, high-strain-rate experiment first suggested by G. I. Taylor (1948a) as a way to measure the dynamic yield strength of a material at a strain rate of  $\sim 10^5 \text{ s}^{-1}$ . This value was known to be substantially more than the static yield strength. By impacting a rod of the material in question onto a 'rigid, semi-infinite' anvil and measuring the length of the deformed section, the yield stress can be calculated. More sophisticated methods such as plate impact have since been used widely, however recently the Taylor impact experiment has regained importance with the acquisition of time-resolved data through high-speed photography. This allows the propagation of the plastic wave to be observed and the formation of any secondary features due to work hardening.

The introduction of the 'symmetrical' Taylor test in which a rod is impacted onto an identical rod removes the problems of frictional elastic constraint at the projectile/target interface and also minimised the problems caused by a lack of a perfectly rigid target (Erlich and Shockey 1983). In effect the rigid condition is achieved in the centre-of-mass frame with a corresponding impact velocity of  $V/2$ . However this inevitably adds experimental difficulties in aligning the rods laterally and ensuring a normal impact. If a sabot is used then possibilities of asymmetry effects between the two rods (Walley et al. 2000; Radford et al. 2002) are introduced if the timescale of interest is sufficiently long.

The Taylor test can be instrumented with stress or strain gauges and VISAR can also be used on the rear surface. The development of high-speed photography has allowed the observation of intermediate deformation profiles. Hence a great deal of data can be found in the high-strain, high-strain-rate regime, this kind of test is therefore ideal for validation of constitutive material modelling.

Consider a cylindrical projectile, initial length  $L$ , with flat ends, which are perpendicular to the cylinder's axis, impacting a flat rigid target at time,  $t=0$ . The stress at the impact end will immediately rise to the elastic limit,  $\sigma_{yield}$ , and an elastic compression wave propagates at the elastic wave velocity in a rod,

$c_R = (E/\rho)^{1/2}$  (Bancroft 1941), into the cylinder, where  $E$  is the Young's modulus and  $\rho$  is the density of the material. If the impact conditions lead to a sufficiently high stress, a plastic wave propagates from the impact site at a velocity, which is less than that of the elastic wave.

Material which has been subjected to the elastic wave but not the plastic one is under stress,  $\sigma_{yield}$  with a particle velocity of  $(V - \sigma_{yield} / \rho_P c)$ , where  $\rho_P$  is the projectile's density,  $V$ , is the impact velocity and  $c$  is the elastic wave velocity ( $c_R$  in this case). The rod is therefore decelerated. Upon reaching the rear end of the projectile, the elastic wave is reflected as a tensile wave. This reflection results in a change in velocity of the free end of  $2\sigma_{yield} / \rho_P c$ , where  $\rho_P$  is the density of projectile material, while material that this tensile wave has passed is at zero stress and has particle speed of  $(V - 2\sigma_{yield} / \rho_P c)$ .

When this reflected elastic wave meets the oncoming plastic wave, it is reflected as a compression wave. This process is repeated until the plastic front has ceased to travel through the material. When the elastic wave meets the plastic wave for the first time, the distance moved from the target by the plastic wave is  $h$ . At this point in time the undeformed length is  $x$ , the total length of the rod  $l = x + h$ . For the final state the undeformed length is defined as  $X$ , the final rod length is  $L_f$ , the initial length of the rod is  $L$ , the plastic front speed is  $v$ .

Let  $dt$  be the time needed for the elastic wave to travel to the rear surface and back to the plastic wave,

$$dt = \frac{2x}{c_R}. \quad (1.12)$$

Consider small changes in  $h$ ,  $u$  and  $x$  during  $dt$ . The plastic wave moves  $vdt$  along the rod.

$$dh = \frac{v2x}{c_R}. \quad (1.13)$$

For such a double transit the elastic rear part of the rod is decelerated, the particle velocity is decreased by

$$du = -\frac{2\sigma_{yield}}{\rho_p c_R}, \quad (1.14)$$

where  $\rho_p$  is the density of the projectile.

Let  $dx$  be the element of the rod that passes the elasto-plastic boundary during time  $dt$ . Hence we have

$$dx = -(u + v)dt = -(u + v)\frac{2x}{c_R}. \quad (1.15)$$

For a complete analysis of the dynamics, it would be necessary to have knowledge of all the intermediate states of the rod. Taylor however had information prior to and post impact only. Using some simplifying assumptions, it was possible to calculate an approximate value for the dynamic yield strength. Taylor assumed that the elasto-plastic boundary had a constant velocity,  $v=c_{pl}$ , throughout the impact event.

From equations 1.14 and 1.15,

$$\frac{du}{dx} = \frac{\sigma_{yield}}{\rho_p x(u + c_{pl})}, \quad (1.16)$$

which may be integrated to give

$$\frac{\sigma_{yield}}{\rho_p} \ln\left(\frac{x}{L}\right) = \frac{1}{2}u^2 + c_{pl}u - \frac{1}{2}V^2 - c_{pl}V. \quad (1.17)$$

When the rod comes to rest,  $u=0$  and  $x=X$ , giving

$$\frac{\sigma_{yield}}{\rho_p} \ln\left(\frac{X}{L}\right) = -\frac{1}{2}V^2 - c_{pl}V. \quad (1.18)$$

Rearrangement gives

$$\frac{\sigma_{yield}}{\rho_p V^2} = \frac{1/2 + c_{pl}/V}{\ln(L/X)}. \quad (1.19)$$

Assuming the rear face of the projectile decelerates uniformly, the time of deceleration,  $T$ , is equal to the length of the plastically-deformed section of the rod divided by the plastic wave speed,

$$T = \frac{(L_1 - X)}{c_{pl}} = \frac{2(L - L_1)}{V}. \quad (1.20)$$

So that,

$$\frac{c_{pl}}{V} = \frac{L_1 - X}{2(L - L_1)}. \quad (1.21)$$

Substituting in for  $c_{pl}$  gives,

$$\frac{\sigma_{yield}}{\rho_p V^2} = \frac{L - X}{2(L - L_1)} \frac{1}{\ln(L/X)}, \quad (1.22)$$

which was Taylor's original expression.

It is difficult to define the elasto-plastic boundary in the rod from outer dimensions alone and the plastic flow may be preceded by microstructural damage.

Using this time for deceleration,  $T$ , the average strain rate in the plastically distorted portion can be estimated. The change in length,  $(L - L_1)$ , occurs over material of initial length  $(L - X)$ , hence the strain and thus average strain rate can be calculated,

$$\dot{\varepsilon} = \frac{L - L_1}{L - X} \left( \frac{V}{2(L - L_1)} \right) = \frac{1}{2} \left( \frac{V}{L - X} \right). \quad (1.23)$$

Within the limits of the technique available to him, Taylor did provide a turning point in the field of high strain-rate engineering. Taylor's original equation requires several simplifying assumptions: the elastic stress wave is assumed to be one-dimensional, the elastic tensile wave is reflected entirely from the plastic front, the projectile is assumed to be rigid-plastic (i.e. exhibits no elastic behaviour). The projectile/target interface is assumed to be frictionless and the target is 'rigid'. The latter two assumptions are better approximated by a 'symmetrical' Taylor impact.

Whiffin (1948) and Taylor (1948b) solved these equations by numerically determining the plastic wave speed consistent with both theory and observed deformation, the yield stress can then be determined. A series of correction factors dependent on impact velocity was found by Whiffin for mild steel cylinders.

Using this formula, Whiffin determined the dynamic yield stress at the elasto-plastic boundary of various metals for a range of impact velocities, 100 m s<sup>-1</sup> to 900 m s<sup>-1</sup>. The values were found to be independent of impact velocity so it seemed a fair estimate of the dynamic yield stress. Typically this was found to be 3 times the static value for steel. Impacts of velocity greater than  $c_{pl}$  were not used; in this regime the plastic wave would be unable to escape from the interface. A shock wave will stand at some small distance from the interface, high pressures behind this cause effects such as material erosion which are not taken into account by Taylor's analysis.

Ignoring radial inertia and considering the material to be rigid-plastic so that there is a constant stress field in the yielding portion of the projectile, Taylor predicted final profiles of deformed rods. Material which passes through the elasto-plastic interface must spread out rapidly in order to conserve volume. When comparing these predictions with Whiffin's experiments, there was found to be a good match at the lower velocities but at higher velocities there were large discrepancies. Taylor's approach was modified, to take account of elastic strain and work-hardening, at his own suggestion. Analysis for impact velocities above  $c_{pl}$  was also produced.

Subsequently this work was extended to take account of projectile mass loss by erosion (Recht 1978) and the problem was also reanalysed using an energy balance approach in (Hawkyard 1969).

When using Taylor's calculation, there are many assumptions made, as discussed earlier, but also defining the elastoplastic boundary is difficult as the outer dimensions do not always indicate its position. Early computer simulations (Wilkins and Guinan 1973) showed that the position of the plastic front, which is largely responsible for decelerating the incoming elastic part, is closer to the rigid boundary than the outward appearance shows. Parameters in the model were altered iteratively in order to match the experimentally achieved rod profiles, hence a different, more accurate yield stress could be determined. Microstructural examination found that plastic flow may also be preceded by twinning, cracks and compression bands (Carrington and Gayler 1948).

### 1.3 Penetration and perforation/ballistic studies

Rod impact and also terminal ballistics, have been popular subjects of research for many years. More recently there has been a great effort to model these conceptually simple experiments using hydrocodes. There is therefore a vast literature, both historical and modern. This section aims to give an overview of the subject and refers to some major texts which would be an excellent starting point for a more detailed literature survey.

Inspired by the work of both John Hopkinson (1872a; 1872b) and his son Bernard Hopkinson (1905; 1914), G. I. Taylor went on to pioneer much in the field of dynamic material testing. Taylor is of course remembered today for the classic Taylor impact configuration (Taylor 1948b), he also carried out important research on areas such as plate perforation.

More recently two excellent books on the terminal ballistics field are (Zukas 1982; Zukas 1990). Contributors to these books include the most notable scientists in the field, these include V. Hohler, R. Recht, A.J. Stilp, R. Woodward and J. Zukas. There have also been two excellent reviews of the area of penetration mechanics, (Backman and Goldsmith 1978) and (Corbett et al. 1996). Maudlin, Rosenberg and Anderson have made important contributions to hydrocode modelling. A useful overview of hydrocodes is (Anderson Jr. 1987) and its application in ballistic impact is considered in (Anderson Jr. and Bodner 1988; Camacho and Ortiz 1997).

Many models use Hertz contact theory (Hertz 1882) as a basis for calculating impact pressures. Such models are however for spherical or cylindrical impactors and targets. The research presented in this dissertation is entirely flat-ended impactors impact flat targets. Hertz's theory is therefore not invoked in this research.

## Theory

Consider a long rod impacting end-on against a target, there are three possible outcomes

- (i) no penetration
- (ii) some penetration but not perforation
- (iii) perforation of target.

The possible penetration processes are illustrated in figure 1.3.1.

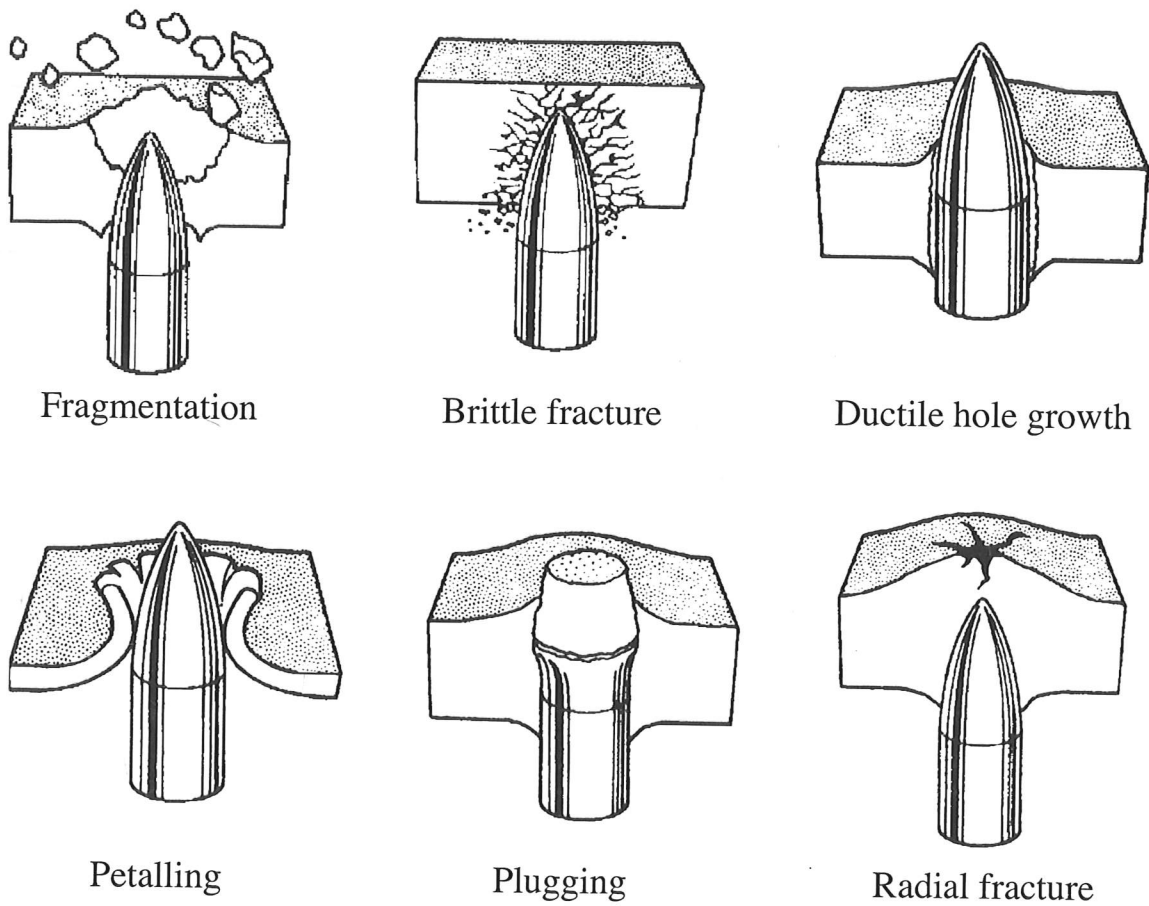


*Figure 1.3.1 Penetration processes (Zukas1990).*

The determining factors are impact velocity and angle, material strengths,  $L/D$  (length to diameter) ratio of the rod and plate thickness. Each of these three cases is considered individually below.

### **Impacts without penetration**

Essentially here we are considering a classic Taylor type impact, the theory of which was discussed in section 1.2.

### **Penetration without perforation**

Upon impact, first yield occurs beneath the indenter when the pressure exceeds the yield material of the impacted material. At this point, the plastic zone is small and displaced material is therefore accommodated by elastic deformation of the remainder of the target. For a more severe impact, the plastic zone can break out of a free surface, in this case the displaced material is able to escape by plastic flow to the sides of the indenter. This occurs at pressures circa three times the yield stress of the target (Tabor 2000). The pressure beneath the indenter is a function of the ratio of the strain imposed on the target material to its elastic strain capacity. This can also be expressed as  $\sigma_{yield}/E$ .

When designing armour, it important to be able to predict penetration depth for any particular impact. Important factors include kinetic energy and momentum per cross-sectional area of the projectile. Therefore the alignment of the projectile velocity vector with respect to the target material is also an important factor. Semi-empirical approaches to penetration depths can be found in (Backman and Goldsmith 1978; Backofen Jr. 1980; Zukas 1990).

Aspect ratio ( $L/D$ ) effects have been extensively studied. There is a positive relationship between this ratio and the penetration ability; there is however a limit to this. The optimum value of penetration per unit length of projectile is discussed in (Hohler and Stilp 1987; Herbette 1989; Rosenberg and Dekel 1994; Anderson Jr. et al. 1996; Rosenberg et al. 1997).

Due to the complicated nature of penetration mechanics and before computer simulations, empirical relations were the best predictions available. This was of course mainly applicable to situations in which the number of variables being

correlated was small and also when the prediction was within the range considered in the available data set. Examples of penetration formulae can be found in (Backofen Jr. 1980). However variables such as crater shape do not feature explicitly in these formulae. Certain assumptions such as neglecting friction between the penetrator and crater wall, penetration deformation etc. reduce the accuracy of these expressions. Obtaining such relations required much data and was hence costly.

Projectile erosion models are given in (Alekseevskii 1966; Tate 1967; Tate 1969), adapted from previous hydrodynamic theory. Long rod penetration was found to be somewhat analogous to shaped-charge jet penetration; tube-shaped craters in semi-infinite targets were observed in both types of experiment. Hence the basis of a fluid jet penetration model, depicted in figure 1.3.2, can be used in the theory of penetration.

Considering the nearly steady state situation in figure 1.3.2, the rear of the projectile has constant velocity of  $V$  towards the stagnation point at the impact face, the length of this rear part of the rod is hence decreasing. The stagnation point moves with constant velocity,  $U$ , through the target, from this point material in the rod flows laterally to form a hollow tube inside the crater. A form of equation, similar to the familiar Bernoulli equations, can be used though, it must first be modified by use of additional terms to account for the dynamic strength of the two materials concerned. Pressure  $p$  can therefore be estimated to be

$$p = \frac{1}{2} \rho_p (V - U)^2 + Y_p = \frac{1}{2} \rho_t U^2 + R_t. \quad (1.24)$$

Where  $R_t$  is the target 'resistance',  $Y_p$  the projectile yield strength,  $\rho_p$  and  $\rho_t$  are the densities of the projectile and target materials respectively. The yield strengths are typically taken to be 3 times and 2.5 times the experimentally measured yield strength for the projectile and target materials respectively (Rosenberg and Dekel 1994).

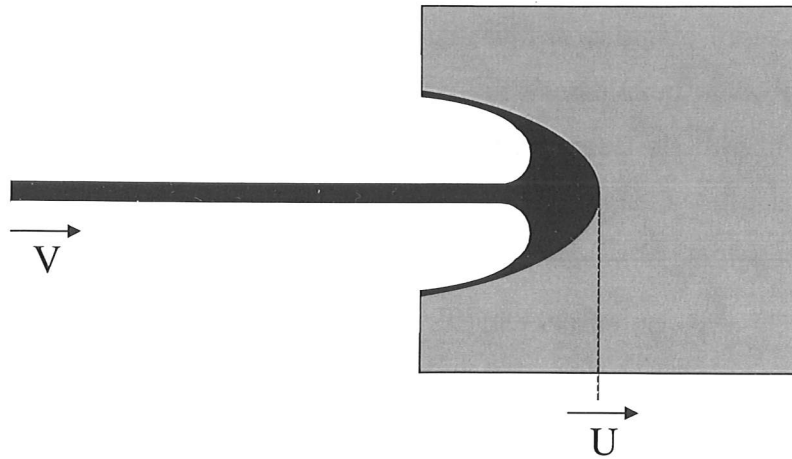


*Figure 1.3.2 Schematic of nearly steady-state situation upon penetration.*

Empirical evidence suggests that if the two materials are the same,  $R_t \approx 3 Y_p$ . The critical impact velocity,  $V_{crit1}$ , below which no penetration, occurs at  $U=0$  and  $R_t > Y_p$ , and is equal to

$$V_{crit1} = \sqrt{\frac{2(R_t - Y_p)}{\rho_p}}. \quad (1.25)$$

The onset of erosion is at impact velocity,

$$V_{crit2} = \sqrt{\frac{2(Y_p - R_t)}{\rho_t}}, \quad (1.26)$$

here  $R_t < Y_p$ .

Penetration can be assumed to have finished when either the rod has been completely eroded or decelerated. The penetration depth,  $P$ , is therefore  $U$  multiplied by the time period, at high velocities where the flow stress is significantly larger than the strength of the material, the normalised penetration is given by

$$\frac{P}{L} = \sqrt{\frac{\rho_p}{\rho_t}}. \quad (1.27)$$

A non-dimensional parameter,  $\rho V^2/Y$ , was suggested to compare impacts (Johnson 1972) to indicate the regime of material behaviour encountered in an impact. This parameter applies only for impacts between identical materials. Modifications for impacts between different materials gives  $\rho V^2/(R_f - Y_p)$ , this is only accurate for materials whose yield strengths are well known. This cannot be applied to materials, such as copper, that undergo work hardening during impact.

This model however, is not so accurate when the length to diameter ratio is not around 10:1. The depths of penetration predicted have discrepancies of up to 50 %. This discrepancy is discussed in terms of material parameters in (Rosenberg and Dekel 1994).

### **Perforation**

When penetrating a plate of finite thickness, the deformation can spread to include the rear surface or even perforation. At this stage, there are boundary effects and wave reflections to consider. If perforation just occurs, then the impact velocity causing this is called the 'ballistic limit'.

There are a number of important failure mechanisms. These are ductile hole enlargement, plugging, bulging and effects such as spallation (similar to that discussed earlier with respect to plate impact), petalling and other forms of fracture, figure 1.3.1.

In 1948, Taylor considered the process of making a circular hole in a flat sheet with a conical headed bullet (Taylor 1948b). This ductile hole enlargement process can leave crater walls on the exit face, an unsymmetrical deformation, or on both exit and entrance faces, a symmetrical deformation. These crater walls are formed because the outward radial pressure causes the material to accumulate around the hole. Taylor considered the principal stresses involved in this plastic deformation and concluded that 2.66 times more work is required to produce the symmetrical mode than the

A non-dimensional parameter,  $\rho V^2/Y$ , was suggested to compare impacts (Johnson 1972) to indicate the regime of material behaviour encountered in an impact. This parameter applies only for impacts between identical materials. Modifications for impacts between different materials gives  $\rho V^2/(R_f - Y_p)$ , this is only accurate for materials whose yield strengths are well known. This cannot be applied to materials, such as copper, that undergo work hardening during impact.

This model however, is not so accurate when the length to diameter ratio is not around 10:1. The depths of penetration predicted have discrepancies of up to 50 %. This discrepancy is discussed in terms of material parameters in (Rosenberg and Dekel 1994).

### **Perforation**

When penetrating a plate of finite thickness, the deformation can spread to include the rear surface or even perforation. At this stage, there are boundary effects and wave reflections to consider. If perforation just occurs, then the impact velocity causing this is called the 'ballistic limit'.

There are a number of important failure mechanisms. These are ductile hole enlargement, plugging, bulging and effects such as spallation (similar to that discussed earlier with respect to plate impact), petalling and other forms of fracture, figure 1.3.1.

In 1948, Taylor considered the process of making a circular hole in a flat sheet with a conical headed bullet (Taylor 1948b). This ductile hole enlargement process can leave crater walls on the exit face, an unsymmetrical deformation, or on both exit and entrance faces, a symmetrical deformation. These crater walls are formed because the outward radial pressure causes the material to accumulate around the hole. Taylor considered the principal stresses involved in this plastic deformation and concluded that 2.66 times more work is required to produce the symmetrical mode than the

unsymmetrical. Most materials show the latter, but the former is certainly advantageous when trying to resist perforation in armour systems.

Another prevalent perforation mechanism in finite plates is that of plug formation. This was analysed in three separate stages by (Awerbuch and Bodner 1974a). Firstly, there is a compressive stage in which material in the plate that is in contact with the projectile is accelerated. There are therefore both inertial forces and compressive forces on the projectile head. Second, the target material begins to shear and a plug is formed. This shearing force is due to the relative motion of target material that is being accelerated by the projectile and that which is not. This stage ends when the whole plug is travelling at the same velocity as the projectile. Finally, during the third stage the plug and projectile are moving as a rigid body, there is a shearing force along the length of the plug. There is also some frictional heating between the projectile and target material; this is neglected as the effect is localised. There can be local melting as there is little time for the heat to be dissipated.

In (Awerbuch and Bodner 1974a), these three stages are used to create a plugging model that predicts residual projectile velocities, force-time histories and contact times. The three stages are illustrated in figure 1.3.3. These were shown to agree well with experimental results in a subsequent paper (Awerbuch and Bodner 1974b). There are however, some problems with their model, it does not take account of plate bulging, dishing and stretching which commonly occur during the plugging process. A number of papers modify the model to take account of this (Jones 1968; Wilkins 1978). However, none takes account of simultaneous deformation in target and projectile or more complicated flow patterns. Hydrocode modelling may well therefore be more useful than even some of the more complicated analytical models.

As expected, the penetration behaviour of a flat-faced right-ended cylinder is very different to that of a shaped nose or hemi-spherical end. Flat-faced projectiles tend to produce plugging failure (Goldsmith 1985). Other factors affecting impact behaviour include impact velocity, target thickness, obliquity, projectile yaw and target properties such as tendency to form shear bands. One method often employed in armour systems in order to improve ballistic performance is the use of multi-layered

systems. A hard facing material, for example a hard steel, would be used to break up the projectile and this can be backed with a more ductile layer that can absorb the kinetic energy of the fragments. The relative hardness of the projectile and target is very important. Alumina ceramics are harder than steel and can break up steel projectiles. However, tungsten carbide is harder than alumina and can only be "defeated" by harder ceramics such as silicon carbide or boron nitride; see (Field 1988). Ceramics are often used as a facing material as they are not only hard but they erode the projectile as it passes through. The advantages of ceramics include the fact that small tiles that have been damaged are easily replaced and transparent tiles can be incorporated into an armoured vehicle to be used as windows. It is thought that the harder the facing layer is, the better the ballistic resistance, however there is no simple relationship between the two.

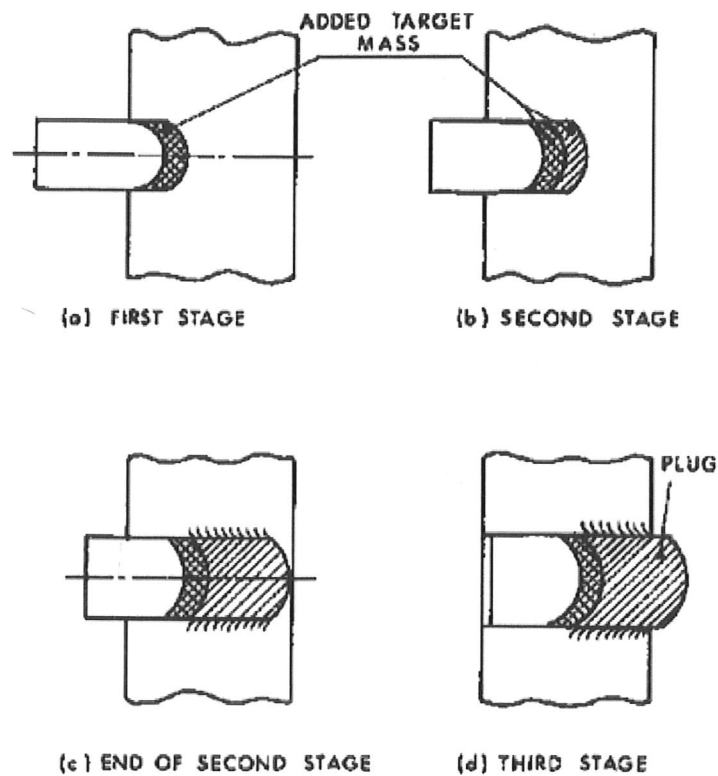


*Figure 1.3.3 The three stages of plugging as described in (Awerbuch and Bodner 1974a).*

Layered systems have proved to be even more valuable than simply being a way to combine the properties of more than one material; when the layers are in contact they resist penetration more than a monolithic beam of equivalent weight. These multi-

layered systems have been researched by many including (Marom and Bodner 1979) who looked at aluminium systems and (Corran et al. 1983) who worked with steel systems. The latter, observing that instead of the response of the plates being dominated by bending and shearing changed to one dominated by stretching or bulging.

Adding gaps between the layers however decreases ballistic performance. This introduces the whole concept of "spaced" armours. Here enough space has to be left between layers for the projectile to either break up or tumble. Hence they are much less effective as a penetrator. Precise detail on these spaced armours is classified and is therefore not discussed here.

Of course, both strain rate and lateral constraint are both extremely important in layered systems. Consider the example of steel: as the strain rate is increased from  $10^{-6}$  to  $10^3 \text{ s}^{-1}$ , the yield stress and ultimate tensile strength increase dramatically by 170 % and 40 % respectively (Manjoine 1944). Constraint can increase the yield strength by a factor of three in the case of quasi-static metal punches (Tabor 2000).

### **Experimental techniques**

Parameters which are commonly measured during ballistic experiments include:

- (i) Velocity and path of projectile both prior to impact, this can be calculated from a series of measured transit times.
- (ii) Velocity and path of projectile post impact. High-speed photography or flash radiography may be used for this, if these techniques are not available then yaw cards can be used. These are plastic or paper cards, which are thin enough not to affect the velocity of the projectile, are placed at intervals over the anticipated path of the trajectory. Perforation shape allows flight orientation to be deduced.

- (iii) Masses, velocity and path of fragments created by the impact event, high-speed photography or flash radiography can be used to visualise path and measure the velocity. The masses can be measured by soft recovery of debris. When collecting debris it is important to reduce their velocity post-impact without causing further damage to them ie. by soft recovery or even better by using momentum traps; see the classic work of (Hopkinson 1914) and (Sun 1991) for a more recent use. Post-mortem measurements can be carried out on the projectile, target and metallurgical examination can also be used. Hence both macroscopic and microscopic change can be taken into account when developing models.
- (iv) Velocity of target post-impact can be determined by use of high-speed photography or flash radiography.
- (v) Hole size and mass loss to target can be determined by soft recovery of the debris. Note that hole size during and post-impact can be different as residual stresses relax.
- (vi) Shape and dimensions of recovered projectile which are measured by recovery of debris.
- (vii) Stress and strain during the impact event can be measured by using reverse ballistic experiments in order to avoid the difficulties of firing an instrumented rod. In a reverse ballistic experiment, the plate is fired at a stationary rod. The plate is limited in dimension to that of the barrel of the gun and the mass of the flyer is limited by the performance of the gun.
- (viii) The ballistic limit is often quoted, this is usually the impact velocity at which a 50 % probability of perforation of the target.
- (ix) Microscopic change during impact can be monitored by use of optical microscopy, SEM, TEM, hardness, X-ray diffraction pre and post-impact. However, this is very time consuming

## 1.4 Conclusion

Studying both the shock and ballistic properties of a material leads to an understanding of behaviour across a wide range of strain rates. Shock experiments provide a simple geometry in which to study material response to high stress and high strain rates. These provide well-defined input parameters for models. These models can then be extended to more complex situations, such as those encountered in ballistics experiments. These provide an opportunity to study three dimensional problems, in order to model these accurately however, the parameters have to be determined accurately. The Taylor tests provide lower strain rate regimes in which to gain data. By studying a variety of strain rates, modellers can predict material behaviour in all types of situations.

## References

- Alekseevskii, V. P. (1966). "Penetration of a rod into a target at high velocity." Combust. Explos. Shock Waves **2(2)**: 63-66.
- Anderson Jr., C. E. (1987). Int. J. Impact Engng. **5**: 33-59.
- Anderson Jr., C. E. and S. R. Bodner (1988). "Ballistic impact: The status of analytical and numerical modeling." Int. J. Impact. Engng **7**: 9-35.
- Anderson Jr., C. E., J. D. Walker, S. J. Bless and Y. Partom (1996). "On the L/D effect for long rod penetrators." Int. J. Impact Engng **18**: 247-264.
- Awerbuch, J. and S. R. Bodner (1974a). "Analysis of the mechanics of perforation of projectiles in metallic plates." Int. J. Solids Structures **10**: 671-684.
- Awerbuch, J. and S. R. Bodner (1974b). "Experimental investigation of normal perforation of projectiles in metallic plates." Int. J. Solids Structures **10**: 685-699.
- Backman, M. E. and W. Goldsmith (1978). "The mechanics of penetration of projectiles into targets." Int. J. Engng Sci. **16**: 1-99.
- Backofen Jr., J. E. (1980). 5th Int. Symp. Ballistics, France, ENSAE.
- Bancroft, D. (1941). "The velocity of longitudinal waves in cylindrical bars." Physical Review **59**: 588-593.
- Barker, L. M. and R. E. Hollenbach (1974). "Shock wave study of the alpha-epsilon phase transition in iron." J. Appl. Phys. **45(11)**: 4872-4887.
- Brace, W. F. and A. H. Jones (1971). "Comparison of uniaxial deformation in shock and static loading of three rocks." J. Geophys. Res. **76**: 4913-4921.
- Camacho, G. T. and M. Ortiz (1997). Comput. Meth. Appl. Mech. Engng **142**: 269-301.
- Carrington, W. E. and M. L. V. Gayler (1948). "The use of flat-ended projectiles for determining dynamic yield stress." Proc. R. Soc. Lond. A **194**: 323-331.
- Chen, D., S. T. S. Al-Hassini, M. Sarumi and X. Jin (1997). "Crack straining-based spall model." Int. J. Imp. Engng. **19**: 107-116.
- Church, P. D., W. G. Proud, T. D. Andrews and B. Goldthorpe (2001). The spall strength measurement and modelling of AQ80 iron and copper systems. 12th APS Topical Group on Shock Compression of Condensed Matter, Atlanta, AIP.

- Corbett, G. G., S. R. Reid and W. Johnson (1996). "Impact loading of plates and shells by free-flying projectiles: a review." Int. J. Impact Engng **18**(2): 141-230.
- Corran, R. S. J., P. J. Shadbolt and C. Ruiz (1983). "Impact loading of plates-an experimental investigation." Int. J. Imp. Engng. **1**: 3-22.
- Curran, D. R., L. Seaman and D. A. Shockey (1987). "Dynamic failure of solids." Phy. Rep. **147**: 253-388.
- Davison, L. and R. A. Graham (1979). "Shock compression of solids." Phy. Rep. **55**(4): 255-379.
- Erlich, D. C. and D. A. Shockey (1983). Dynamic flow curve of 4340 steel as determined by the symmetric rod impact test. Shock Waves in Condensed Matter-1983, Santa Fe, New Mexico, Elsevier Science Publishers.
- Field, J. E. (1988). Final Technical Report: Investigation of the impact performance of various glass and ceramic systems, United States Army European Research Office of the U.S. Army, London, England. Contract number DAJA45-85-C-0021.
- Goldsmith, W. (1985). Initiation of perforation in thin plates by projectiles. Metal Forming and Impact Mechanics. S. R. Reid, Pergamon: 271-287.
- Grady, D. E. (1988). "The spall strength of condensed matter." J. Mech. Phys. Solids **36**(3): 353-384.
- Hammond, R. I., P. D. Church, A. Grief, W. G. Proud and J. E. Field (2003b). Dependence of measured lateral stress in thickness of protective "padding" around gauge. APS, Portland, Oregon.
- Hammond, R. I., W. G. Proud and J. E. Field (2003a). "Classic and symmetric Taylor impact on tungsten alloys." J. Phys. IV France **110**: 483-488.
- Hammond, R. I. and W. G. Proud (2004). "Does the pressure induced phase transition occur for all low-alloy steels?" Proc. Roy. Soc. A In print.
- Hawkyard, J. B. (1969). "A theory for the mushrooming of flat-ended projectiles impinging on a flat rigid anvil, using energy considerations." Int. J. Mech. Sci. **11**: 313-333.
- Herbette, G. (1989). The influence of projectile shape on penetration power. Proc. 11th Int. Symp. Ballistics: 561-567.
- Hertz, H. (1882). J. Reine Angew. Math. **92**:192.

- Hohler, V. and A. J. Stilp (1987). "Hypervelocity impact of rod projectiles with L/D from 1 to 32." Int. J. Impact Engng **5**: 323-331.
- Hopkinson, B. (1905). "The effects of momentary stresses in metals." Proc. R. Soc. Lond. **74**: 498-506.
- Hopkinson, B. (1914). "A method of measuring the pressure produced in the detonation of high explosives or by the impact of bullets." Phil. Trans. R. Soc. Lond. A **213**: 437-456.
- Hopkinson, J. (1872a). "Further experiments on the rupture of iron wire." Proc. Manchest. Liter. Philos. Soc. **11**: 119-121.
- Hopkinson, J. (1872b). "On the rupture of iron wire by a blow." Proc. Manchest. Liter. Philos. Soc. **11**: 40-45.
- Johnson, J. N. (1981). "Dynamic fracture and spallation in ductile solids." J. Appl. Phys. **52**(4): 2812-2825.
- Johnson, J. N., R. S. Hixson, D. L. Tonks and A. K. Zurek (1995). Rate-dependent spallation properties of tantalum. APS Topical Group on Shock Compression of Condensed Matter, Seattle, Washington, AIP.
- Johnson, W. (1972). Impact strength of materials, Hodder Arnold.
- Jones, N. (1968). "Impulsive loading of simply supported circular rigid plastic plate." J. Appl. Mech. **35**: 59-65.
- Manjoine, M. J. (1944). "Influence of rate of strain and temperature on yield stresses of mild steel." J. Appl. Mech. **11A**: 211-218.
- Marom, I. and S. R. Bodner (1979). "Projectile perforation of multi-layered beams." Int. J. Mech. Sci. **21**: 489-504.
- Marsh, S. P. (1980). LASL Shock Hugoniot Data. Berkeley, California, University of California Press.
- Murray, N. H. (1996). The response of alumina based ceramics to high strain-rate loading. Cavendish Laboratory, Thesis University of Cambridge: 97.
- Radford, D. D., P. D. Church, P. J. Gould and E. Eadington (2002). Deformation and failure during "symmetric" Taylor impact tests. Plasticity '02, NEAT Press, Maryland.
- Recht, R. F. (1978). "Taylor ballistic impact modelling applied to deformation and mass loss determinations." Int. J. Engng. Sci. **16**: 809-827.

- Rosenberg, Z. and E. Dekel (1994). "The relation between the penetration capability of long rods and their length to diameter ratio." Int. J. Impact Engng **15**: 125-130.
- Rosenberg, Z., R. Kreif and E. Dekel (1997). "A note on the geometric scaling of long-rod penetration." Int. J. Impact Engng **19**: 277-283.
- Roy, G., H. Trumel and A. Dragon (2002). Spall damage modelling. Inertia effects in fully elastic-plastic range. Plasticity '02, NEAT Press, Maryland.
- Sun, Q. (1991). Solid particle erosion and ballistic impact. Thesis, Cavendish Laboratory, Cambridge University.
- Tabor, D. (2000). The hardness of metals, Oxford University Press.
- Tate, A. (1967). "A theory for the deceleration of long rods after impact." J. Mech. Phys. Solids **15**: 387-399.
- Tate, A. (1969). "Further results in the theory of long rod penetration." J. Mech. Phys. Solids **17**: 141-150.
- Taylor, G. I. (1948b). "The formation and enlargement of a circular hole in a thin plastic sheet." Quart. J. Mech. Appl. Math. **1**: 103-124.
- Taylor, G. I. (1948a). "The use of flat-ended projectiles for determining dynamic yield stress, Part 1. Theoretical Considerations." Proc. R. Soc. Lond. A **xciv**: 289-299.
- Tonks, D. L., J. E. Vorthman, R. Hixson, A. Kelly and A. K. Zurek (1999). Spallation studies on shock loaded U-6 wt.% Nb. 11th APS Topical Group on Shock Compression of Condensed Matter, Snowbird, Utah, AIP.
- Walley, S. M., P. D. Church, R. Townsley and J. E. Field (2000). "Validation of a path-dependent constitutive model for fcc and bcc metals using "symmetric" Taylor impact." J. Phys. IV France **10**: Pr9-69-74.
- Whiffin, A. C. (1948). "The use of flat-ended projectiles for determining dynamic yield stress: II. Tests on various metallic materials." Proc. R. Soc. Lond. A **xciv**: 300-322.
- Wilkins, M. L. (1978). "Mechanics of penetration and perforation." Int. J. Engng Sci. **16**(793-807).
- Wilkins, M. L. and M. W. Guinan (1973). "Impact of cylinders on a rigid boundary." J. Appl. Phys. **44**: 1200-1206.

Zukas, J. A. (1982). Stress waves in solids. Impact Dynamics. J. A. Zukas, T. Nicholas, H. F. Swift, L. B. Greszczuk and D. R. Curran. New York, Wiley-Interscience: 1-27.

Zukas, J. A. (1990). High velocity impact dynamics, John Wiley & Sons Inc., New York.

## Chapter 2

### Materials

#### 2.1 Bainitic steels

##### Discovery of bainite

Edgar C. Bain, pictured in figure 2.1.1, was a pioneer in the study of transformations in steels. During his career, which spanned 35-40 years, he carried out a great deal of important work in the field. It was in the 1920s and 1930s that he carried out a large proportion of his most significant work including research on solid solutions and transformation mechanisms between face-centred-cubic (fcc) austenite and body-centred-cubic (bcc) or body-centred-tetragonal (bct) martensite (Bain 1972; Bain 1975). Up to this time, research had been performed under continuous cooling conditions. This inevitably lead to complicated microstructures which probably included some bainite.



*Figure 2.1.1 Edgar C. Bain (Bain 1975).*

During the late 1920s, Bain teamed up with E. C. Davenport, at the Kearny Research Laboratory of the U.S. Steel Corporation, to form one of the first teams to use isothermal heat treatments. In 1930, just above the martensite start temperature,  $M_s$ , see figure 2.1.2, a “dark etching aggregate” was observed and named martensite-troosite. They also identified ‘high range’ martensite-troosite which formed at a higher temperature. These forms of steel were found to be as hard as martensite but significantly tougher; hence the scientific interest.

In 1934, research staff at the Kearny Lab named the newly discovered microstructure ‘Bainite’ but initially the name was rarely used due to Bain’s modesty. It wasn’t until the late 1930s that the labels upper and lower bainite started to be used in scientific writing.

### **What are bainitic steels?**

Bainite is a non-lamellar mixture of cementite and fine plates of ferrite. In some cases, it can give the alloy useful properties. The free energy change driving the fcc austenite to transform into bcc ferrite increases at large undercoolings. Once the temperature is lower than the bainite start temperature,  $B_s$ , upper bainite can form. Ferrite plates grow into the austenite, the carbon is forced out, hence carbides nucleate between the ferrite plates. Figure 2.1.3 gives a schematic diagram for the formation of both upper and lower bainitic microstructures.

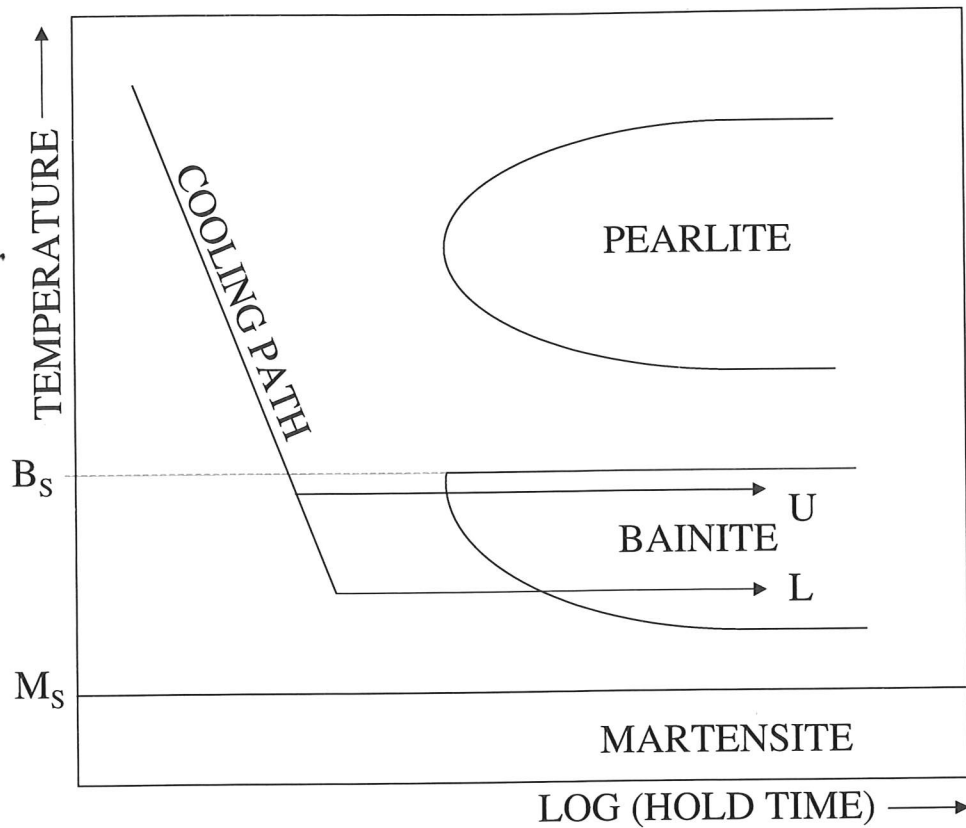


**Figure 2.1.2** Schematic form of a Time-Temperature-Transformation (TTT) diagram for steel (Bhadeshia 2001).

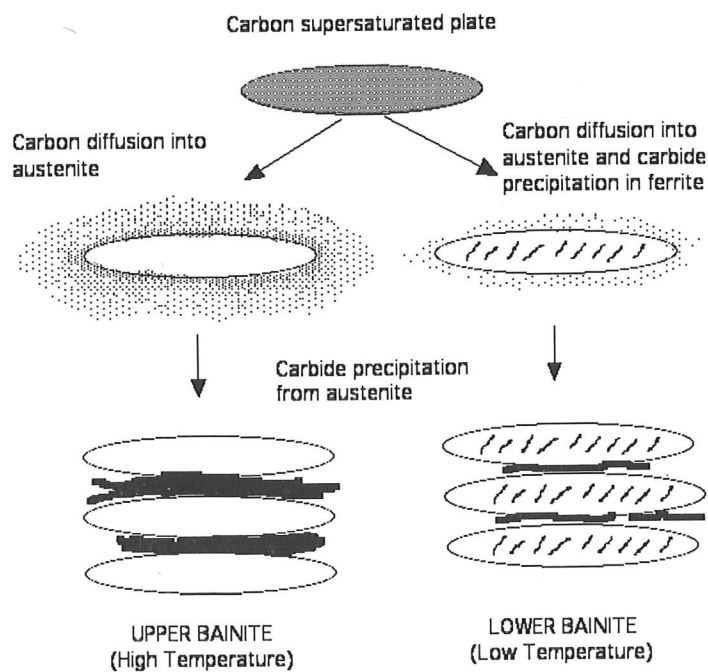


**Figure 2.1.3** Schematic of formation of both upper and lower bainitic microstructures (Bhadeshia 2001).

The temperature below which bainitic transformations,  $B_s$ , take place, can easily be estimated if the composition of the steel is known (Olson et al. 1989).

$$B_s(^{\circ}\text{C}) = 830 - 270w_C - 90w_{Mn} - 37w_{Ni} - 70w_{Cr} - 83w_{Mo}, \quad (2.1)$$

where  $w_x$  is the weight per cent of element  $x$ .

At temperatures just above the martensite start temperature,  $M_s$ , well-defined ferrite plates, which are crystallographically oriented to the austenite matrix, form. Both the matrix and the plates contain a dispersion of fine carbides. Bainite forms by a crystallographic shear mechanism (Cottrell 1995). Lower bainite can be formed using the lower cooling path, labelled L, in figure 2.1.2.

In order to form upper bainite, a cooling path such as the upper one, labelled U, shown in figure 2.1.2 is necessary. To form either bainite, a rapid quench followed by an isothermal hold are required. Slow cooling would lead to the pearlite region and the resulting microstructure would be interpenetrating single crystals of ferrite and cementite with iron carbide, appearing as an alternating lamellar structure on cross-sections. Fast cooling would result in a martensitic structure which is characteristically made up of laths or plates.

Both upper and lower bainite consist of sheaves of plates of ferrite usually separated by untransformed austenite, although the plates could also be separated by martensite or cementite. Within a sheaf, the ferrite plates are interconnected in three dimensions and hence have a common crystallographic orientation. On formation of these ferrite plates, there needs to be elastic accommodation of the surrounding austenite, hence the yield strength has a large effect on the shape deformation in the plates. Plate size is also related to the thermodynamic driving force for the phase change. At high temperatures, recovery of the austenite may lead to coarsening of the plates.

The principal difference between the upper and lower bainite is the distribution of carbide precipitates. In upper bainite, the ferrite is free from precipitates, the carbides precipitate from the austenite, which is enriched in carbon. In the lower bainite, finer

plate-like carbides exist in the ferrite plates. The dislocation density of bainitic ferrite increases as the transformation temperature is reduced (Bhadeshia 2001), hence the lower bainite ferrite will have the higher dislocation density and hence may be stronger.

### **Pressure induced phase transformations**

At high pressures, a third phase,  $\epsilon$ -iron which is hexagonal close-packed can be obtained (Barker and Hollenbach 1974). This transition causes a change in specific volume of the material and hence the phase transition can be monitored by measuring the pressure. In this research, this phase is only expected to exist during impact and is unlikely to be observable post-impact, though some change in the recovered microstructure may be found.

Such a phase transition is martensitic: it must occur without diffusion given the rapid propagation of the transformation front through the material under shock conditions. Because of the glissile nature of the front it can travel at up to the speed of sound in the metal (Honeycombe and Bhadeshia 1995). The interface structure can be described in terms of dislocations, for a martensitic transformation it must not be necessary for any of these dislocations to climb as the interface moves. To ensure a glissile (mobile) interface, the Burgers vector of the dislocations on the interface must not lie in the plane of the interface itself (with the exception of screw dislocations). When there is more than one set of dislocations, with different Burgers vectors, in the interface, the interface can be rendered sessile. Hence across the interface there must be perfect fit along one line. A martensitic transformation can therefore only occur if one line can be preserved without either distortion or rotation. This is known as invariant-line strain. The phase transformation being considered in this research involves a dilation of circa 4%. This must be accommodated within the material without violating the invariant-line strain condition.

### **Bainite studied in this research**

The two materials considered in this research are chosen to be examples of an upper bainite and a so-called lower-temperature bainite. The latter having undergone a heat-treatment similar to that labeled L in the figure 2.1. However a lower bainitic structure did not result; the carbide formation having been inhibited by the silicon content of the material. These were of interest as potential armour materials and were provided by QinetiQ, Fort Halstead. Using physical models solely (phase transformation theory), novel high strength bainitic steels were designed (Caballero et al. 2001a; Caballero et al. 2001b; Caballero et al. 2002) avoiding the need for extensive, expensive experimental work. A table of the physical properties can be found in chapter 4.

The lower temperature bainite had a composition of 0.8 wt. % carbon, 1.6 wt. % silicon, 2 wt. % manganese, 1.4 wt. % chromium, 0.25 wt. % molybdenum, the balance being iron. This was normalised at 900 °C for 1 hour and then held at 190 °C for 2 weeks.

The upper bainite had a composition of 0.4 wt. % carbon, 1.5 wt. % silicon, 1 wt. % manganese, 2 wt. % chromium, 0.5 wt. % molybdenum, the balance being iron. This was normalised at 900 °C for 1 hour and then held at 300 °C for 256 minutes.

## 2.2 Tungsten alloys

The word tungsten is derived from the Swedish words *tung* and *sten*, which translate as heavy and stone respectively. Medieval german tin smelters found tin ores that contained tungsten had a greatly reduced yield. It was said the tungsten devoured the tin "like a wolf", tungsten therefore could have acquired its alternative name, wolfram, and hence its chemical symbol, W, may be as a result of this. However it is more probable that it was named after Peter Woulfe who examined the mineral now known as wolframite in 1779 and concluded it must contain a new substance.

Tungsten has become an essential material for a wide variety of applications due to its high melting point, 1650 °C, which is the highest melting point of all metals, its high density and low vapour pressure. At low temperatures, it has excellent corrosion resistance but at elevated temperatures it must be protected in order to prevent oxidation.

Tungsten and its alloys are used extensively for filaments and electric lamps, X-ray targets, windings and heating elements for furnaces, many high-speed tool steels contain tungsten, radiation shields, mining equipment eg. boring bars, weights and counter-balances and environmentally friendly ammunition.

Generally, tungsten based materials are made by two routes. The first using tungsten as a filler in high-density polymer/metal compounds which look and feel like and can often be used to replace metallic components. Such parts may be injection-molded and can therefore be intricate and also economical.

The second route is to use tungsten as a raw material for powder metallurgy. Tungsten is often alloyed with nickel, copper and iron by powder processing. Powder is compacted into the desired shape by die pressing, isostatic pressing, extrusion, injection moulding or slip casting. The resulting porous shape, known as the 'green' body, is then densified by application of heat and often pressure. These alloys can then be machined by conventional methods such as turning, milling, grinding, polishing, drilling and tapping.

Unfortunately components made by powder metallurgy, have a large scatter in their tensile strength, apparently identical parts may have different strengths as they can contain flaws of different sizes. These flaws may well be as a result of agglomerates in the original powder. The particles stick together in order to reduce their surface energy, this leads to a non-uniform initial density in the 'green' body. When densification occurs, the zones of lower initial density will shrink more than the surrounding material leaving voids and the zones of higher initial density, the agglomerates, will shrink less and cause cracking in surrounding material. The size and number of agglomerated can be reduced by pre-processing such as ball-milling.

Tungsten based alloys, made by powder metallurgy routes, are often used as penetrators due to their high density and strength. By addition of other elements, ductility can be improved at the expense of strength, alloys with around 91 % tungsten have been found to be a good compromise (Satapathy et al. 1999).

The two materials were investigated in this work were Densimet 176 FNC tungsten alloy and SAC tungsten alloy. Both of which were supplied by QinetiQ, Fort Halstead. The rod dimensions, length 55 mm and diameter 5.5 mm, and the composition, 92 wt. % bcc W particles, diameter circa 20  $\mu\text{m}$ , 5 wt. % Ni, 1.5 wt. % Fe and 1.5 wt. % Co matrix, were identical in both cases. Refer to table 2.2.1 for the physical properties of the two materials.

Property	SAC Tungsten Alloy	FNC Tungsten Alloy
Density, $\rho$ , ( $\pm 20$ kg m <sup>-3</sup> )	17560	17750
Young's modulus, E, ( $\pm 2$ GPa)	366	366
Shear modulus, $\mu$ , ( $\pm 0.4$ GPa)	142.6	142.2
Bulk modulus, K, ( $\pm 1$ GPa)	283	287
Poisson's ratio, $\nu$ , ( $\pm 0.006$ )	0.284	0.287
Longitudinal sound speed, $c_l$ , ( $\pm 5$ m s <sup>-1</sup> )	5190	5180
Transverse sound speed, $c_s$ , ( $\pm 5$ m s <sup>-1</sup> )	2850	2830
Bulk sound speed, $c_0$ , ( $\pm 10$ m s <sup>-1</sup> )	4010	4020
Sound speed in a rod, $c_R$ , ( $\pm 20$ m s <sup>-1</sup> )	4570	4540

*Table 2.2.1 Physical properties of SAC and FNC tungsten alloys. Data were measured in the Cavendish Laboratory as part of this investigation.*

### 2.3 Rolled Homogeneous Armour Steel (RHA)

Supplied by DERA (now QinetiQ) Fort Halstead. It is currently in use as an armour steel for vehicles, the lower temperature bainite discussed in section 2.1 is a possible replacement for it. Refer to table 2.3.1 for the physical properties. This alloy can have hardness of 240 HV10 to 380 HV10.

Property	
Density, $\rho$ , ( $\pm 5 \text{ kg m}^{-3}$ )	7824
Young's modulus, $E$ , ( $\pm 1 \text{ GPa}$ )	211
Shear modulus, $\mu$ , ( $\pm 0.2 \text{ GPa}$ )	82.1
Bulk modulus, $K$ , ( $\pm 0.6 \text{ GPa}$ )	163.4
Poisson's ratio, $\nu$ , ( $\pm 0.006$ )	0.285
Longitudinal sound speed, $c_l$ , ( $\pm 5 \text{ m s}^{-1}$ )	5905
Transverse sound speed, $c_s$ , ( $\pm 5 \text{ m s}^{-1}$ )	3239
Bulk sound speed, $c_0$ , ( $\pm 10 \text{ m s}^{-1}$ )	4570

*Table 2.3.1 Physical properties of RHA. Data taken from (Forde 2000).*

## References

- Bain, E. C. (1972). "Some recollections, early observations of phase transformations-micromorphology." Met. Trans. **3**: 1031-1034.
- Bain, E. C. (1975). Pioneering in steel reseach: A personal record, American Society for Metals.
- Barker, L. M. and R. E. Hollenbach (1974). "Shock wave studies of the alpha-epsilon phase transition in iron." J. Appl. Phys. **45**(11): 4872-4887.
- Bhadeshia, H. K. D. H. (2001). Bainite in steels, IOM Communications Ltd.
- Caballero, F. G., H. K. D. H. Bhadeshia, K. J. A. Mawella, D. G. Jones and P. Brown (2001a). "Design of novel high strength bainitic steels: Part 1." Mat. Sci. Tech. **17**: 512-516.
- Caballero, F. G., H. K. D. H. Bhadeshia, K. J. A. Mawella, D. G. Jones and P. Brown (2001b). "Design of novel high strength bainitic steels: Part 2." Mat. Sci. Tech. **17**: 517-522.
- Caballero, F. G., H. K. D. H. Bhadeshia, K. J. A. Mawella, D. G. Jones and P. Brown (2002). "Very strong low temperature bainite." Mat. Sci. & Tech. **18**: 279-284.
- Cottrell, A. (1995). An introduction to metallurgy, The Institute of Materials.
- Forde, L. C. (2000). Ballistic Impact of Rods. Cavendish Laboratory. Cambridge, Cambridge University: 339.
- Honeycombe, R. W. K. and H. K. D. H. Bhadeshia (1995). Steels: Microstructure and Properties. London, Edward Arnold.
- Olson, G. B., H. K. D. H. Bhadeshia and M. Cohen (1989). "Coupled diffusional displacive transformations." Acta Metall. **37**: 381-389.
- Satapathy, S., J. Cazamias, S. Bless, R. Monfredo Gee, L. Meyer and N. Brar (1999). Dynamic strength of tungsten-nickel-cobalt alloys. 11th APS Topical Group on Shock Compression of Condensed Matter, Snowbird, Utah, AIP.

## Chapter 3

### Experimental techniques

#### 3.1 Determination of static properties

The longitudinal sound speed,  $c_l$ , of a material can be used as a first estimate of the shock velocity (refer to section 1.1). It is therefore possible to construct a distance-time,  $x-t$  (figure 3.1.1), diagram before undertaking an experiment. This is especially important when considering the lateral releases which ultimately limit the timescale of the experiment. In this work sound speeds in the steel were measured ultra-sonically.

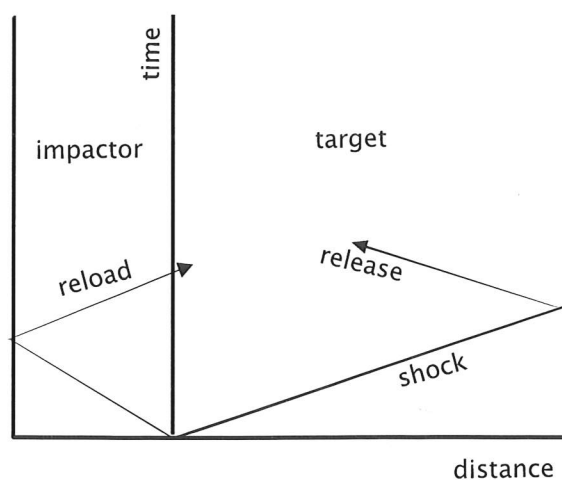


**Figure 3.1.1** An example  $x-t$  diagram. The gradient of a line is inversely proportional to the velocity.

#### Measurement of sound speed

Longitudinal sound speeds were measured using a Panametrics Videoscan 5 MHz transducer, which incorporates a z-cut piezo-electric quartz crystal as the active element. Silicone grease is the coupling agent for longitudinal sound speed measurements. The pulse generator/receiver (Panametrics 5052PR) is connected to the transducer which when placed on the sample sends a sound wave into the specimen. A current is induced in the transducer that is monitored using a Tektronix TDS 460 digital storage oscilloscope. A series of reflections is displayed, figure 3.1.2 and using their average spacing,  $\Delta t$ , and considering the thickness of the flat, parallel-sided sample the longitudinal sound speed can be calculated. Similarly the shear wave speed can be determined using 2.25 MHz Panametrics Videoscan transducers and a more viscous coupling agent such as boiled treacle.

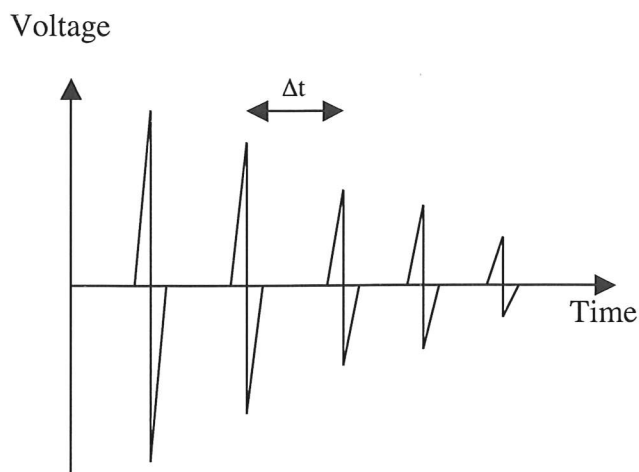


**Figure 3.1.2** Typical trace of reflections recorded during measurement of sound speed of a material.

The bulk wave speed can then be calculated.

$$c_0 = \sqrt{c_l^2 - \frac{4}{3}c_s^2}, \quad (3.1)$$

where  $c_l$  is the longitudinal sound speed and  $c_s$  is the shear wave speed.

Poisson's ratio,  $\nu$ , can also be found.

$$\nu = \frac{c_l^2 - 2c_s^2}{2(c_l^2 - c_s^2)}. \quad (3.2)$$

Note, from these measurements it is also possible to calculate the shear modulus,  $\mu$ ,

$$\mu = \rho c_s^2, \quad (3.3)$$

the bulk modulus,  $K$ ,

$$K = \rho c_l^2 - \frac{4}{3}\mu, \quad (3.4)$$

and the Young's modulus,  $E$ ,

$$E = \frac{9\mu K}{\mu + 3K}$$

(3.5)

### 3.2 The Cambridge impact facility

All the Hugoniot and lateral stress experiments were carried out using the single stage gas gun in the Cavendish Laboratory (figure 3.2.1).

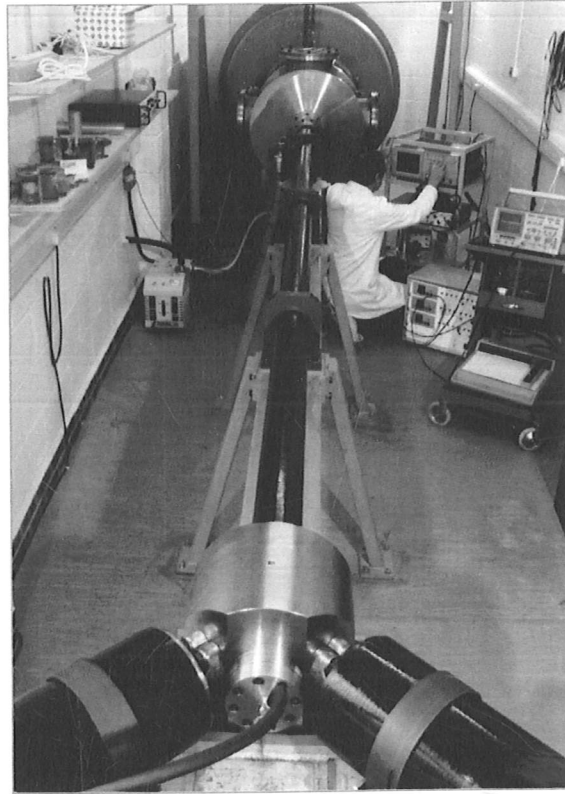


*Figure 3.2.1 Plate impact facility at Cavendish Laboratory.*

A flyer plate is attached to the sabot using three counter-sunk screws. The projectile is placed in the barrel and a breech-block secured in place. The projectile is held against the breech-block by a vacuum produced by pumping out the air behind the projectile. There are two “o” rings on the sabot, in this set-up the body and the “o” rings block the exits of the two reservoirs. This arrangement is known as a “wrap-around” breech. The reservoirs are filled with propellant gas using pressurised cylinders and compressors operating up to 350 bar. When using helium as a propelling gas, velocities of up to  $1.2 \text{ km s}^{-1}$  can be achieved. By altering the impact speed and the material of the flyer plate, the impact stress can be varied.

The gun is fired by the rotation of a solenoid which breaks the vacuum behind the projectile causing it to move forward, clearing the reservoir exits, it is then propelled down the barrel. The barrel is 5 m long and of 50 mm bore  $\pm 25 \mu\text{m}$ .

Projectile velocity is measured to an accuracy of  $\pm 0.5\%$  by means of four pairs of pins which are positioned at accurately known distances before the target. As the conductive flyer passes a pair of these pins, it completes a circuit giving a shorting signal which is recorded on an oscilloscope. Hence the velocity can be calculated. Graphite pins, diameter 0.3 mm, are used to measure velocities below  $600 \text{ m s}^{-1}$  and brass pins for higher velocities.

Stress levels are measured in the sample with Manganin gauges (refer to section 3.3).

### **Lateral Release**

So far only infinite planar waves which result in uni-axial strain have been considered in the theoretical discussion. However, the diameter of the projectile is determined by the bore of the barrel so infinite waves cannot be generated. Lateral release waves are generated at the edge of the projectile in which a tri-axial strain state exists. In this region the assumptions used in the derivation of the shock relations are no longer valid, hence the time "window" for 1-d data is limited. The timescale depends on the time taken for a wave to traverse from the edge to the centre. The soundspeed,  $c_L$ , can be used to estimate this, ie. 25 mm divided by the sound speed gives 5-10  $\mu\text{s}$  total time for most materials.

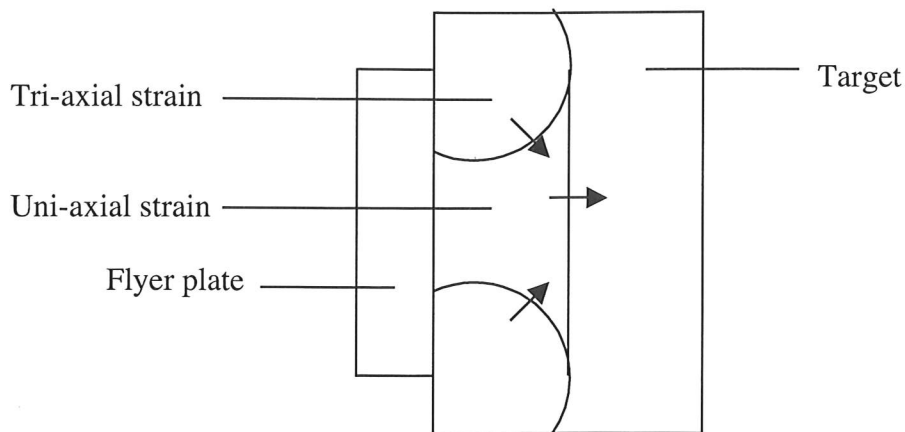


*Figure 3.2.2 Region in which uni-axial strain is reduced by lateral stress release waves to a tri-axial strain state.*

It is important to consider these lateral release waves when deciding where to place the gauges, only measurements made in the uni-axial system are relevant. Lateral release waves are also generated at the rear surface of the impactor, once these reach the gauge the stress is released.

### Sample Alignment and Flatness

Misalignment is inevitable with real materials and current engineering techniques, hence a perfectly flat, perpendicular impact is impossible to achieve.

Consider an impact with a misalignment of  $\theta$  and impact velocity  $V_i$ , the contact velocity  $V_c$  can be found by the equation

$$V_c = \frac{V_i}{\sin\theta} \approx \frac{V_i}{\theta}. \quad (3.6)$$

Shock waves are created when the contact velocity is greater than the shock velocity. In order that stress measurements are relevant the shock wave needs to be as close to perpendicular as possible. The angle of the shock wave away from perpendicular,  $\phi$ , can be found given the velocity of the contact angle must be the same in both materials.

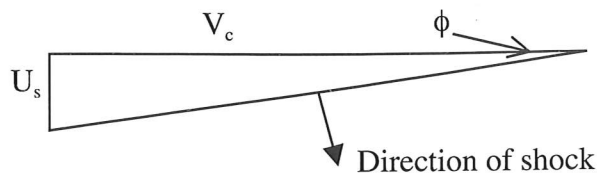


**Figure 3.2.3** Shock wavelets initiate at a contact point which moves at  $V_c$ , propagating at  $U_s$ , giving the angle off perpendicular as  $\phi$ .

By simple trigonometry, refer to figure 3.2.3, it found that

$$\tan \phi = \frac{U_s}{V_c}. \quad (3.7)$$

Taking the misalignment to be small, substituting in (3.6)

$$\phi \approx \frac{U_s \theta}{V_i}. \quad (3.8)$$

The shock angle is given by the ratio of impact to shock velocity multiplied by the misalignment angle. The tolerances achieved in this work were no worse than a milliradian. Considering an impact velocity of  $400 \text{ m s}^{-1}$  on copper, the shock velocity would be around  $4500 \text{ m s}^{-1}$ , hence the original misalignment would be multiplied by 11.

For a well-aligned shot, the sample, mounting, mounting ring, sample plate and flyer plate need to be flat *and* well aligned.

Once the projectile is assembled, it is held in a lathe and the flier plate is faced to be perpendicular to the rotation axis of the sabot.

## Experimental Set-Up

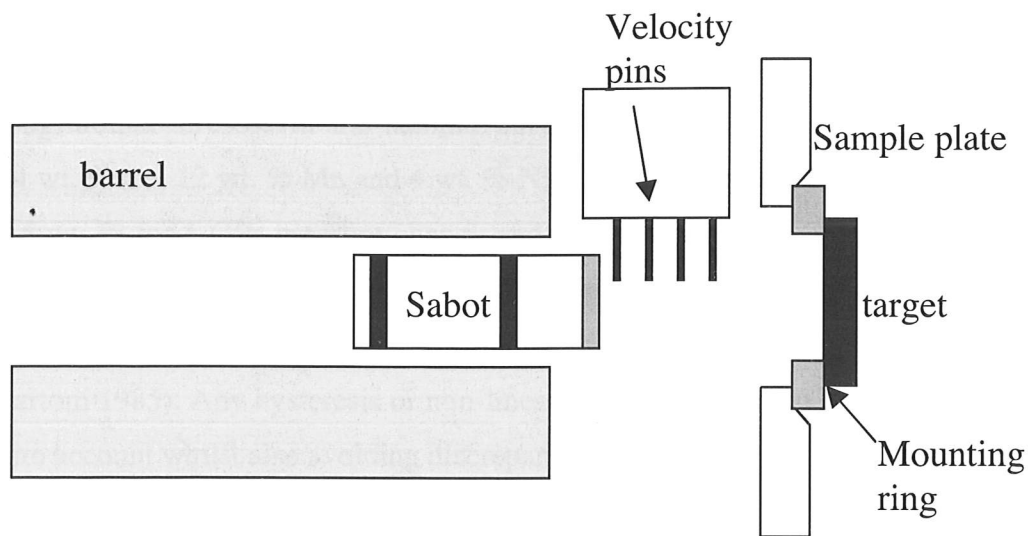


*Figure 3.2.4 Experimental set-up for plate impact experiment (not to scale).*

The sample plate is aligned to an accuracy of  $0.1 \mu\text{m}$  by use of a dial gauge and a plug which is inserted in the end of the barrel for each experiment.

The mounting ring is machined flat and parallel to better than  $10 \mu\text{m}$  over its 14 cm diameter. The central hole of the ring is diameter 6 cm which allows the projectile to pass through after the impact. The ring is lightly pressed into place on the sample plate, figure 3.2.4. The target is fixed to the ring using metal filled epoxy, which has good adhesion and minimal expansion on setting; care is taken not to get adhesive between the target and mounting ring.

At impact the sabot is partially in the barrel so ensuring that there is no yaw due to gravity acting on the projectile.

### 3.3 Stress measurements

Manganin piezo-resistive stress gauges were used to measure both lateral and longitudinal stresses in the sample during the impact. Manganin is an alloy of 84 wt. % Cu, 12 wt. % Mn and 4 wt. % Ni. Typically the resistance changes by about 2.5 wt. % for 1 GPa pressure change and the resistance is temperature independent. The gauges are commercially available, reproducibly manufactured and of well-defined response (Rosenberg et al. 1980; Rosenberg and Partom 1985; Rosenberg and Partom 1985). Any hysteresis or non-linearity of the manganin curves has been taken into account whilst also avoiding discrepancies due to configuration and composition.

The gauges used in this work were manufactured by Micro Measurement. Longitudinal stress was measured using fully epoxy encapsulated, LM-SS-21FD-050 gauges with a resistance of  $51.4 \Omega \pm 0.5 \%$  and an area of  $36 \text{ mm}^2$ . Lateral stress measurements were made with J2M-SS-580SF-025 gauges which have a resistance of  $25.0 \Omega \pm 2.0 \%$  (figure 3.3.1).

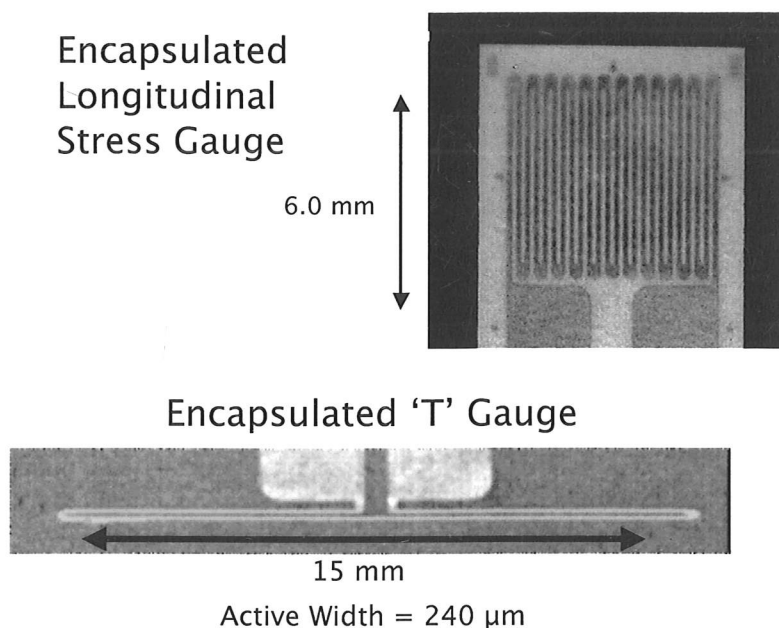


**Figure 3.3.1** The encapsulated longitudinal and lateral (*T*) stress gauges.

The gauge is incorporated in a Wheatstone bridge circuit as shown in figure 3.4.3. A power supply is used to discharge a 100 V, 2 A, 100  $\mu\text{s}$  "square topped" pulse through the gauge. The decay constant of the voltage across the supply's capacitor is a

function of the product of the capacitance and the resistance. During the pulse, a measurable decay occurs which has to be taken account of. The circuit is balanced using the variable resistor so that after 50  $\mu$ s the measured voltage is zero. The delay generator is set so that the loading of the gauge occurs at this time. Before each experiment, the gauges are calibrated by putting a series of known resistances in series and measuring the voltage output of the supply.

The initial resistance of the gauge was measured using a standard multimeter, accurate to  $\pm 0.1 \Omega$ , about  $\pm 0.2 \%$  of the gauge resistance. A TDS Tektronix 540 oscilloscope (500 MHz) was used to measure the voltage time history of the experiments. The output is sampled at 8 ns point to point. Using the calibration data the data are converted to a resistance time history. These data are then converted to a stress-time history using the pressure,  $\Delta R/R_0$  relationship discussed in (Rosenberg et al. 1980). The accuracy of this calibration is found to be better than 2 %.

### 3.4 Strain Measurements

There are two basic types of strain gauges namely foil and semi-conductor. Foil strain gauges offer a large linear range, up to 5 % strain. They are relatively insensitive compared to semiconductor gauges which offer a hundred times greater sensitivity but a low range, tending to break at  $\approx 0.2$  % strain.

Considering a foil type strain gauge as a conductor of length  $l$ . The resistance,  $R$ , of this wire is equal to

$$R = \frac{\rho' l}{A} = \frac{\rho' l}{\pi r^2}, \quad (3.9)$$

where  $\rho'$  is the resistivity of the material,  $r$  is the radius of the wire and  $A$  is the cross-sectional area of the wire. Taking logs gives

$$\log R = \log \rho' + \log l - 2 \log r + C, \quad (3.10)$$

where  $C$  is a constant. Considering a small change in length gives

$$\frac{dR}{R} = \frac{d\rho'}{\rho'} + \frac{dl}{l} - 2 \frac{dr}{r}. \quad (3.11)$$

Experimentally, we know

$$\frac{d\rho'}{\rho'} = k' \frac{dV}{V}, \quad (3.12)$$

for metals  $k'$  is approximately 1, where  $V$  is equal to the volume of the wire.

Therefore,

$$\frac{d\rho'}{\rho'} = k' \left[ \frac{dl}{l} + 2 \frac{dr}{r} \right] = k' [1 - 2n] \frac{dl}{l}. \quad (3.13)$$

So,

$$\frac{dR}{R} = 2k' \frac{dl}{l} = G\varepsilon \approx 2\varepsilon, \quad (3.14)$$

where  $G$  is the gauge factor, which is approximately 2 for metals and  $\varepsilon$  is the fractional normal strain.

The strain gauges used were EA-06-031CF-120 (Micromeritics, Basingstoke) consisting of a foil of constantan. They have a 0.03 mm flexible polyimide backing for the sensor elements which are arranged in a rectangle, 1.5 x 1.0 mm. The strain is measured along the 1.0 mm axis (refer to figure 3.4.1). The initial resistance is 120  $\Omega$ , the gauge factor is 2.01 with a linear range up to 3 %. Outside of the 3 % limit, the gauge becomes increasingly less sensitive but can work effectively up to  $\approx 10$  %.

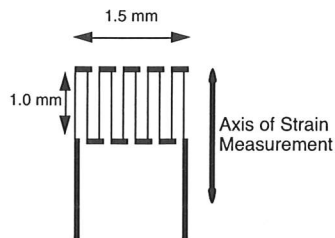


*Figure 3.4.1 The geometry of Micromeritics EA-06-031CF-120 strain gauge.*

### Mounting

The gauges have brass legs soldered to them using a low melting point solder (Micro Measurements 361A-20R-25). A piece of Mylar, 25  $\mu\text{m}$  thick, glued to the legs to prevent shorting against the rod. This Mylar did not lie between the sensing elements and the rod in any way. The gauge was then ready to be fitted to the rod.

The gauges were mounted onto the surface of the 5.5 mm diameter rod using the clamping device shown in figure 3.4.2. An epoxy (Epoxy-patch, Hysol Engineering Co., Seabrook, New Hampshire) was used to attach the gauge to the rod surface. This epoxy was chosen due to the low heat developed during its setting and also its strong adherence to both the rod and the gauge. One of the main problems in mounting of any strain gauge is the adhesive, which must give strong adhesion but not provide extra rigidity to the sample! If too weak a material is used, for example, it will tend to deform elastically under the applied stress, thus shielding the gauge from the sample surface movement and giving a lower response out of the gauge.

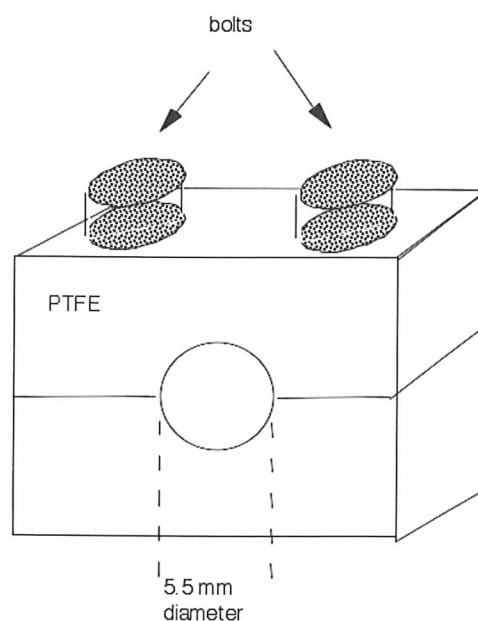


*Figure 3.4.2 Block used in gauge mounting.*

After being left to set for 24 hours, the gauge was then ready for use. Light wires were attached to the brass shims and these connected to BNC cables.

### **Electrical Measurement System Used**

The gauges were powered by a constant current supply, provided by a Dynasen CK2-50/0.050-300, and the measuring circuit is shown below in figure 3.4.3. The supply is set to minimum ringing if the sensor element is set to 50  $\Omega$ , for this reason a parallel resistance of 82  $\Omega$  was introduced. This results in an electrical response time of the

order of 10 ns for the system. However, the gauge has a length of 1 mm, in the direction of measurement, implying the mechanical response time is  $\approx 4 \mu\text{s}$ , if the sound speed in the tungsten is  $\approx 4.0 \text{ mm } \mu\text{s}^{-1}$ .

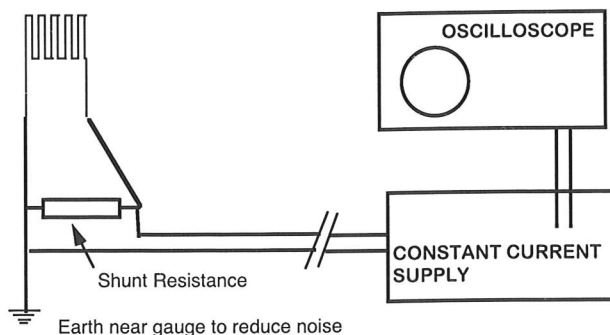


**Figure 3.4.3** *Electrical circuit used.*

The oscilloscope channels were set to  $50 \Omega$  termination matching the power supply termination and reducing ringing at high frequencies on the time scale of the experiment.

### Analysis

Equation (3.14) indicates that a 1 % strain produces a 2 % (or strictly 2.01 %, i.e. gauge factor,  $G = 2.01$ ) change in resistance. The initial resistance of a gauge is  $120 \Omega$ , if the output of the power supply to resistance change is known then the strain can be easily calculated.

Before the experiment, the initial gauge resistance,  $R_{Gauge}$ , and the fixed value of the parallel resistor were recorded. The output voltage response to different in-line resistances placed in series with the gauge. These are fitted with a second order polynomial passing through the origin as  $R_{meas} = aV^2 + bV$ . The resistance versus voltage curve needs only to be fitted up to the maximum voltage attained by the gauge during the experiment.

The change in the total gauge and shunt resistance can be calculated using the calibration data. The second step takes the simple parallel resistance formula as shown in equation (3.15) and rearranges it to give the gauge resistance.

$$\frac{1}{R_{meas}} = \frac{1}{82} + \frac{1}{R_{Gauge}} \quad (3.15)$$

The third step calculates the percentage change in the gauge resistance, divides this by 2.01, the gauge factor, and gives the total strain experienced by the gauge.

Compression reduces the gauge resistance and so is called negative strain while tension tends to increase the resistance and so is called positive strain.

### 3.5 VISAR (Velocity Interferometer System for Any Reflector)

The particle velocity-time history of a specularly reflecting surface during an impact can be determined using VISAR (Barker and Hollenbach 1965). It is important that the surface is not polished to an optical finish because such a finish is unlikely to be preserved at high stress, this unfortunately means that the reflected laser light is spatially incoherent. This technique was developed by Barker and Hollenbach (1972) in the late 60's and early 70's.

The reflected laser light is captured and split into two beams, one of which is passed through a glass cylinder known as an "etalon". Because the refractive index of glass is larger than that of air, the light in this beam is slowed down and delayed with respect to the other beam which passes through air. This set-up is a Wide-Angled Michelson Interferometer (WAMI). If the target is stationary, the interference pattern will not change with time when the two beams are recombined. For an accelerating target, however, the reflected beam will be doppler shifted, due to this change in frequency, there is a beat frequency when the two beams are recombined. Changes in velocity can be measured by recording this interference. The time delay is dependent on the "etalon" length, so it is possible to adjust the system to ensure that an appropriate amount of acceleration per beat (fringe) is obtained.

A change in velocity  $\Delta v$  at the rear can be related to the change in stress by

$$\Delta\sigma = \frac{\rho c \Delta v}{2}, \quad (3.16)$$

where  $\rho$  is the density of the material and  $c$  is the elastic wave speed.

The time resolution of the VISAR data is 2 ns and the noise on the photo-multiplier produces an error of  $\pm 5\%$ . A duplex fibre-optic is mounted in a plastic holder close ( $< 10$  mm) behind the target with one fibre to supply the incident light and the other to collect the reflected light. The movement of the target towards the fibre-optic changes the intensity of the collected light. This is compensated for by the system which has

an internal measure of the intensity independent of the two interfering beams. Eventually when the target-fibre distance is about 3 mm, accurate measurement is no longer possible. However by this point the sample is no longer under shock loading.

### 3.6 High-speed photography

The Ultramac FS501 was used in conjunction with a Bowen 400 E Monolite flash. The flash is a professional photographic type. It takes  $100 \mu\text{s}$  to illuminate fully after triggering and maintains a fairly constant light level for about  $500 \mu\text{s}$ . In these experiments, the illumination was diffuse and the images back-lit. The diffuser consists of a variable number of sheets of tracing paper.

The camera is an image converter type capable of operating at framing rates of up to twenty million frames per second. Twenty-four frames may be recorded and each can be individually programmed in terms of exposure and inter-frame times. The images are captured using Kodak 667 film, which is pressed against a phosphorescent fibre-optic plate when the camera is operating. The images are on a raster in order to minimise the distance the electron beam carrying the image has to move and this results in the images needing to be read in a zigzag fashion as shown in figure 3.6.1. In this research, either 24 frames were taken at  $4 \mu\text{s}$  intervals or 12 frames were taken at  $10 \mu\text{s}$  intervals.

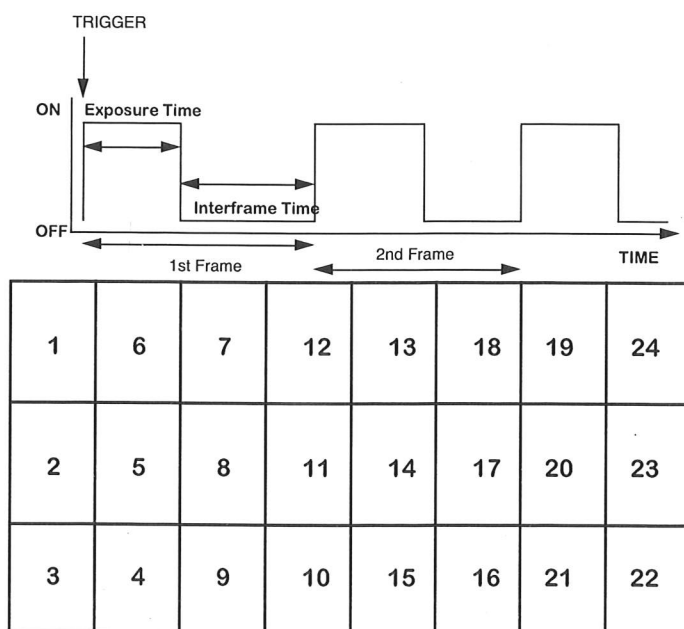


**Figure 3.6.1** Schematic of high-speed record of Ultramac FS501 and illustration of exposure and interframe times.

### 3.7 The small gas gun

For classic Taylor impacts studies the set-up is shown in figure 3.7.1 was used. The firing vessel can be filled with either helium or nitrogen to the required pressure for the shot, and when the gun is fired fast-acting valves open and propel the projectile. The impact chamber and barrel are evacuated to 100 mbar prior to the firing. Projectiles of a few grams can be fired at velocities of up to  $1.4 \text{ km s}^{-1}$ .

The velocity of the projectile is measured by use of a velocitometer. This consists of two low power laser diodes the output of which can be fed into either a specially constructed timer or into an oscilloscope. During the shot the projectile cuts these light beams, which are a known distance apart. The velocity can then be calculated to an accuracy of  $\pm 1 \text{ m s}^{-1}$  using a counter timer.

The output of the timer can be sent to a Multi-Channel Delay Generator the output of which can be used to trigger the diagnostics, (photography or gauges etc.) as required.

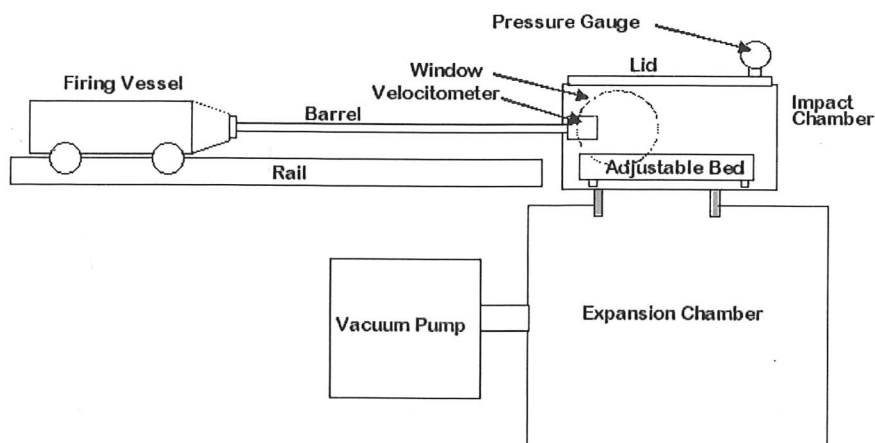


*Figure 3.7.1. Schematic of experimental set-up of the single stage small gas gun.*

### 3.8 Microstructural studies

#### Optical microscopy

Preparation of samples for optical microscopy is an important technique, it requires care since if sample preparation is performed incorrectly, it can lead to the wrong conclusions about a material's structure.

Both bainitic steel and tungsten alloy samples were sectioned using a hacksaw, abrasive cutter or diamond wheel when possible, otherwise they were cut by spark erosion. It is important to remember that after sectioning, the microstructure near to the cut may well have been damaged in some way. Therefore for the bainitic samples, after sectioning, the material was etched chemically with 4 % nital (4 % nitric acid, 96 % ethanol) before grinding.

After sectioning, the samples were ground to ensure that material with damaged microstructure was removed. In the metals considered in this work the damaged zone is likely to be less than 100  $\mu\text{m}$  deep (Vander Voort 1999). Often when grinding and polishing it is advantageous to mount the sample and a cold setting resin is used. Grinding was carried out using a series of grit papers starting out with the coarsest first, grit papers commonly available include 60, 120, 240, 320, 400 and 600 mesh grit paper. Water was used as coolant and lubricant since it removes loose abrasive and cutting debris and therefore reduces clogging which could lead to smearing or burnishing of the surface.

After grinding, samples were then polished using diamond paste, 30  $\mu\text{m}$  down to 1  $\mu\text{m}$ , on a polishing cloth. Again the abrasive agent is usually water-based. However for the bainitic samples considered in this research it was found that due to their high hardness the period of time required for grinding and polishing allowed rust to form on the sample unless oil based lubricants and polishing pastes were used.

When performing microscopy on a sample, it is important that there is good contrast between different zones of the microstructure. Contrast can be improved by etching or use of Nomarski interference-contrast.

The bainitic samples examined in this research were etched using 0.5 % nital which stains the grain boundaries. Thus the microstructural detail is enhanced. From the shape and size of the grains revealed, an idea of the phases present and in what fraction can be observed.

Tungsten alloys can be etched with boiling hydrogen peroxide, however the detail required in this work could be observed using Nomarski interference-contrast. Polarised light is used with the two beams created by a double quartz prism with the polarizer and analyser crossed. The prism is placed between the objective lense and the source of illumination. The two beams created by the prism interfere in the image plane and produce two laterally displaced images differing in phase by half a wavelength, thus producing height contrast. This technique is ideal for observing grain shapes but not the detail within the grain.

Images can be recorded either digitally or on black and white photographic film with the latter giving better resolution.

### **Electron microscopy**

There are two main types of electron microscopy, SEM (Scanning Electron Microscopy) and TEM (Transmission Electron Microscopy). More recently combining the two to give a STEM (Scanning/Transmission Electron Microscope) has become increasingly popular.

The production of samples for TEM is extremely lengthy and therefore only SEM was used in this research. The main advantages of SEM over optical microscopy are that the depth of focus is much larger, meaning that fracture faces can be examined, and the resolution is much better. Images were recorded digitally. The SEM used in this research was a FEI Philips XL30 sFEG.

## Hardness

Hardness is a fundamentally simple concept, however it cannot be defined rigorously or measured accurately. The main problem is that the service conditions and the test conditions do not match and are difficult to relate to one another. Despite this, hardness measurements are widely used because they are both easy and cheap to carry out. (Tabor 2000) provides an excellent review of the area.

One of the most common methods of measuring hardness is by indentation. Test conditions can be accurately controlled and reproduced so materials can easily be compared. A hardness number can be calculated from the applied load and the area of the impression. The indentation size depends on the hardness of the material, the applied force and time of application as creep can occur over long time periods. Hence standardised 'static' indentation tests are frequently used, examples of which are Rockwell, Vickers or Brinell.

Brinell hardness tests involve a 10 mm diameter indenter pressed into the sample for 30 s. Brinell used the surface area of the indent instead of the projected area see (Wahlberg 1901a; Wahlberg 1901b), Meyer showed that correcting for this is fairly simple (Meyer 1908) but is not usually done due to the popularity of Brinell hardness. The load used depends on the hardness of the material under consideration.

Unfortunately Brinell testing requires quite a lot of time, large indentation and is not suitable for hard materials. The Vickers test uses a square-based pyramidal diamond indenter (Smith and Sandland 1925). The angle between opposite sides,  $\alpha$ , was chosen to be  $136^\circ$  so that hardness numbers are similar in magnitude to Brinell numbers. The loading time used is 10 to 15 s, the load chosen depends on the hardness of material being tested. After removal of the load, both diagonals of the indent are measured and the average value,  $d$  in mm, and the Vickers hardness,  $HV$ , can be calculated.

$$HV = \frac{2L \sin(\alpha/2)}{d^2}, \quad (3.17)$$

where  $L$  is the applied load in kgf (kilograms-force).

In 1919, Rockwell, a metallurgist, invented the Rockwell tester (Rockwell 1922). Initially a minor load of 10 kg is applied via the sphero-conical diamond indenter, Whilst this is still being applied, the major load, the magnitude of which is dependent on the hardness of the material being tested, is applied. Because the hardness is determined by the incremental change in penetration depth upon application of the major load, elastic recovery effects are reduced and the effect of deflection of the tester is removed from the results.

The hardness tests considered so far give an average value for the area tested. Micro-indentation tests are necessary for resolution of changes of hardness across a microstructure. Lower loads are used with smaller indentors. Micro-hardness testing is reviewed in (Mott 1956) and (Buckle 1959). One drawback with micro-hardness testing is that sample preparation is more lengthy, a better quality finish is required than the simple requirement of a flat sample for most hardness tests.

Each testing method has its own range of applications, however it is still possible to convert between these using conversion tables which are found in ASTM Standard E140.

More recently, developments in the field have been mainly for ergonomic reasons. Automated systems have been developed that can do entire microhardness traverses. The machine used in this research was a Mitutoyo HKV-3 which was not fully automated. All hardnesses quoted in this dissertation are in Vickers numbers. A hardness of around 700 HV is a very hard material, a soft steel would typically be about 200 HV.

### **X-ray analysis**

X-ray diffraction was carried out, with a Philips E'Pert PW 3020, using a rotating crystal method. This allowed Rietveld analysis to be carried out to determine the volume fraction of different phases present. This software was a X'Pert Plus Rietveld routine. A database of different crystal structures was used in this analysis. The

bainitic samples needed 10 to 14 hours in the X-ray diffractometer before enough data were collected; the grains in the bainites are very small and scatter the radiation very effectively!

## References

- Barker, L. M. and R. E. Hollenbach (1965). "Interferometer technique for measuring the dynamic mechanical properties of materials." Rev. Sci. Instrum. **36**(11): 1617-1620.
- Barker, L. M. and R. E. Hollenbach (1972). "Laser interferometer for measuring high velocities of any reflecting surface." J. Appl. Phys. **43**(11): 4669-4675.
- Buckle, H. (1959). "Progress in micro-indentation hardness testing." Met. Rev. **4**(13): 49-100.
- Meyer, E. (1908). "Contribution to the knowledge of hardness and hardness testing." Z. Ver. Dtsch. Ing. **52**: 645-654; 740-748; 835-844.
- Mott, B. W. (1956). Micro-indentation hardness testing. London, Butterworth Scientific Publications.
- Rockwell, S. P. (1922). "The testing of materials for hardness." Trans. Am. Soc. Steel Treat. **11**: 1013-1033.
- Rosenberg, Z. and Y. Partom (1985). "Lateral stress measurement in shock-loaded targets with traverse piezoresistance gauges." J. Appl. Phys. **58**(8): 3072-3076.
- Rosenberg, Z. and Y. Partom (1985). "Longitudinal dynamic stress measurements with in-material piezoresistive gauges." J. Appl. Phys. **58**(5): 1814-1818.
- Rosenberg, Z., D. Yaziv and Y. Partom (1980). "Calibration of foil-like manganin gauges in planar shock wave experiments." J. Appl. Phys. **51**(7): 3702-3705.
- Smith, R. L. and G. E. Sandland (1925). "Some notes on the use of a diamond pyramid for hardness testing." J. Iron Steel Inst. **111**(1): 285-304.
- Tabor, D. (2000). The hardness of metals, Oxford University Press.
- Vander Voort, G. F. (1999). Metallography, principles and practice, ASM International.
- Wahlberg, A. (1901a). "Brinell's method of determining hardness and other properties of iron and steel." J. Iron Steel Inst. **59**(1): 243-298.
- Wahlberg, A. (1901b). "Brinell's method of determining hardness and other properties of iron and steel." J. Iron Steel Inst. **60**(2): 234-271.

## Chapter 4

### Shock properties of bainitic steels

The materials considered in this research were chosen as examples of upper and lower temperature bainite, as discussed in chapter 2. The latter being a steel in which the carbide formation has been hindered by the silicon content of the material, (Bhadeshia 1999; Bhadeshia 2001; Caballero et al. 2001a; 2001b; 2002). The two bainites were both of similar low-alloy composition which are given in chapter 2, along with details of the heat treatments.

At high pressures,  $\epsilon$ -iron which is hexagonal close packed can be obtained (Barker 1975). This transition causes a change in specific volume of the material allowing the phase transition to be monitored by measuring the stress. An excellent discussion of phase transitions occurring at high dynamic pressures is found in (Duvall and Graham 1977) while a more general review of shock compression is found in (Graham 1992). In this research, the  $\epsilon$  phase exists only during the shock compression and is unlikely to be observable post-impact, though some change in the recovered microstructure may be found. An excellent discussion of the microstructural changes that would be expected to be observable is (Murr and Meyers 1983).

The shock properties of the two bainitic steels were determined. In this chapter, this research is discussed. It is divided into five main sections;

- Measurement of static properties,
- Measurement of the Hugoniot,
- Measurement of lateral stresses and subsequent calculation of shear strength,
- Measurement of the dynamic tensile, or spall, strength and
- Microstructural and macroscopic damage studies.

## 4.1 Measurement of static properties

The physical properties of the two alloys and also mild steel (Millett et al. 1995) are given in table 4.1. As can be seen, there is little difference in the density and wave speeds. The hardness is significantly different and reflects the fineness of the microstructure, the density of precipitates as well as dislocations and other defects. Lower temperature bainite, which has the finest microstructure of the materials considered, was found to have a hardness comparable to that of a martensitic steel: an extremely brittle and hard microstructure. The advantage of lower temperature bainite is that it maintains the hardness and high strength but is less brittle than a martensitic alloy. Upper bainite, whilst being relatively hard, has a hardness value that is more usual for a ferrous alloy (Bhadeshia 2001; Caballero et al. 2001a; 2001b).

Material Property	Lower temperature bainite	Upper bainite	Mild steel
Longitudinal sound speed, $c_l$ , ( $\pm 0.005 \text{ mm } \mu\text{s}^{-1}$ )	5.85	5.87	5.91
Shear sound speed, $c_s$ , ( $\pm 0.005 \text{ mm } \mu\text{s}^{-1}$ )	3.18	3.20	3.25
Bulk sound speed, $c_0$ , ( $\pm 0.01 \text{ mm } \mu\text{s}^{-1}$ )	4.55	4.56	4.57
Poissons ratio ( $\pm 0.006$ )	0.290	0.289	0.283
Density, $\rho_0$ , ( $\pm 20 \text{ kg m}^{-3}$ )	7740	7760	7820
Hardness (HV10, $\pm 5 \text{ kg mm}^{-2}$ )	703	468	~250

**Table 4.1** The static properties of lower temperature and upper bainites and also mild steel.

## 4.2 Measurement of the Hugoniot

### Experimental

Impact conditions were selected to cover a wide range of stresses. This was achieved by varying both the impact velocity and also the impacting material. The velocities used were in the range 250 to 1000 m s<sup>-1</sup>. For the highest velocity impacts, tungsten alloy flyers were used; the high impedance ensuring a higher stress on impact for a given velocity than would be achieved using other, lower impedance, materials. The tungsten alloy was a commercial sintered and heat treated alloy containing 92.5 % tungsten with the balance being Ni, Fe and Co. This material was characterised by (Millett et al. 1996) and others in the group. Copper flyers were used for all other shots.

Stress and particle velocity were measured using a combination of manganin gauges and VISAR. The gauge configuration is shown in figure 4.2.1. It should be noted that gauges can also be used as time of arrival sensors, so measuring the shock velocity,  $U_s$ . Therefore data are obtained even if the gauge should not record a stress history.

VISAR was used for the highest velocity shots not only as a comparison to the gauges, but also to give better time resolution. The duplex fibre was mounted about 10 mm from the rear surface. It reflected off the bainite/PMMA interface and was centred away from the gauge location to prevent any gauge heating. It has a spot diameter of approximately 5 mm.

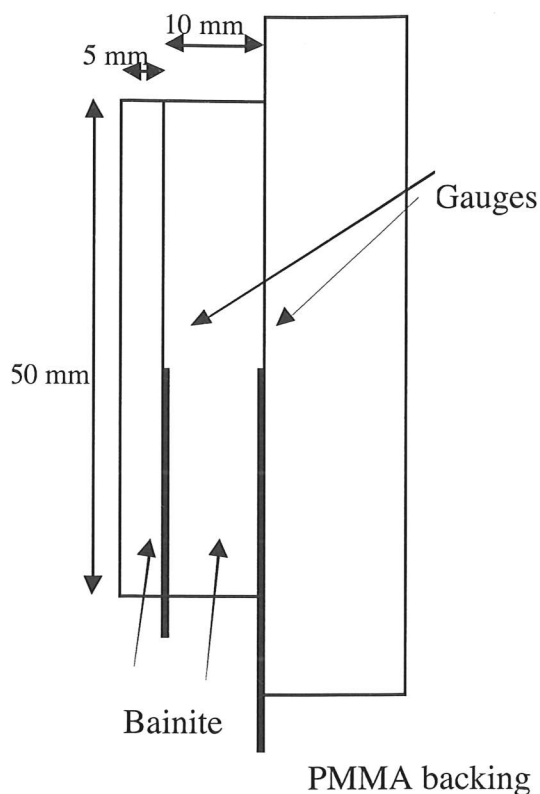


**Figure 4.2.1** Gauge configuration used for Hugoniot experiments.

The embedded stress gauges recorded the maximum stress in the material accurately but impedance differences between the sample and the epoxy/gauge package, the stress must ring up (figure 4.2.2). Overall this produces a time resolution of 200 ns. This was not sufficient to resolve the HEL or the phase transition in the material. Better time resolution (30 ns) is achieved in the back-surface gauge and artifacts in the trace are more readily observable. However, the transmission coefficient of the interface must be known (chapter 1).

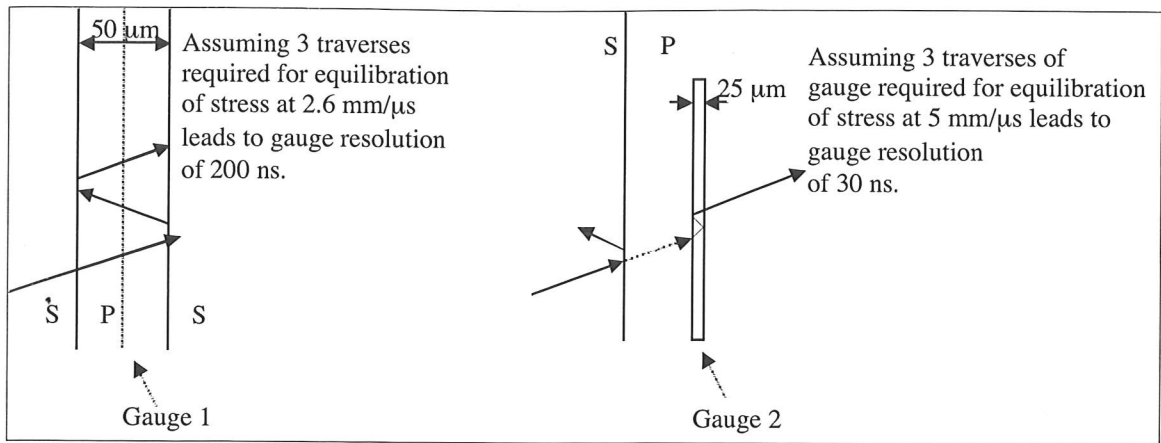


**Figure 4.2.2** Schematics of gauge conditions and calculation of time resolution by use of impedance matching.

## Results

Typical longitudinal stress histories are shown in figures 4.2.3 and 4.2.4. The back-surface gauge traces for the lower temperature bainite samples clearly show both the HEL and the phase transition. When converted by impedance matching to stress levels in the bainite itself, the HEL was found to be at  $3.5 \pm 0.5$  GPa and the phase transition occurred at  $13 \pm 0.5$  GPa. For the maximum stress shot, VISAR was also used. Figure 4.2.5 shows the resulting trace, which clearly shows both the HEL and the phase transition.

The back-surface gauge trace for the upper bainite clearly shows the HEL, which is at  $2 \pm 0.5$  GPa, but does not show the phase transition.

Figure 4.2.6 shows the Hugoniot curves for the two materials. The curves deviate from the elastic line at stresses near the phase transition. The curves then approach the elastic line as the system heads towards "overdrive". This is the point at which the shock front is a single wave of higher velocity than the elastic wave. For the highest stress impact on each material, there are two data points, one derived from the VISAR and the other from the stress gauge. Within experimental error these points are in agreement. The average for each experiment is presented in this research.

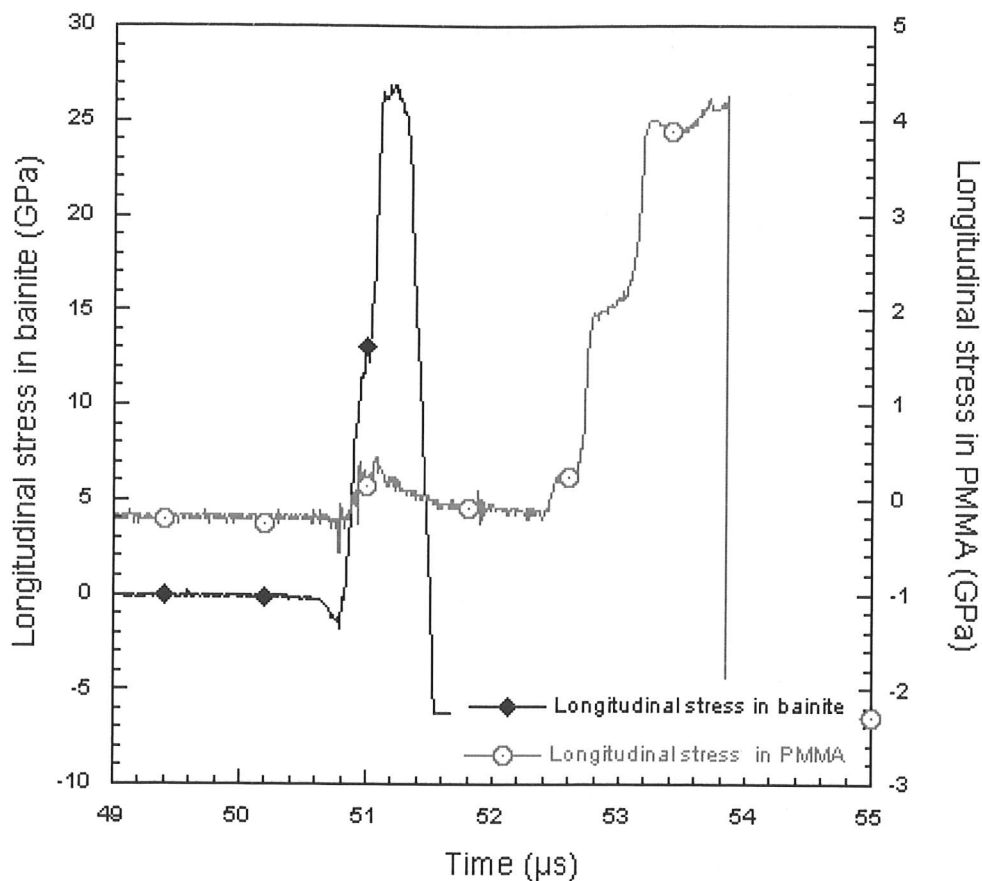


*Figure 4.2.3* Typical gauge traces for a Hugoniot experiment on lower temperature bainite. Here a tungsten impactor with velocity  $965 \text{ m s}^{-1}$  was used. The stress in the PMMA clearly shows plateaux at both the HEL and phase transition.

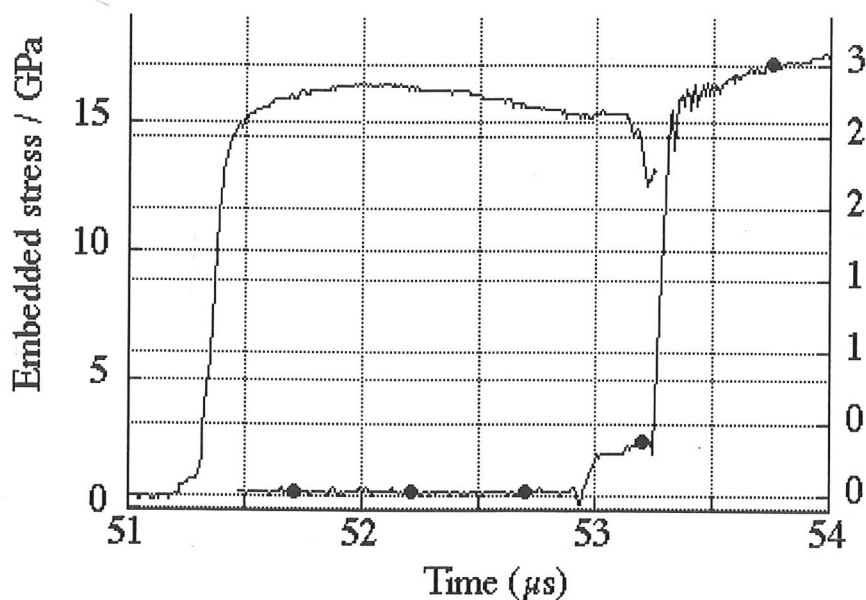


*Figure 4.2.4* Typical gauge traces for a Hugoniot experiment on upper bainite. A copper impactor with velocity  $842 \text{ m s}^{-1}$  was used.

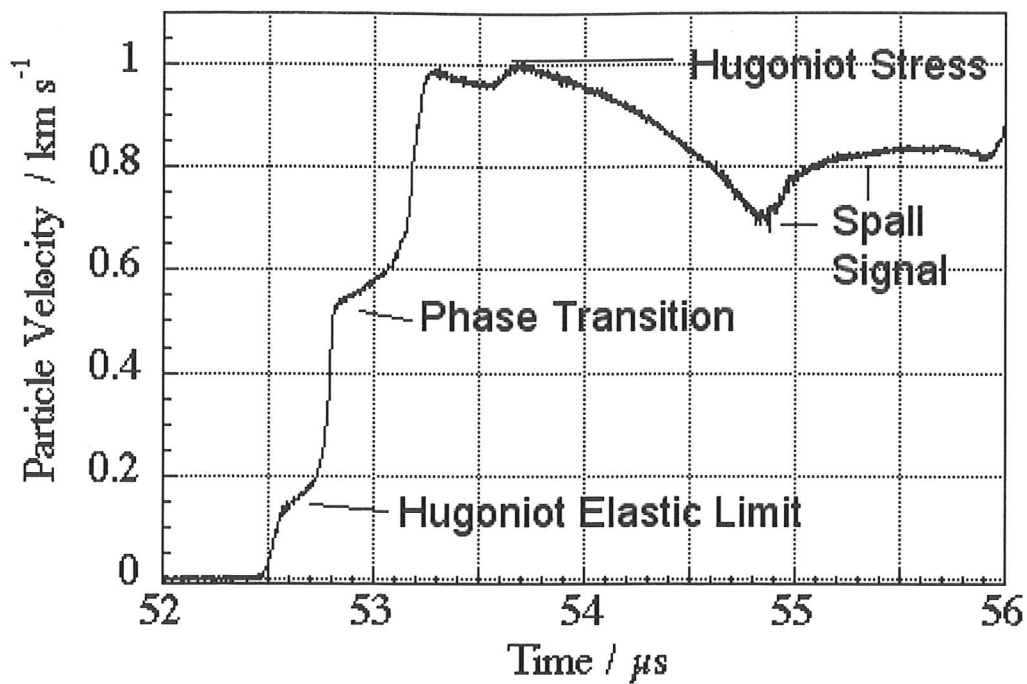


Figure 4.2.5 VISAR trace for impact of tungsten at  $965 \text{ m s}^{-1}$  onto lower temperature bainite.

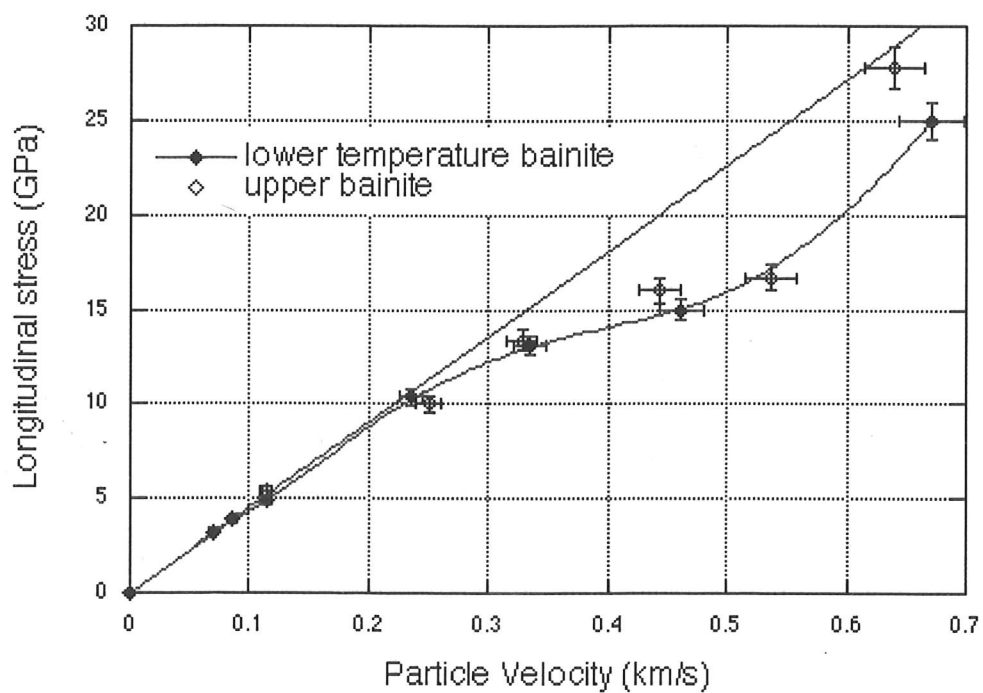


Figure 4.2.6 Hugoniot curves lower temperature bainite and upper bainite. The elastic line for both materials is also plotted.

## Discussion

The Hugoniot curves for the two materials were found to be similar to one another. The phase transition found in the lower temperature bainite was at a comparable stress to that found in other work (Barker and Hollenbach 1974; Millett et al. 1997). However the phase transition was not observed in the upper bainite. Upper bainite was found to be almost entirely ferritic, hence the phase transition should have been more evident than that of the lower temperature bainite. For these low alloy steels, the effect of alloying additions on the phase transition stress should be minimal.

The  $\alpha$ - $\epsilon$  phase transition is martensitic, nuclei can form rapidly. Such a nucleation event was found to take 55 ns (Meyers 1979) and is therefore well within the timescale of the impact. Martensitic transformations can occur at velocities approaching the speed of sound in the material as they rely on dislocation motion (Honeycombe and Bhadeshia 1995), the presence of grain boundaries and other defects may reduce the transformation velocity; hence the grain size may have an effect. This will be considered in section 4.6.

The reason that the HEL of upper bainite is significantly lower than that of the lower temperature bainite may be associated with the dislocation density and carbide precipitation distribution as discussed earlier.

### 4.3 Lateral stress measurement and calculation of shear strength

Lateral stress measurements were carried out using the same impact conditions as for the Hugoniot experiments. The configuration is shown in figure 4.3.1. The shear strength of the two materials was calculated, as discussed in section 1.1, and the results are shown in figure 4.3.3.

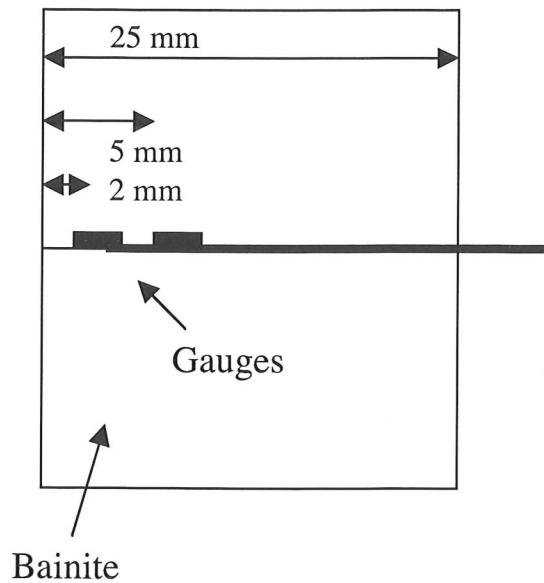


*Figure 4.3.1 Gauge configuration for lateral experiments. Each half of the sample measured 25 mm by 25 mm by 50 mm before being glued together to create a 25 mm by 50 mm by 50 mm target. The gauge positions were accurate to  $\pm 0.2$  mm.*

#### Results

Figure 4.3.2 shows typical lateral gauge traces. The two materials behave similarly. The HEL was exceeded in all impacts but was not resolvable in the lateral gauge traces. Figure 4.3.3 shows the shear strength of the materials. The shear strength is equal to half the difference between the longitudinal stress and the lateral stress at a given impact condition. No lateral stress measurements were recorded above the phase transition. Studies of the survivability of lateral gauges are discussed in chapter 7, these involve incorporating extra “padding” around the gauge. The effect of different degrees of this “padding” has been quantified (Hammond et al. 2003). As the thickness of the padding is increased, there is at first a drop off in the measured value of  $\Delta R/R_0$  of 10 to 15 %. This is followed by a plateau up to a thickness of circa 0.5

mm on either side of the gauge. Beyond this there is a significant drop in  $\Delta R/R_0$  values as the thickness is increased further, refer to chapter 7 for a full discussion of this research.

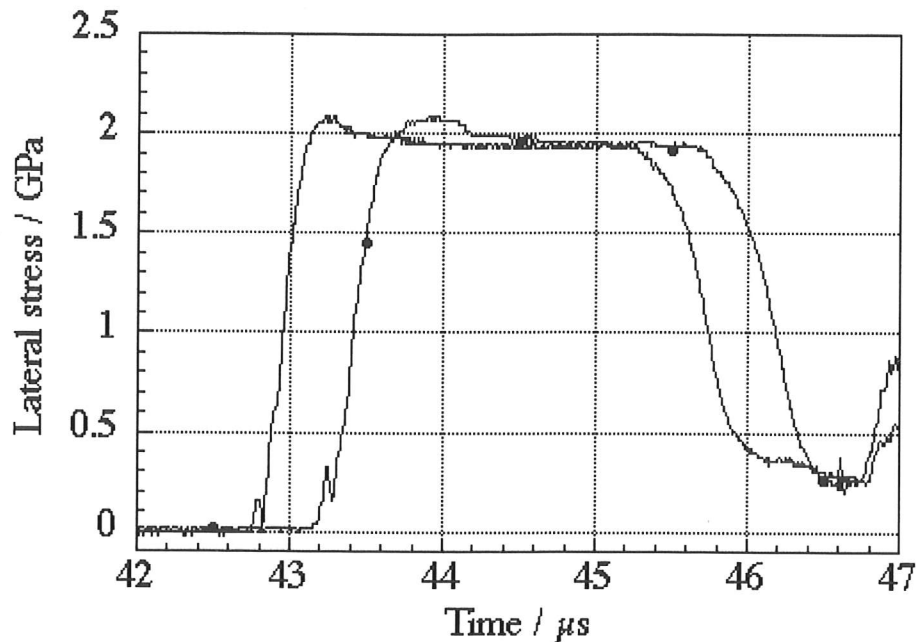


Figure 4.3.2 Lateral stress time histories from impact on the lower temperature bainite using a copper projectile at  $259 \text{ m s}^{-1}$ .

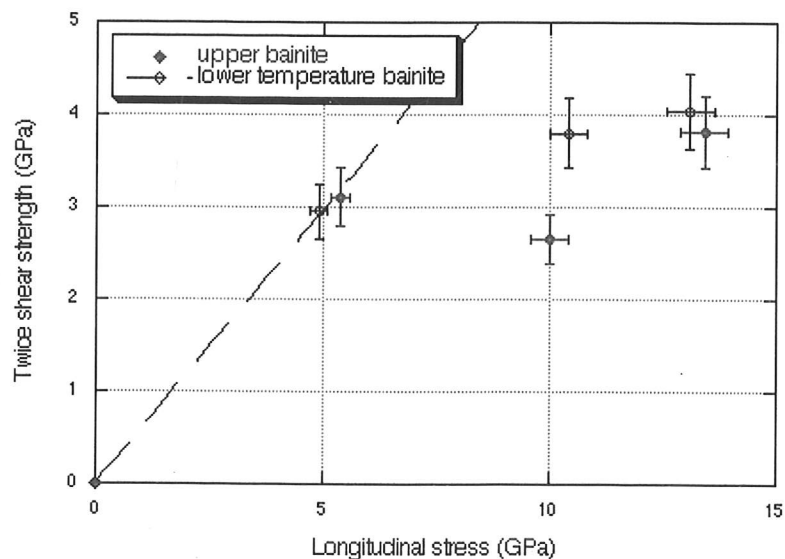


Figure 4.3.3 A plot of the shear strengths against longitudinal stress for both the lower bainite and the upper bainite. The elastic line for the lower bainite is also shown, on this scale it is indistinguishable from the elastic line for the upper bainite.

## **Discussion**

The lateral stress data showed the two materials undergo similar stresses for the same impact conditions (figure 4.3.2). The shear strength of the lower temperature bainite was found to be similar than that of the upper bainite (figure 4.3.3) over the stress range considered.

For both materials, the shear strength versus longitudinal stress plot shows the materials deviating from the elastic line at a longitudinal stresses above 5 GPa, higher than the elastic limit in either material but lower than the phase transition stress. It does not correspond to the point at which the Hugoniot curve deviates from the elastic.

Both materials display dynamic response, transverse and lateral, that is similar to previously published data for mild steel (Millett et al. 1997).

## 4.4 Spall strength

Spall experiments were carried out on both bainites over a range of impact velocities using VISAR as the diagnostic tool. For all but two of the experiments, a 5 mm thick sample was impacted by a 3 mm copper flyer. The remaining two shots (carried out at  $367 \text{ m s}^{-1}$  and  $365 \text{ m s}^{-1}$ ) used a 5 mm copper flyer impacting a 10 mm thick target.

### Results

Data were collected in the form of VISAR traces (see figures 4.4.1 and 4.4.2). The position of the spall plane can be found by examining the time of reload, which can be compared to the actual measured values on the sample.

Several reload signals were clearly visible in many of the traces, the spall strengths, in  $\text{km s}^{-1}$ , could easily be read off each of the traces (figures 4.4.1 and 4.4.2). From these values the spall or dynamic tensile strength, in GPa, could be calculated with knowledge of the Hugoniot found earlier, refer to Section 4.2. These spall strengths are plotted against longitudinal stress in figure 4.4.3.

The position of the spall plane can be found using the time between reloads, these were found to agree with the actual measured values on the sample.

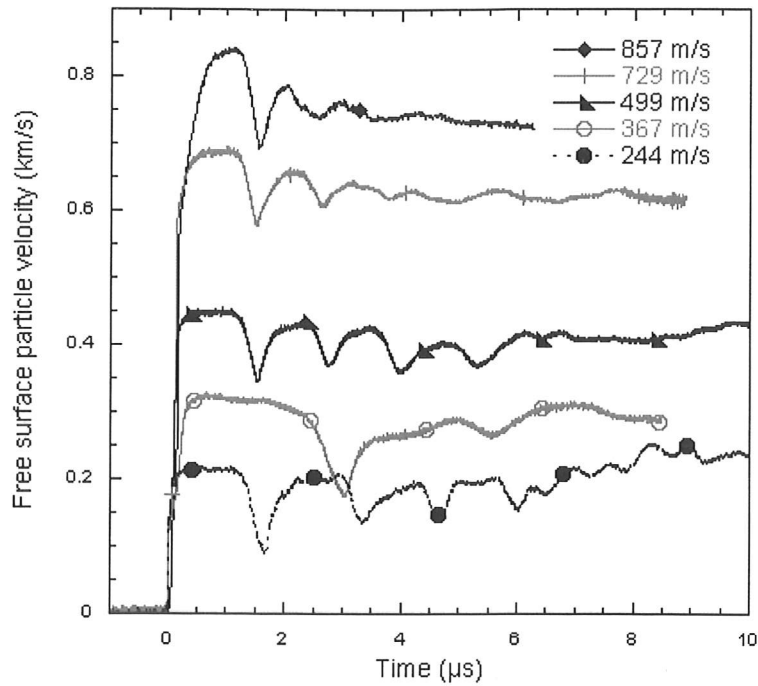


Figure 4.4.1 VISAR traces for spall experiments on lower temperature bainite. The experiment at  $367 \text{ m s}^{-1}$  used a 10 mm thick plate, all others were 5 mm.

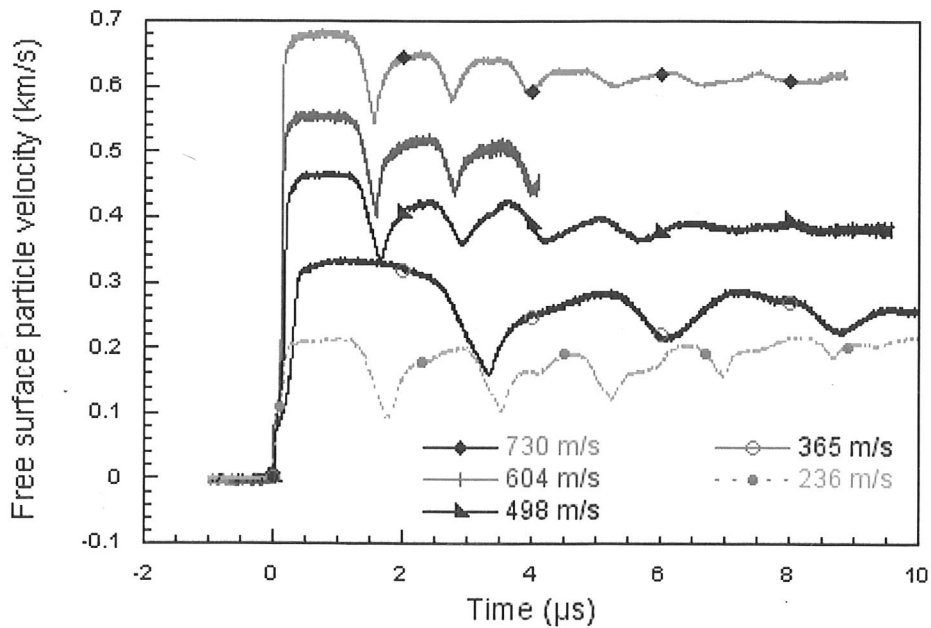
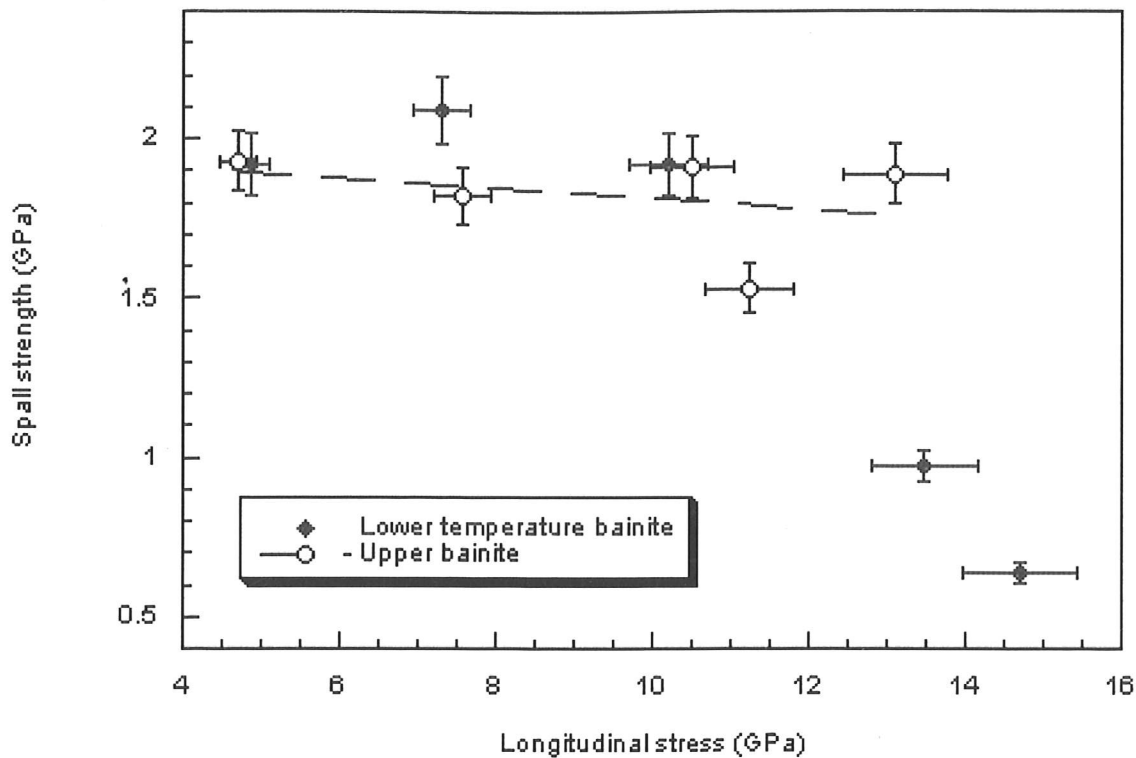


Figure 4.4.2 VISAR traces for spall experiments on upper bainite. The experiment at  $365 \text{ m s}^{-1}$  used a 10 mm thick plate, all others were 5 mm.



**Figure 4.4.3** Spall strength plotted against longitudinal stress for the two bainites.

The quasi-static yield stress values for lower temperature bainite and upper bainite are 2.5 GPa and 1.6 GPa respectively. For the upper bainite, as would be expected, the dynamic values (circa 1.9 GPa) are greater than the static ones throughout the region of longitudinal stress considered. However this is not the case for the lower temperature bainite which has a spall strength of approximately 2 GPa falling to 0.5 GPa above the phase transition stress. A possible cause of this is that the lower temperature bainite is significantly more brittle than the upper bainite. When the shock wave first travels through the material it causes it to be weakened by forming a number of fracture nucleation sites. When spall occurs in this pre-shocked material, the dynamic tensile strength is found to decrease with increasing longitudinal stress. The phase transition itself causes a change in specific volume in the material; this process could cause microstructural damage. It could also be that the  $\epsilon$ -phase is weaker. Interestingly, in pure single crystal  $\alpha$ -iron, the spall strength was found to increase at the phase transition stress (Veiser et al. 1999), this observation agreeing with previous work (Murray 1996). However analysis of the data found in (Church et al. 2001) shows that AQ80 steel, a very soft ductile material, has a spall strength

which, within experimental error, does not vary with longitudinal stress at the stresses considered.

Either the phase transition is being suppressed or is not observable. The main difference between the two materials is microstructural, it follows therefore that this is almost certainly the reason. It is probably an effect of grain size or precipitate content and distribution. These may cause the change in specific volume at the phase transition to be reduced in some cases, thus making the phase transition more difficult to observe using stress gauges. No references have been found that indicate that other researchers have suppressed the phase transition in ferrite to pressures as high as than those considered in this study.

## 4.5 Recovered debris

Over the range of impact conditions reported in this work, lower temperature bainite exhibited brittle fracture, often leaving the sample in a great number of pieces (figure 4.5.1). Upper bainite samples were recovered mostly intact (figure 4.5.2). For the higher stress impacts (Hugoniot and lateral stress measurements), spall was also observed in both bainites.



*Figure 4.5.1 Debris of lower temperature bainite Hugoniot sample recovered post-impact at  $669 \text{ m s}^{-1}$  by a copper impactor.*

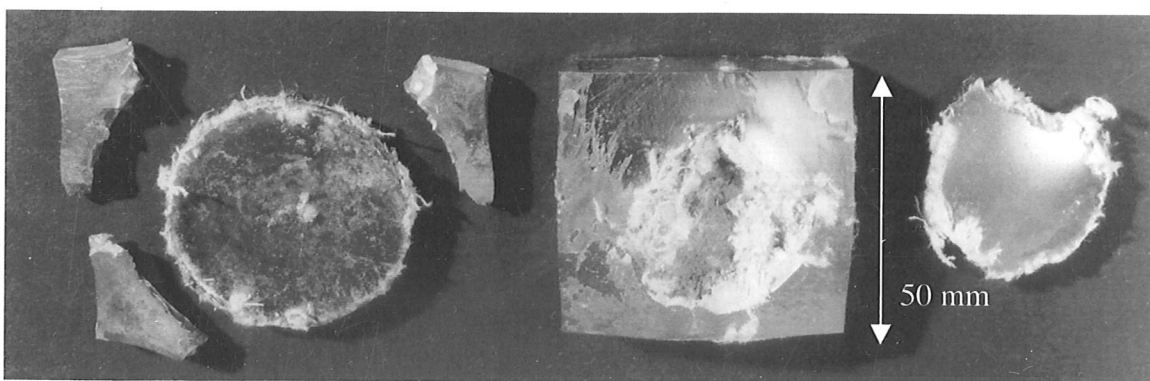


*Figure 4.5.2 Upper bainite Hugoniot sample debris recovered after impact using a tungsten projectile with velocity  $732 \text{ m s}^{-1}$ . The 10 mm thick rear plate is in the centre of the figure, the spalled section on the right and the 5 mm thick front plate is on the left.*

There has also been some controversy as to whether spall occurs within one plane or in a zone as discussed in Johnson et al. (1995). Johnson found that the spall zone

extended over a distance of the order of tens of microns. Certainly in this research, voiding and cracking were observed over such a zone. Hardness measurements made in this area yielded interesting results; refer to section 4.6. This effect is probably due to the spreading of the release fans.

The lower temperature bainite exhibited brittle fracture on impact whereas the upper bainite exhibited much more ductile behaviour. This can be explained by considering the heat treatments received by each material and the resulting microstructure. It is possible that the upper bainite was held at a high enough temperature for the carbon to diffuse out of the ferrite by interstitial, producing carbide-free ferrite plates. At this holding temperature, recovery in the ferrite may also reduce the dislocation density. The lower temperature bainite was held at a much lower temperature. It is likely that as with the upper bainite, carbides form in the phase between the ferrite plates. Unlike lower bainite, in this alloy the precipitation of the carbides is suppressed by the addition of silicon so there are no carbides within the ferrite plates themselves. It is thought unlikely that recovery, a process during which dislocations are rearranged or annihilated in order to reduce the free energy of the material, would have had a significant effect on the dislocation density. In a material, such as lower temperature bainite, with a high dislocation density, slip systems are likely to become locked due to dislocation pile-ups producing brittle fracture results and high hardness. The upper bainite having a lower dislocation density and less carbide precipitates in the ferrite plates would be more able to flow plastically and hence fail in a more ductile manner.

## 4.6 Microstructural studies

### X-ray analysis

Rietveld analysis on the X-ray diffraction data showed that the lower temperature bainite is 85 % ferrite and 15 % austenite. Upper bainite was found to be almost 100 % ferritic. Post impact, any changes in these values were within experimental error (refer to figures 4.6.1 and 4.6.2 for an example of each bainite post-impact).

### Hardness

Micro-hardness traverses were taken on a selection of the debris recovered post-impact. The measurements are given as Vickers Numbers (HV), each measurement used a 1 kg load for a duration of 10 s. A comprehensive investigation into peak dynamic pressure and material type was carried out. A selection of the data yielded by these traverses is shown in figure 4.6.1, the average hardness value from each sample and also of unimpacted material is plotted in figure 4.6.2. The spread in the data from the unimpacted materials gives an error of roughly  $\pm 10$  HV. This could be accounted for by either user error or non-uniform material hardness.

Figure 4.6.3 shows micro-hardness traverses from four samples. These were recovered after an impact event whose impact velocity is indicated in  $\text{m s}^{-1}$  in the legend of the figure. There are two examples of each of the bainites, one of which was not recovered whole so not all traverses cover the full 25 mm depth of the sample. In each case there is a large appearance of scatter in the data. Some of this can be attributed to user error; however, the material may well be "patchy" in its hardness. There are some trends that may result from a change in the dislocation density that was caused by the impact event. In the 15 to 20 mm region, a number of the samples exhibited an increase in hardness compared to the rest of the trace. This coincides with the position of the spall plane in those sample that exhibited spall, those that did not still show some increase in this region. In fracturing a sample dynamically, as occurs during the spall process, there is some amount of work done in tearing the sample and in creating new dislocations. Since the hardness gives an indication of the dislocation density within a material it is inevitable that hardness is increased at and

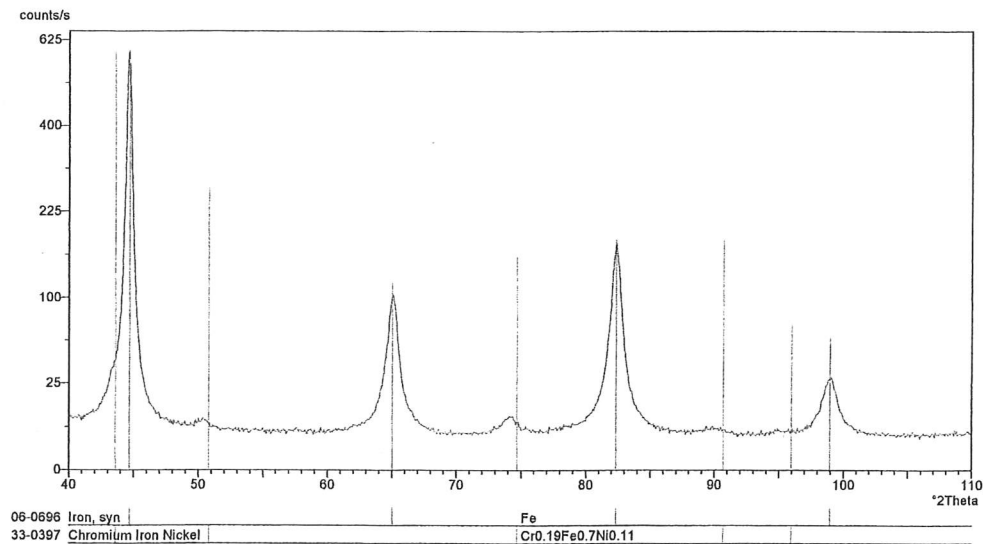


Figure 4.6.1 X-ray diffraction plot for upper bainite post-impact by tungsten flyer at 732 m s<sup>-1</sup>. This plot is typical of all the plots recorded for upper bainite, both before and after impact.  
X-ray wavelength 1.54056 Å

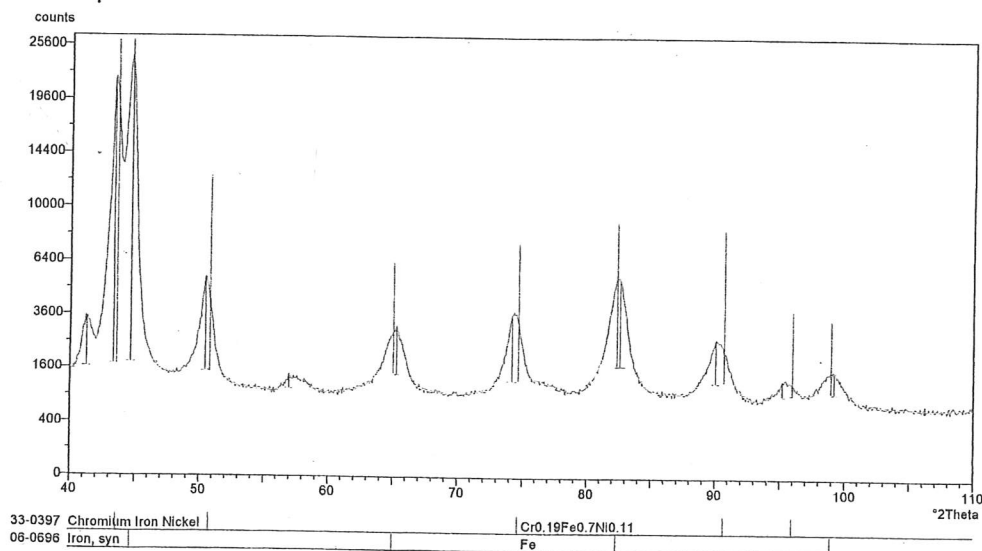
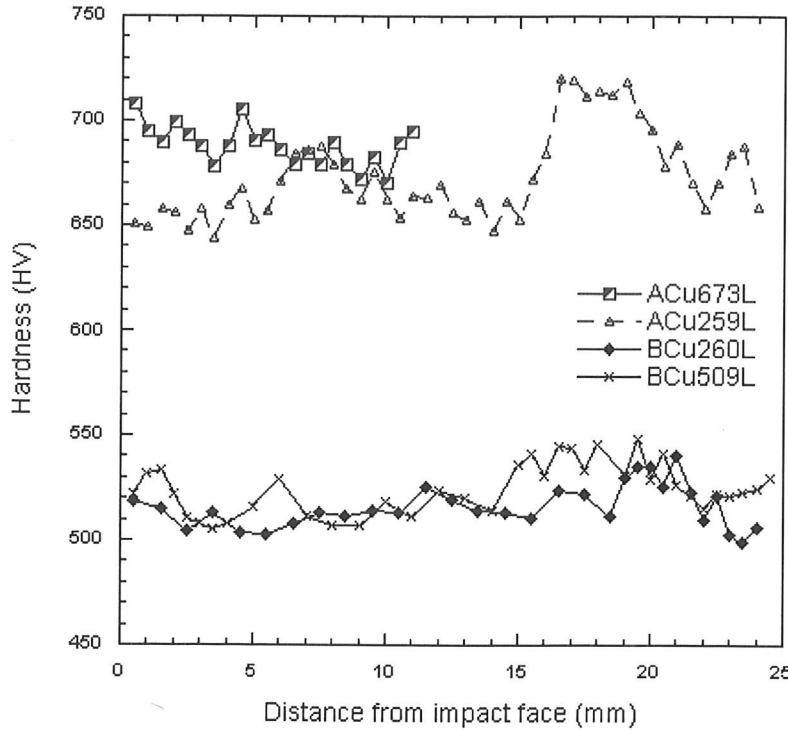


Figure 4.6.2 X-ray diffraction plot for lower temperature bainite post-impact by copper flyer at 843 m s<sup>-1</sup>. This plot is typical of all the plots recorded for upper bainite, both before and after impact.

around the position of the spall plane. The hardness near to the impact face is expected to increase as that material has been under shock for longer (Murr and Meyers 1983), however it would appear from this research that there is little or no effect.



**Figure 4.6.3** Examples of data from micro-hardness traverses of samples of recovered material. Note that a label beginning with A is an experiment carried out on the lower temperature bainite and B corresponds with the upper bainite. This is followed by Cu which indicates a copper impactor was used at the velocity (in  $m s^{-1}$ ) which is given by the 3 digits following. All samples were from 'lateral' experiments so all these short codes end with L.

The initial and post-impact hardnesses (average) that are given in figure 4.6.4, clearly show that the higher the maximum dynamic pressure seen by the sample the greater the micro-hardness. Together with the previous figure, this suggests that the pressure of the shock wave is much more significant than its duration in terms of the creation of dislocations.

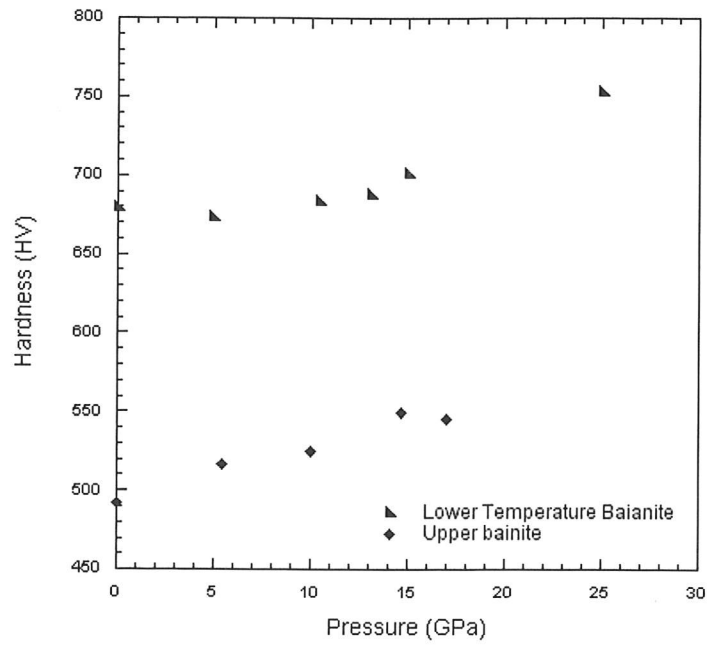


**Figure 4.6.4** Plot of average hardness value from traverse against the maximum dynamic pressure seen by sample.

## 4.7 Conclusions

Both lower temperature and upper bainites were found to have Hugoniot curves and shear strengths similar to that of mild steel. The HEL were found to be  $3.5 \pm 0.5$  GPa and  $2 \pm 0.5$  GPa respectively. Lower temperature bainite was found to have a phase transition at  $13 \pm 0.5$  GPa.

At longitudinal stresses greater than 13 GPa, it was found that the lateral gauges were unable to give stress-time histories for the whole of the impact. The addition of up to 175  $\mu\text{m}$  of mylar around the two gauges did not alleviate this problem. There was also concern that using such a large quantity of mylar might affect the stress level in the gauge. The effect of "padding" the gauge in this way has been quantified (Hammond et al. 2003) and is reported in chapter 7 of this dissertation.

The performance of armour is also related to the spall strength of the material. The spall strengths of both lower temperature bainite and upper bainite were measured. The spall strength of the lower bainite was found to be circa 2 GPa below the phase transition. Above this it fell significantly. The spall strength measurements for the upper bainite did not show any evidence of the phase transition occurring; its value remaining roughly constant at about 1.9 GPa throughout the stress range considered in this work.

In order to understand why the materials behaved as they did and possibly to predict material properties in the future, it is important to investigate the microstructural response to the different impact conditions. This could take the form of further microscopy, X-ray diffraction and hardness testing. Such research may help to establish why the phase transition was not observable in upper bainite and why the HELs, of the two materials are so different.

From the micro-hardness studies performed, it can be concluded that the effect of the pressure of the shock wave is significantly more than any effect of its duration. There is some indication that the dynamic fracture of the material at the spall plane introduces a significant number of dislocations into the material. There is inevitably

some effect of the fact that these samples were not soft recovered. There will have been effects from lateral release waves traveling through the material and also other unintentional impacts as the material comes to rest. In order to pursue hardness testing further as a route to understanding the material behaviour, future impact experiments incorporating soft recovery would be necessary.

As a result of this research, we can say that the lower temperature bainite showed evidence of the phase transition occurring, whereas the upper bainite did not. It may be that it was suppressed in the stress range considered in this paper, or simply that it was not observable. The reason for this unexplained behaviour is almost certainly to do with the microstructure; the main differences between the two forms of bainite are in grain size, carbide distribution and number.

## References

- Barker, L. M. (1975). "Alpha-phase Hugoniot of iron." J. Appl. Phys. **46**(6): 2544-2547.
- Barker, L. M. and R. E. Hollenbach (1974). "Shock wave study of the alpha-epsilon phase transition in iron." J. Appl. Phys. **45**(11): 4872-4887.
- Bhadeshia, H. K. D. H. (1999). "The bainite transformation: unresolved issues." Mat. Sci. & Eng. **A273-275**: 58-66.
- Bhadeshia, H. K. D. H. (2001). Bainite in steels, IOM Communications Ltd.
- Caballero, F. G., H. K. D. H. Bhadeshia, K. J. A. Mawella, D. G. Jones and P. Brown (2001a). "Design of novel high strength bainitic steels: Part 1." Mat. Sci. Tech. **17**: 512-516.
- Caballero, F. G., H. K. D. H. Bhadeshia, K. J. A. Mawella, D. G. Jones and P. Brown (2001b). "Design of novel high strength bainitic steels: Part 2." Mat. Sci. Tech. **17**: 517-522.
- Caballero, F. G., H. K. D. H. Bhadeshia, K. J. A. Mawella, D. G. Jones and P. Brown (2002). "Very strong low temperature bainite." Mat. Sci. & Tech. **18**: 279-284.
- Church, P. D., W. G. Proud, T. D. Andrews and B. Goldthorpe (2001). The spall strength measurement and modelling of AQ80 iron and copper systems. 12th APS Topical Group on Shock Compression of Condensed Matter, Atlanta, AIP.
- Duvall, G. E. and R. A. Graham (1977). Rev. Modern Phys. **49**: 523-579.
- Graham, R. A. (1992). Solids under high-pressure shock compression: Mechanics, physics and chemistry. New York, Springer Verlag.
- Hammond, R. I., P. D. Church, A. Grief, W. G. Proud and J. E. Field (2003). Dependence of measured lateral stress in thickness of protective "padding" around gauge. APS, Portland, Oregon.
- Honeycombe, R. W. K. and H. K. D. H. Bhadeshia (1995). Steels: Microstructure and Properties. London, Edward Arnold.
- Johnson, J. N., R. S. Hixson, D. L. Tonks and A. K. Zurek (1995). Rate-dependent spallation properties of tantalum. APS Topical Group on Shock Compression of Condensed Matter, Seattle, Washington, AIP.
- Meyers, M. A. (1979). "An estimate of the nucleation time in the martensitic transformation." Met. Trans. A **10A**: 1723-1727.

- Millett, J. C. F., N. K. Bourne and Z. Rosenberg (1995). Shear stress measurements in copper, iron and mild steel under shock loading conditions. APS Topical Group on Shock Compression of Condensed Matter, Seattle, Washington, AIP.
- Millett, J. C. F., N. K. Bourne and Z. Rosenberg (1997). An investigation of the alpha-epsilon phase transition in shock loaded EN3 mild steel. APS Topical Group on Shock Compression of Condensed Matter, AIP.
- Millett, J. C. F., R. Flaxman and N. K. Bourne (1996). The measurement of the Hugoniot of porous tungsten alloy, PCS, Cavendish Laboratory, Cambridge University.
- Murr, L. E. and M. A. Meyers (1983). Metallurgical effects of shock and pressure waves in metals. Explosive welding, forming and compaction. T. Z. Blazynski. Barking, Essex, England, Applied Science Publishers Ltd.: 83-122.
- Murray, N. H. (1996). The response of alumina based ceramics to high strain-rate loading. Cavendish Laboratory, University of Cambridge: 97.
- Veeser, L. R., G. T. Gray III, J. E. Vorthman, P. J. Rodriguez, R. S. Hixson and D. B. Hayes (1999). High pressure response of a high-purity iron. 11th APS Topical Group on Shock Compression of Condensed Matter, Snowbird, Utah, AIP.

## **Chapter 5**

### **Ballistic studies**

A wide-ranging study of the ballistic properties of the bainites was planned. However, only a few samples of a lower temperature bainite, similar to the one previously considered were available. The composition had been slightly modified, from the original lower temperature bainite, to reduce porosity. In this dissertation, this is referred to as 'new lower temperature bainite'.

In this chapter, the new lower temperature bainite was compared to both mild steel and RHA steel (refer to chapter 2). The experiments were carried out using the 50 mm bore light-gas-gun and high-speed images were recorded using the Ultramac FS-501 camera. The impactors used in all cases were flat-ended FNC tungsten rods of length to diameter ratio 10:1, diameter 5.55 mm.

Further experiments were carried out to investigate the depth of penetration of the projectile after passing through a front piece of new low temperature bainite, mild steel or RHA. It should be remembered that the penetration characteristics of a material are altered when the plate is constrained i.e. backed with another piece of material. The backing material used in all these experiments was RHA.

## 5.1 Impacts on free plates

All experiments were recorded using the Ultramac FS-501 high-speed camera. The images were side views of the impact.

### New low temperature bainite

Figure 5.1.1 gives a high-speed photograph sequence for an impact event between a tungsten alloy rod travelling at  $912 \text{ m s}^{-1}$  and a 9.6 mm thick plate of new low temperature bainite. The rear surface of the plate shows bulging  $6 \mu\text{s}$  after the impact. By this stage there are already ejecta travelling away from the front face of the bainite (towards the barrel). Later in the impact, the bulging material breaks away from the plate in the form of a plug. The effect of the impactor has been spread over an area of the target that is larger than the cross-section of the projectile itself. This is beneficial in terms of energy dissipation in armour steels. The projectile itself is shortened during the impact. Note there is an impact flash in frames 11 and 12, this makes it look as if the tungsten rod has disappeared.

The same set-up, but with a lower impact velocity,  $605 \text{ m s}^{-1}$ , was used in the experiment that is depicted in figure 5.1.2. The major point here is that the rod takes a much longer time to cause a bulge in the rear surface of the plate and also perforation is retarded. It is not until  $\sim 15 \mu\text{s}$  after the impact that bulging of the rear surface is observed. The ejecta from the front face are travelling at a greater angle to the path of the incoming projectile than in the higher velocity shot i.e. the debris are more spread out. It is hard to tell from this high-speed record if there is any dwell or shortening of the tungsten rod as the sabot does not come into the field of view until the last two frames.

Impact experiments were carried out on thinner, 4.1 mm thick, plates of this new low temperature bainite. Both the impact at  $609 \text{ m s}^{-1}$  and the one at  $410 \text{ m s}^{-1}$  seem to show the rod passing straight through the plate, refer to figures 5.1.3 and 5.1.4. In both of these cases, most of the ejected debris is again travelling towards the barrel, it seems to be spread over a wider range of angles than in previous shots. These debris

will be discussed later in this chapter. In the slower of these two experiments, there may be some bulging of the rear face of the target around 4 to 10  $\mu\text{s}$  after the impact, just prior to perforation.

Figures 5.1.5, and 5.1.6 are photographs of the debris collected post-impact for two separate experiments. The former, clearly shows a perforation, in the 4.12 mm thick new low temperature bainite, no larger than the rod's cross-sectional area. This indicates the initial damage was perforation by a plugging mechanism, the remaining fracture probably occurred due to post-impact flexure. Figure 5.1.6 shows the debris after impact on a thicker piece of the new lower temperature bainite. There is evidence of fracture occurring radially from the impact site. The fact that the central pieces were not recovered, indicates that they were almost certainly smaller.

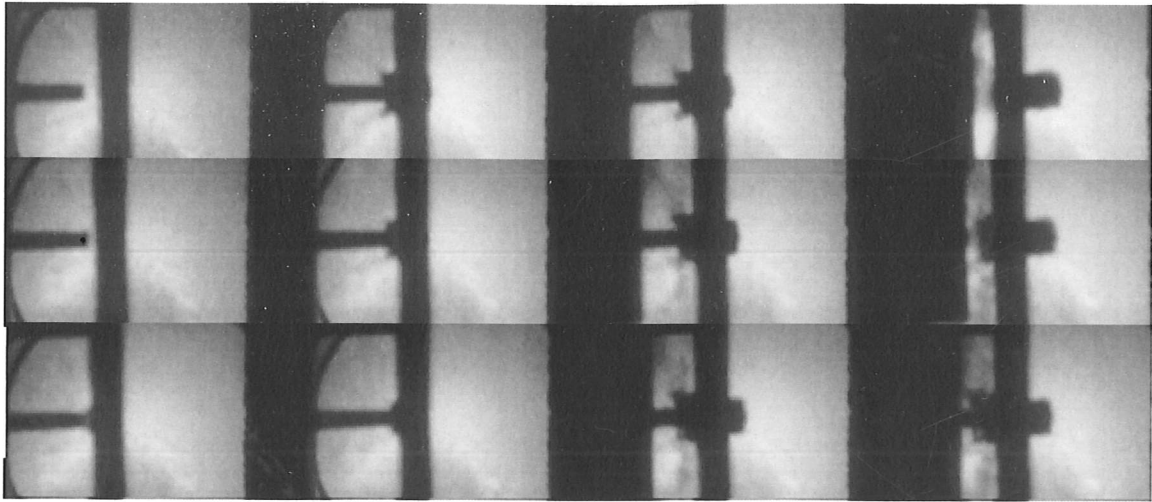


*Figure 5.1.1 Tungsten alloy rod at  $912 \text{ m s}^{-1}$  on 9.6 mm thick new low temperature bainite. Interframe time  $2 \mu\text{s}$ , exposure time  $1 \mu\text{s}$ .*

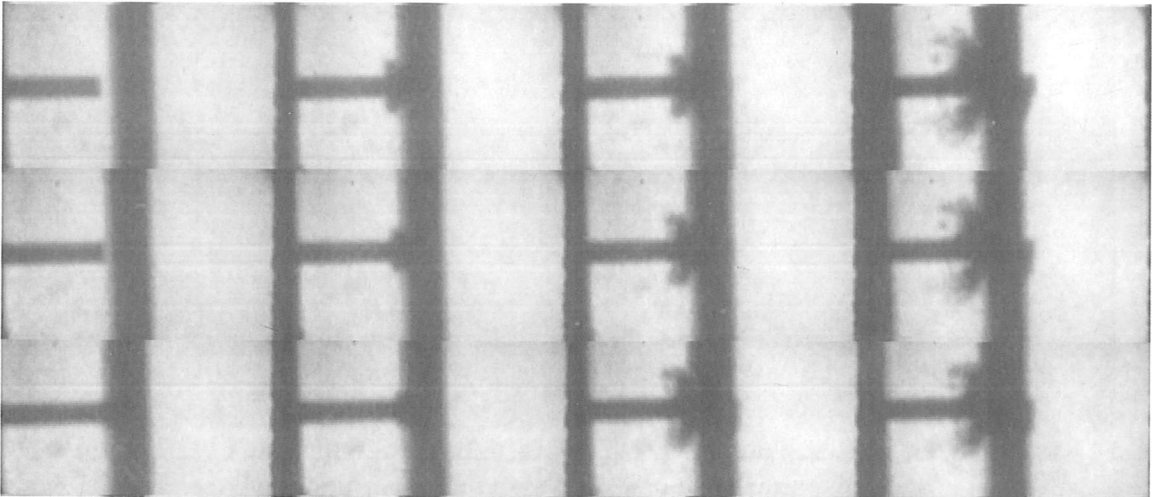


*Figure 5.1.2 Tungsten alloy rod at  $605 \text{ m s}^{-1}$  on 9.6 mm thick low temperature bainite. Interframe time  $2 \mu\text{s}$ , exposure time  $1 \mu\text{s}$ .*

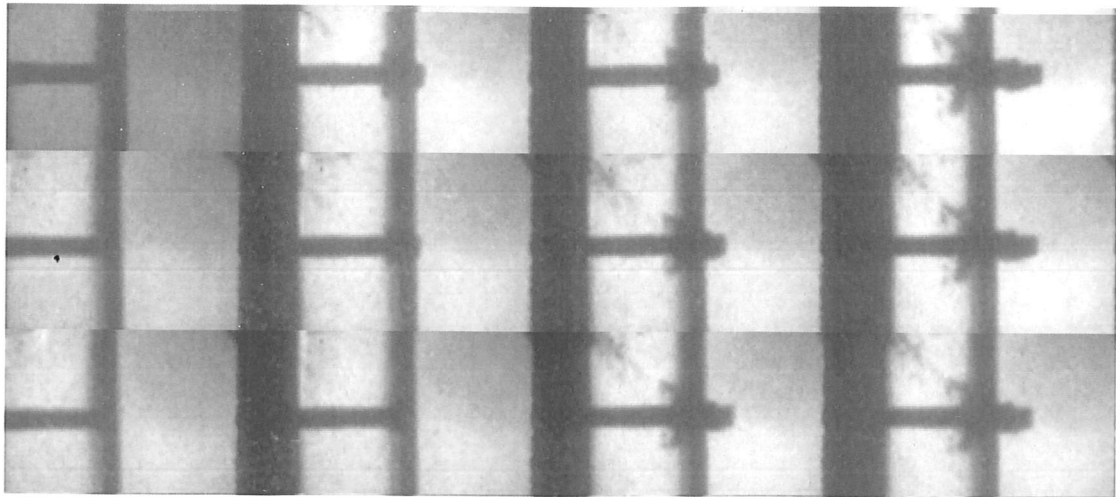


*Figure 5.1.3 Tungsten alloy rod at  $609 \text{ m s}^{-1}$  on 4.1 mm thick low temperature bainite. Interframe time  $2 \mu\text{s}$ , exposure time  $1 \mu\text{s}$ .*

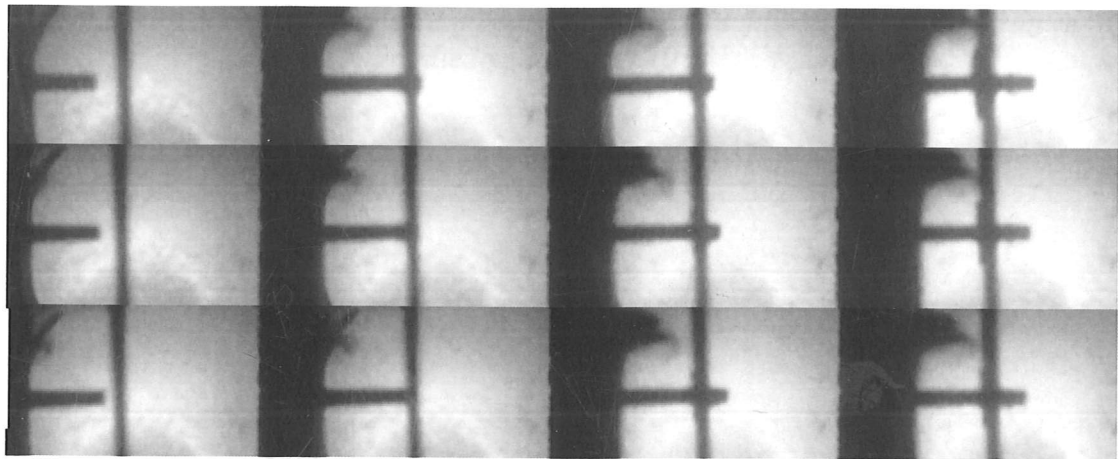


*Figure 5.1.4 Tungsten alloy rod at  $410 \text{ m s}^{-1}$  on 4.1 mm thick low temperature bainite. Interframe time  $4 \mu\text{s}$ , exposure time  $1 \mu\text{s}$ .*

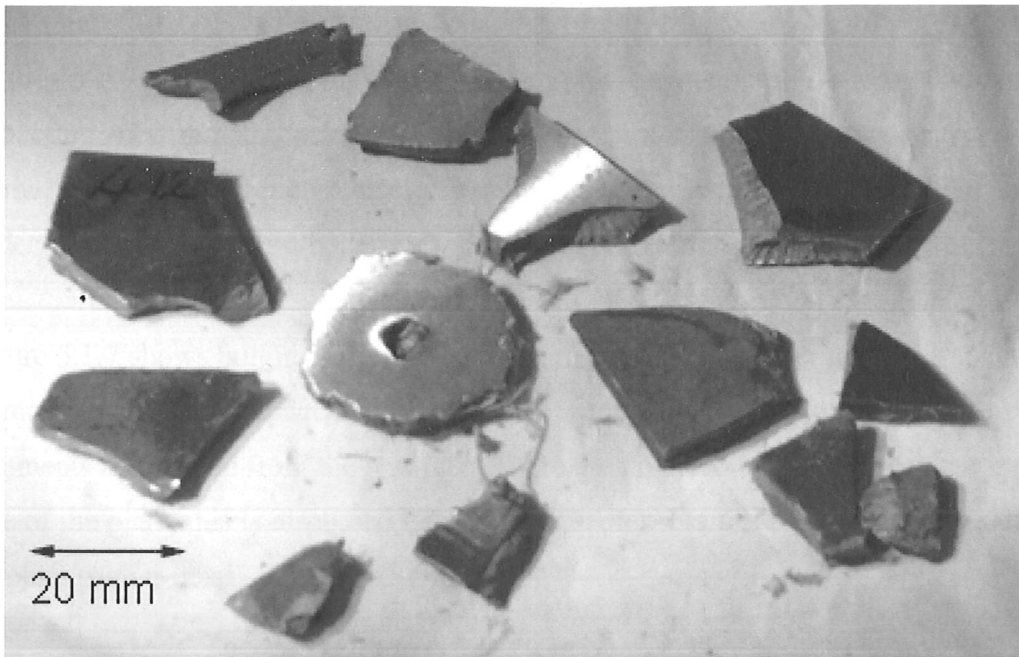


*Figure 5.1.5 Debris recovered post-impact, 4.12 mm thick new low temperature bainite impacted at  $410 \text{ m s}^{-1}$ .*

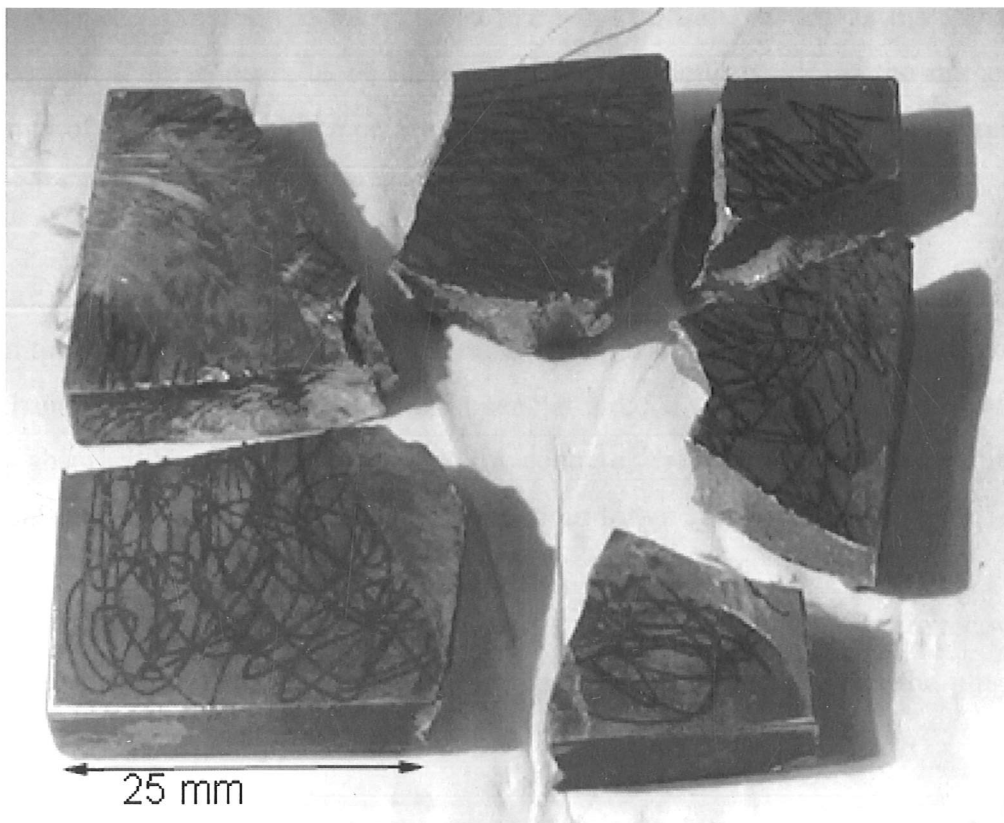


*Figure 5.1.6 Debris recovered post-impact, 9.6 mm thick new low temperature bainite impacted at  $605 \text{ m s}^{-1}$ .*

### Mild steel

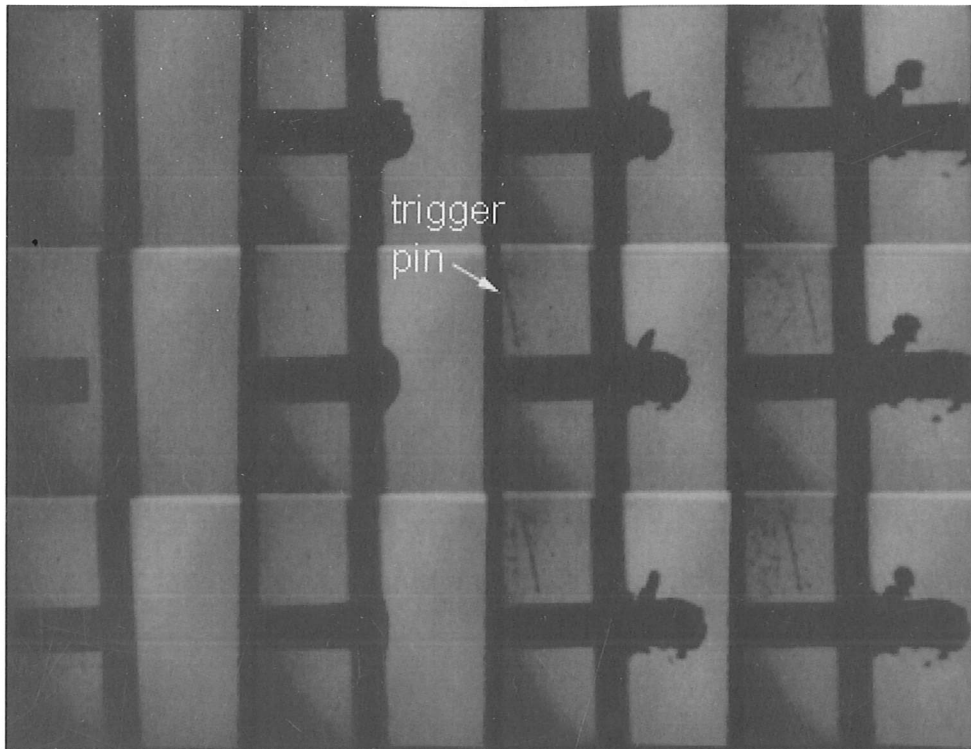
Figures 5.1.7 and 5.1.8 are high-speed photographic sequences of tungsten alloy rods impacting 4.00 mm thick mild steel at  $600 \text{ m s}^{-1}$  and  $400 \text{ m s}^{-1}$  respectively. The former is magnified which is useful for observing the local deformation. The latter, wider view image, gives a better view of any fragmentation and ejecta.

Figure 5.1.7 shows bulging after impact in frames 4 and 5; up to  $6 \mu\text{s}$  after impact. By frame 6,  $9 \mu\text{s}$  after impact, the plate has been perforated. A plug as well as other fragments are ejected from the rear face. There are no ejecta observed from the impact side of the plate, this is discussed later in this chapter. Frames 8 to 12 show one of the graphite trigger pins!

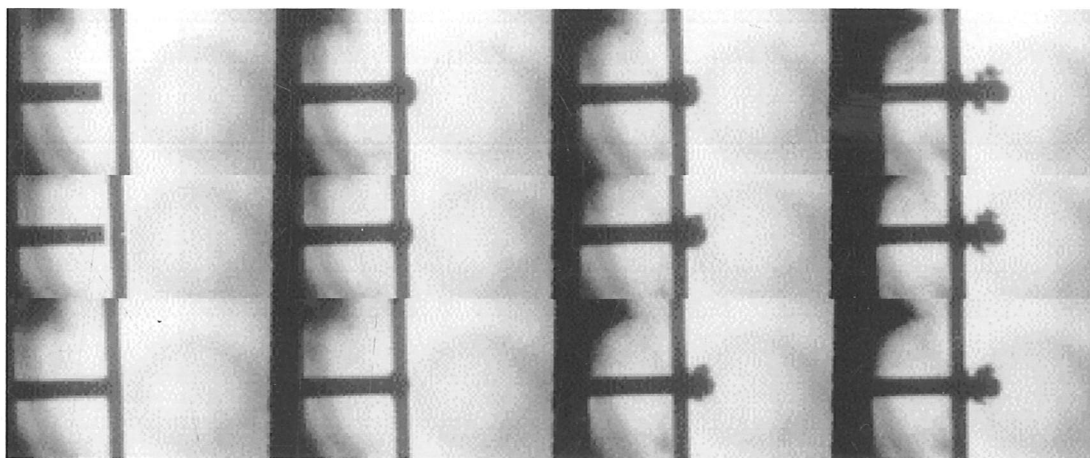
Figure 5.1.8 has longer interframe times and the rod has lower velocity. The bulging lasts for 3 frames but this is a similar length of time to that observed in figure 5.1.7. The plate can certainly be taken to be laterally 'infinite' as far as the impact is concerned, there appears to be little or no deformation outside of the immediate vicinity of the impact and the perforation is over before stress waves return from the supports. The deformation zone has a diameter of around two rod diameters.

Figure 5.1.9 shows the debris collected from an impact on mild steel (same impact conditions as for figure 5.1.5). The fracture has occurred by a much more ductile mechanism, fragments were also no longer flat indicating that some energy had also been absorbed by plastic deformation. The centre of the rear of the sample exhibits a typical spall failure: certainly not good behaviour for an armour material.

Typical recovered debris are shown in figure 5.1.10. The rod and plug were recovered intact, the plate itself was in several fragments. This is evidence that the plugging mechanism was indeed occurring.



**Figure 5.1.7** High-speed photographic sequence of tungsten rod impacting 4.0 mm thick mild steel plate at  $603 \text{ m s}^{-1}$ . Exposure time  $1 \mu\text{s}$ , interframe time  $2 \mu\text{s}$ .



**Figure 5.1.8** High-speed photographic sequence of tungsten rod impacting 4.0 mm thick mild steel plate at  $417 \text{ m s}^{-1}$ . Exposure time  $1 \mu\text{s}$ , interframe time  $4 \mu\text{s}$ .

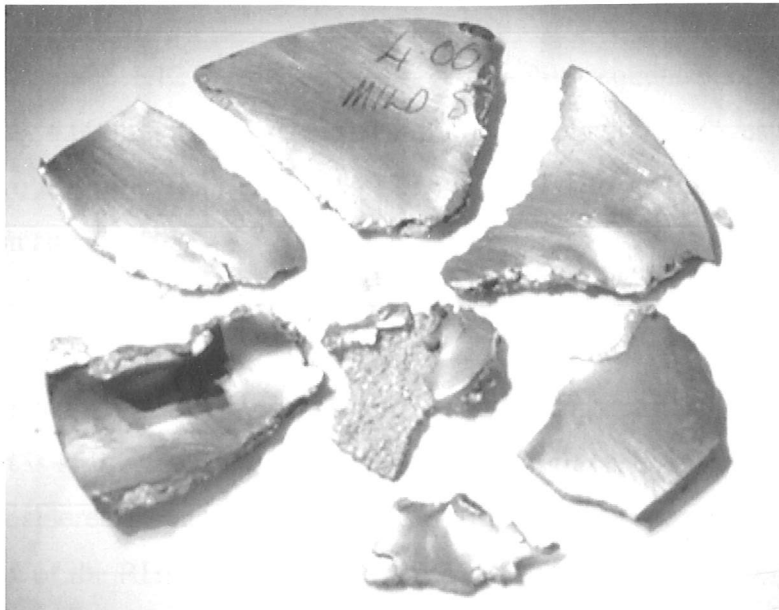


*Figure 5.1.9 Debris recovered post-impact, 4.0 mm thick mild steel impacted at  $410 \text{ m s}^{-1}$ .*

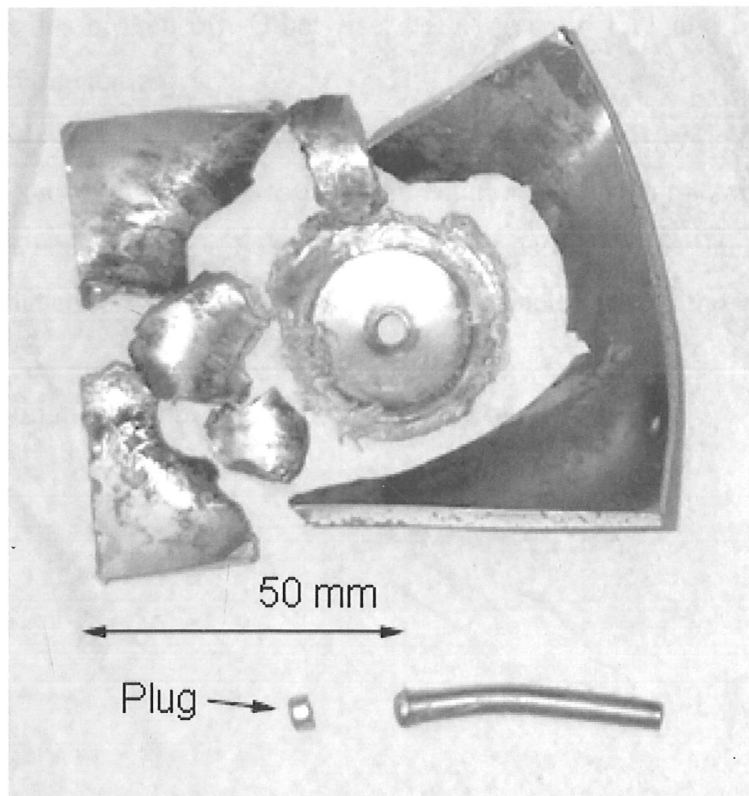


*Figure 5.1.10 Debris recovered post-impact, a 4.0 mm mild steel plate was impacted by a tungsten alloy rod with velocity  $600 \text{ m s}^{-1}$ . Note that a plug of the steel was recovered and the rod was intact.*

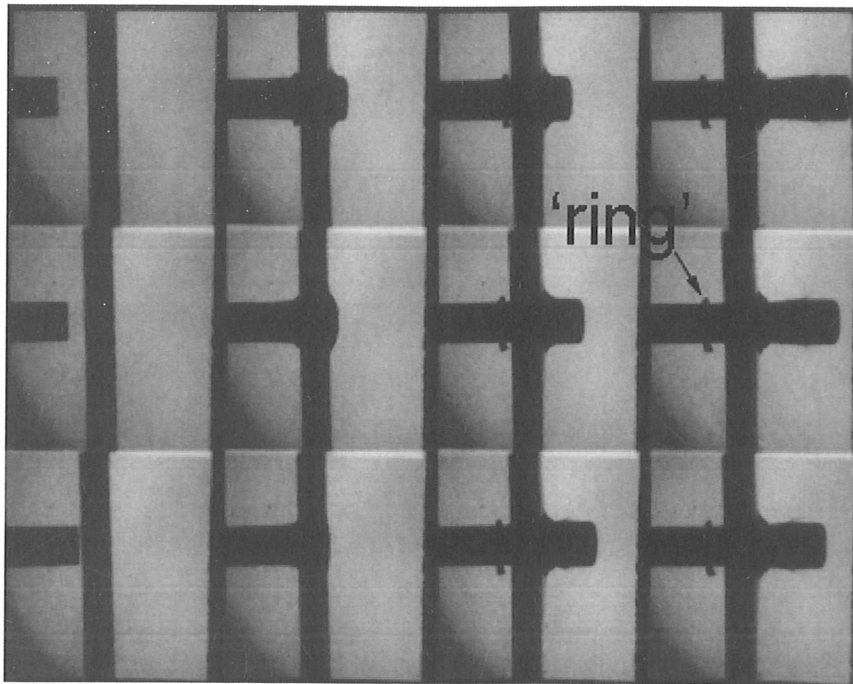
### **RHA steel**

Figures 5.1.11 and 5.1.12 are high-speed photographic sequences of tungsten alloy rods impacting 4.00 mm thick RHA steel at  $600 \text{ m s}^{-1}$  and  $400 \text{ m s}^{-1}$  respectively. The views use two magnifications, one for observing local deformation, the other to view fragmentation and ejecta.

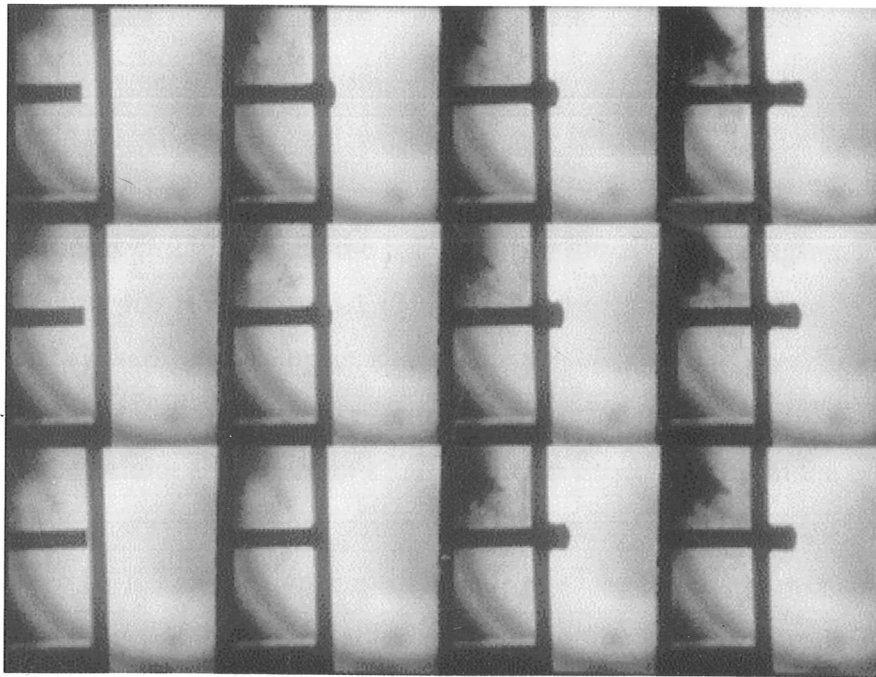
Bulging of the rear face of the plate is observed in frames 4 to 6 of figure 5.1.11, beyond which there is evidence that of permanent deformation around the impact area which in fact is still present in the recovered sample, figure 5.1.13. Unlike the other materials considered in this chapter, the RHA steel samples were recovered mostly intact. A plug of the RHA steel is ejected ahead of the rod, most evident in frames 9 to 12. There is one 'ring' of debris ejected back along the length of the incoming rod, frames 6 to 12. This could be a 'mushroom' of material from the front of the projectile that has broken off. Otherwise, both figures 5.1.11 and 5.1.12 show no evidence of fragmentation.

Figure 5.1.13 shows that there was no fragmentation of the sample after impact, the only damage sustained was a hole, same diameter as the projectile, and the plastic deformation that covers occurs only a further rod diameter around the impact zone.

Clearly the main mechanism of failure is plugging in all cases.



*Figure 5.1.11 High-speed photographic sequence of tungsten rod impacting 4.0 mm thick RHA steel plate at  $588 \text{ m s}^{-1}$ . Exposure time  $1 \mu\text{s}$ , interframe time  $2 \mu\text{s}$ .*



*Figure 5.1.12 High-speed photographic sequence of tungsten rod impacting 4.0 mm thick RHA steel plate at  $393 \text{ m s}^{-1}$ . Exposure time  $1 \mu\text{s}$ , interframe time  $4 \mu\text{s}$ .*

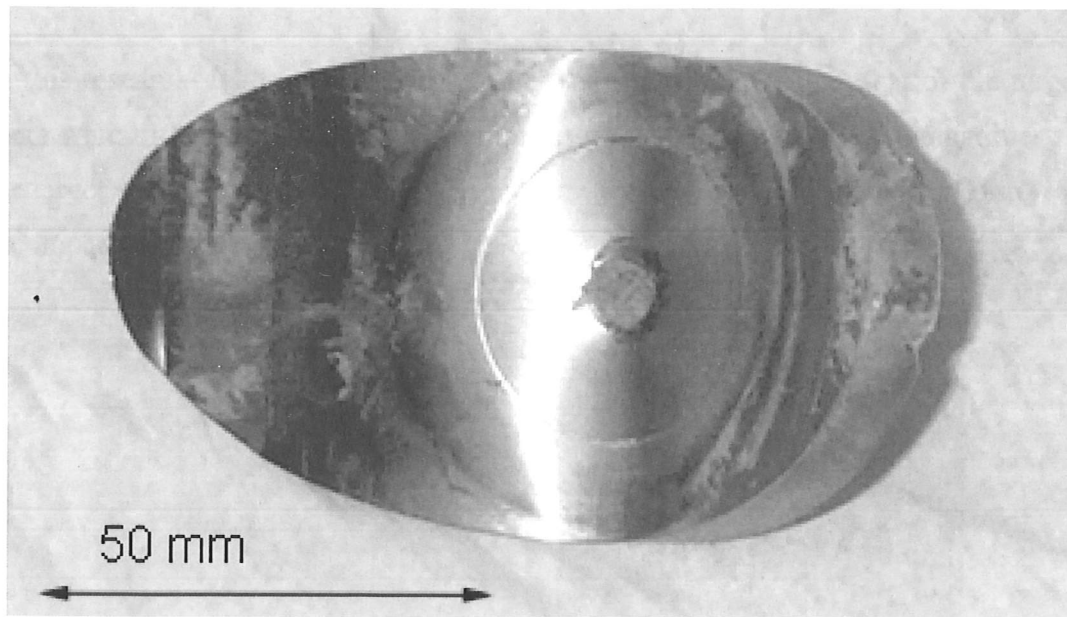


*Figure 5.1.12 Recovered debris after impact on 4 mm thick RHA steel by tungsten alloy rod  $393 \text{ m s}^{-1}$ .*

### **Ejected debris**

As mentioned in section 1.3 of this dissertation, the relative hardnesses of the projectile and target material are very important (Field 1988). The facing of the targets considered in this chapter vary from RHA steel at 150 HV, the mild steel having a hardness of 250 HV and the bainite being 700 HV. The tungsten alloy had a hardness of circa 400 HV. Figure 5.1.13 shows frames from each of four experiments. Debris were ejected on the impact side of the target in two of these. One was an impact on the new low temperature bainite at  $605 \text{ m s}^{-1}$ , figure 5.1.13 (a). All the other impacts on the bainite above  $600 \text{ m s}^{-1}$  also showed similar ejecta. In the other frame showing debris traveling away from the impact face, there were less ejecta (figure 5.1.13 (b)). This was an impact at  $410 \text{ m s}^{-1}$  on the new lower temperature bainite. This debris fan was a larger angle from the incoming rod. This is an interesting result as the main factor in determining the amount of ejected debris should have been hardness (Field 1988). Clearly there are other factors.

Figures 5.1.13 (c) and (d) show frames from impacts on mild steel and RHA steel respectively. Neither of them shows ejected debris fanning out from the impact zone. The latter does however exhibit the 'ring' of debris discussed earlier in this chapter.

In this research, if the hardness of the impactor was greater than that of the target, there were little or no ejecta from the impact side of the plate. When the hardness of the target was greater than that of the impactor, there were debris ejected in a fan from the impact surface of the plate.

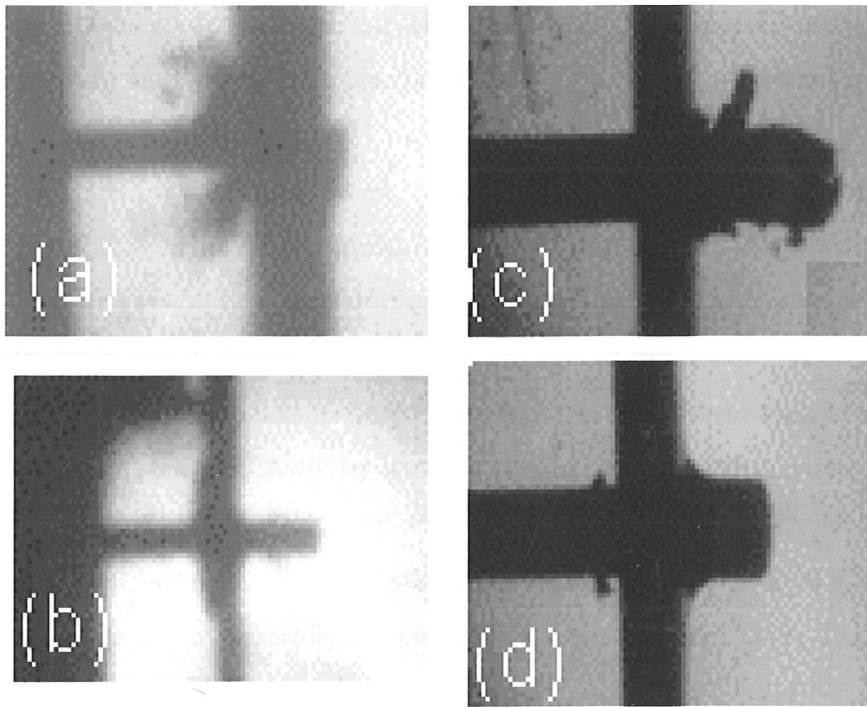


**Figure 5.1.13** Frames from each of four experiments (note for scale each rod has diameter 5.55 mm, i.e. each frame has a different scale):

- (a) Frame 11 of figure 5.1.2. Impact at  $605 \text{ m s}^{-1}$  on 9.6 mm thick NLTB.
- (b) Frame 12 of figure 5.1.4. Impact at  $410 \text{ m s}^{-1}$  on 4.1 mm NLTB.
- (c) Frame 9 of figure 5.1.7. Impact at  $603 \text{ m s}^{-1}$  on 4.0 mm mild steel.
- (d) Frame 8 of figure 5.1.11. Impact at  $588 \text{ m s}^{-1}$  on 4.0 mm RHA steel.

## 5.2 Depth of penetration studies

A series of experiments was carried out using a backing of 50 mm of RHA steel. This ensured that perforation was not possible in any of the experiments. By facing the RHA steel with one of the three materials that are being considered in this chapter, their penetrative properties were compared. One experiment was carried out without a facing plate. It was compared with the RHA steel facing on the RHA steel backing in order to ascertain whether the interface has any effect on the penetration depth.

The samples were then examined by X-rays to determine both the profile of the tungsten and the depth of penetration. A 200 kV Pantek X-ray head was used with Kodak D7 film. The depth of penetration was determined for all 8 samples. Four of the samples were also X-rayed looking down the axis of impact in order to check that the tungsten had remained symmetric during the impact. The resolution of each X-ray image is 0.4 mm. This was found by use of a range of diameters of wires in the field of view and determining the diameter of the smallest wire resolvable. Measurements of depth of penetration were taken directly from the film and accurate to  $\pm 1$  mm. This error originates from the difficulty in determining exactly where the front edge of the sample is in the image.

### Results and discussion

Figure 5.2.1 shows a typical sample after impact. In most cases the facing plate was no longer attached to the sample, in this case there was no facing plate. The impact velocity was  $605 \text{ m s}^{-1}$ . The rod has penetrated the block normally and come to rest without the rear section of the rod either penetrating or breaking off. There is a large amount of plastic deformation in the RHA block in all samples.

The depth of penetration data are included in table 5.1 and are represented graphically in figure 5.2.2. The total depth of penetration varies between 21.5 mm and 23 mm for the higher velocity experiments. Given the experimental error is  $\pm 1$  mm, these values are not significantly different. This would suggest that the density of the material is

probably the most important factor as discussed in section 1.3 of this dissertation and also in (Tate 1967).

At the lower velocity considered, there is more variation. The experiments carried out with RHA plate with backing and backing only gave very similar total depth of penetration. This is important as it infers that the interface in the material between the plate and backing had little or no effect on the penetration. The sample faced with mild steel suffered 8.5 mm total depth of penetration which is not particularly different from the experiments carried out on RHA only. However, the experiment carried out on the new low temperature bainite faced sample exhibited 11.5 mm total depth of penetration, this is significantly more than the other materials.

A radiograph was also taken looking along the axis of the rod, it showed that the areas of tungsten were almost circular. This shows that the deformation was isotropic in the tungsten and steel. No radiographs are shown in this chapter as their reproduction is poor. The originals, however, were good enough to make the required measurements.

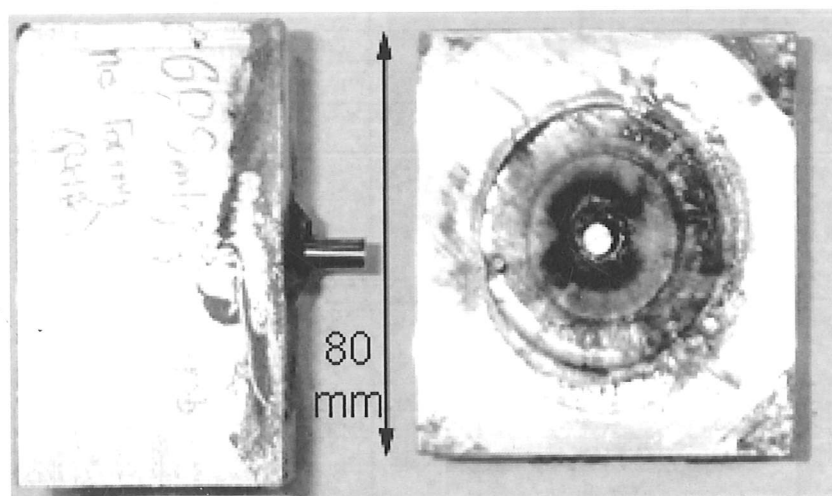


*Figure 5.2.1 Two views of sample post-impact. There was no facing plate in this experiment, the impact velocity was  $605 \text{ m s}^{-1}$ .*

Velocity (m s <sup>-1</sup> )	Facing material	Thickness of facing (mm)	Penetration into RHA backing (mm)	Total depth of penetration (mm)
605	-	-	7	7
605	Mild steel	4.0	4.5	8.5
605	RHA steel	4.0	2.5	6.5
605	NLTB*	4.0	7.5	11.5
894	Mild steel	4.0	17.5	21.5
894	RHA steel	4.0	18	22
895	NLTB*	4.0	18.5	22.5
900	NLTB*	8.0	15	23

*Table 5.1* Depth of penetration data, NLTB\* is new lower temperature bainite.

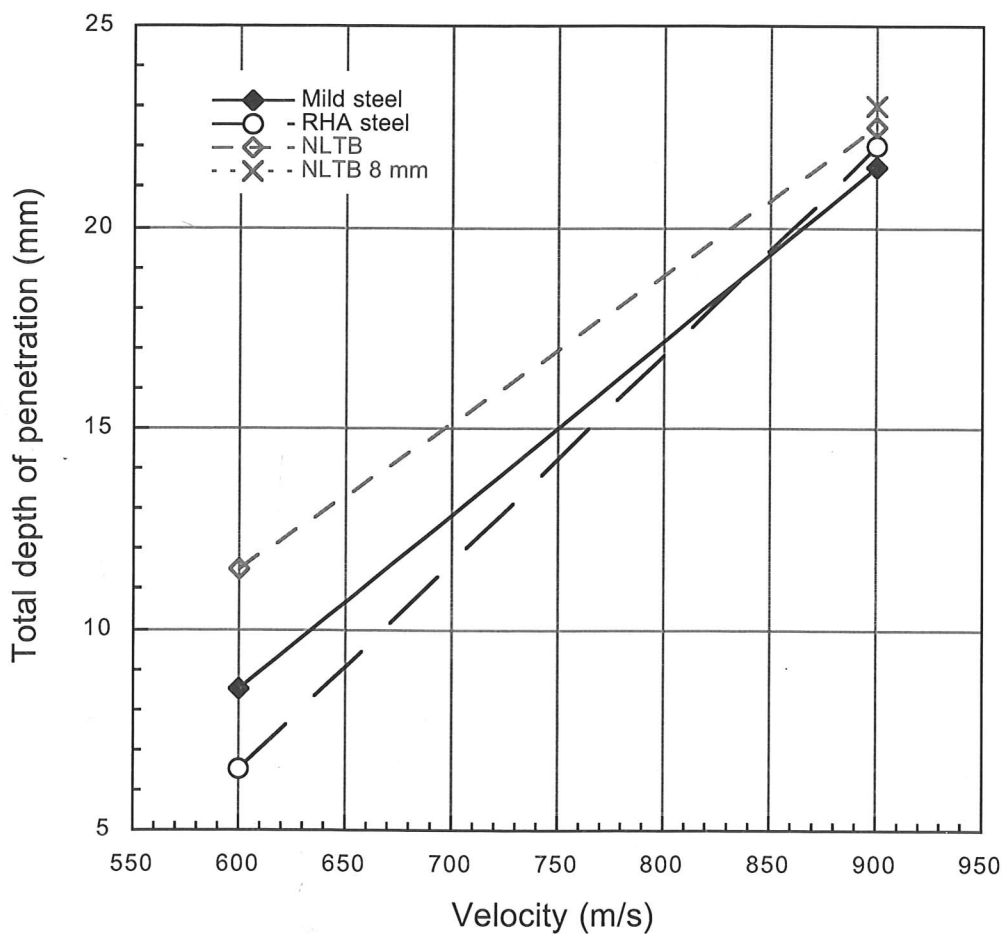


*Figure 5.2.2* Graphical representation of data from table 5.1.

### 5.3 Conclusions

The new low temperature bainite exhibited some characteristics of a good armour in some of the unsupported plate experiments, a plugging failure mechanism occurred however this was accompanied by extensive fragmentation with little plastic deformation.

The mild steel is certainly not a good armour steel, as some of the samples showed spalling which is extremely dangerous in armour applications. Some of the mild steel samples did fail by plugging at the higher velocities studied but in all experiments a large amount of fragmentation, both during the experiment i.e. spall and debris clouds and post-impact, occurred in the sample.

The RHA steel, on the other hand, failed by the plugging mechanism every time with no other fragmentation and some plastic deformation.

The depth of penetration work showed that at impact velocities of circa  $605 \text{ m s}^{-1}$ , the new low temperature bainite performed less well than either RHA steel or mild steel. However, at the higher velocity considered,  $900 \text{ m s}^{-1}$ , the three steels all appear to have shown similar ballistic behaviour.

It is not clear from this research whether the bainitic steel is an improvement on the RHA steel, further studies accompanied by modelling need to be carried out. However, both RHA steel and the new low temperature bainite were shown to be better armour material than mild steel.

It may be that at full ballistic velocities of  $1.8 \text{ km s}^{-1}$  the bainite shows a marked advantage. However, given the samples available, such trials are beyond the scope of this thesis.

## References

- Field, J.E. (1988). Final Technical Report: Investigation of the impact performance of various glass and ceramic systems, United States Army European Research Office, London, England. Contract number DAJ45-85-C-0021.
- Tate, A. (1967). "A theory for the deceleration of long rods after impact." J. Mech. Phys. Solids **15**: 387-399.

## Chapter 6

### Taylor impact of tungsten alloys

Tungsten alloys are under consideration as an environmentally friendly penetrator material. Much of the literature on ballistic performance of alloys is either classified or incomplete. There is however, still much information in the open literature (Furnish et al. 1995; Chang and Choi 1997; Satapathy et al. 1999; Kennedy and Murr 2001; Pappu et al. 2001). Two tungsten alloys were considered in detail; one that exhibited brittle fracture, the other more ductility. Refer to chapter 2 for a more complete description of these sintered alloys.

Taylor tests also provide a good validation method being both high strain and high strain rate. For a full discussion of the ideas behind both classic and symmetric Taylor tests, see chapter 1.

Tungsten based alloys are often used as penetrators due to their high density and strength. By addition of other elements, ductility can be improved at the expense of strength and alloys with around 91 % tungsten have been found to be a good compromise (Satapathy et al. 1999).

The two materials investigated in this study were commercial alloys containing 92.5 wt% tungsten with the balance being Ni, Fe and Co. One material was sintered and heat treated (SAC) and the other material was sintered, heat treated and cold worked (FNC). Both were supplied by QinetiQ, Fort Halstead. The rods were 55 mm in length and 5.5 mm in diameter. The physical properties of the two materials are given in chapter 2.

## 6.1 Experimental

Classic and symmetric Taylor tests were carried out on sintered tungsten alloys in order to determine the failure modes, deformation profiles and strain histories during impact. Impact velocities of  $200 \text{ m s}^{-1}$  were used in classic Taylor experiments and  $300 - 370 \text{ m s}^{-1}$  in the symmetric Taylor experiments.

In a second series of experiments angled faced rods were used in the 'symmetric' configuration to reduce the effect of misalignment. PMMA rods of identical aspect ratios were also studied. These were photographed through crossed polarisers in order to observe the propagation of the stress waves in relation to the fracture in the rods.

### (a) Classic Taylor tests

Classic Taylor experiments were carried out using a small single-stage light gas gun with a 60 kg steel block as the 'semi-infinite, rigid' body. This was faced with a SAC plate for shots using FNC and SAC rods. A schematic of the set-up is shown in figure 3.8.1 of chapter 3. Prior to firing the impact chamber and barrel are evacuated to 100 mbar. The firing vessel is then filled with helium to the required pressure for the shot, and when the gun is fired fast-acting valves open and the projectile is accelerated down the barrel.

The velocity of the projectile was measured by use of a velocitometer. This consisted of two low power laser diodes, the output of which could be fed into either a specially-constructed timer or into an oscilloscope. As it emerged from the barrel, the projectile intercepted these light beams, which were a known distance apart. The velocity was then calculated to an accuracy of  $\pm 1 \text{ m s}^{-1}$  using a counter timer.

The output of the timer was sent to a delay generator (Hadland) that triggered the flash unit, a Bowen Monolight 400, and camera, Ultramac FS-501 High-Speed Image Converter Camera, at the appropriate times. In order to ensure that the light output was sufficient during all the exposure time, the flash was triggered  $100 \mu\text{s}$  before the

camera. Images were recorded onto Polaroid 667 film and then digitised using a 600 dpi flatbed optical scanner.

After impact, the final profile of the rods was recorded and optical microstructural studies were undertaken.

(b) Symmetric Taylor tests with normal impact faces

Symmetric rod impact tests were carried out using the 50 mm bore light gas gun at Cambridge (Bourne et al. 1995). The target rod was instrumented with strain gauges on diametrically opposite sides (top and bottom of rod) 15 mm from the impact face. The rod was suspended in front of the barrel and aligned using both the Ultramac FS-501 High-Speed Image Converter Camera and a laser alignment system. With the rod aligned accurately, the gas gun chamber was sealed, the sabot placed in the breech and the interior of the gun evacuated to 1 mbar pressure. The upper edge of the plate had been ground to give a flat surface so that upon leaving the barrel this would short a series of velocity pins. The pin output was used to trigger a delay generator connected to the diagnostics. It should be noted that the sabot is still half to two thirds within the barrel upon impact. This allows precision alignment on impact to  $< 1$  mrad, which would not be achieved if the sabot was in free flight.

The rods were mounted in a frame made from steel sections welded to a 6.3 mm thick rectangular steel base, forming an upright in each corner. The uprights were made of square section pieces with rotating horizontal rods mounted at the upper and lower end of each upright. This frame was fixed to the base of the impact chamber of the single-stage light gas gun.

High-speed photographic sequences were taken of the impact events using an Ultramac FS501 image converter camera in conjunction with a Bowen flash. Images were recorded onto Polaroid 667 film.

(c) Symmetric Taylor tests with angled impact faces

The impact faces of some of the rods of the FNC tungsten alloy were ground to have impact faces  $45^\circ$  or  $30^\circ$  to the axis of the rod. 'Symmetric' tests were carried out at circa  $300 \text{ m s}^{-1}$ , using the small gas-gun in conjunction with a square-section barrel which eliminated rotation of the impactor prior to the impact. All experiments were recorded using the Ultramac FS-501 high-speed camera; some experiments also used strain gauges as a diagnostic tool. These were positioned in pairs, diametrically opposite one another on the target rod. There were 3 pairs at  $15 \text{ mm}$  intervals from the tip of the impact face of the rod as shown in figure 6.1.1.

In order to facilitate observation of stress waves, two experiments were carried out, using a similar geometry, with PMMA rods. These had a diameter of  $7.0 \text{ mm}$  and length  $70.0 \text{ mm}$ . Each experiment was viewed through crossed polarisers. The best method used to observe the stress waves in this research was through full-extinction crossed polarisers that were placed inside the impact chamber so that the residual strain in the chamber windows did not affect the imaging.

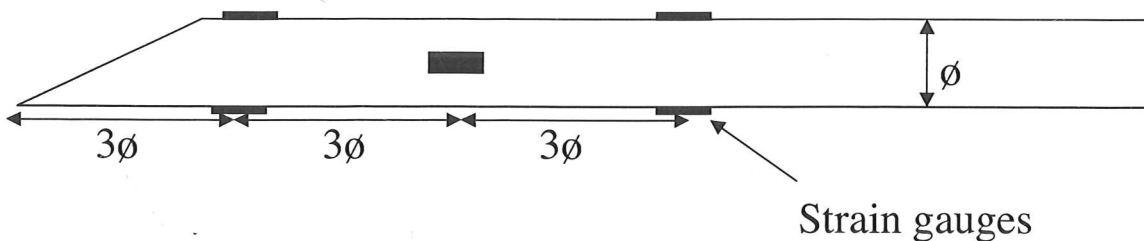


*Figure 6.1.1 Schematic diagram of positions of strain gauges on target rod.*

## 6.2 Results and Discussion

### (a) Classic Taylor

High-speed records of classic Taylor experiments, on both FNC and SAC tungsten alloys were made and a typical photographic sequence is shown in figure 6.2.1. The event was photographed through a dove prism which has rotated the image through  $90^\circ$ . In the real event, the rod moves horizontally. For both alloys, a characteristic mushroom shape was clearly visible. At this impact velocity, there was little fragmentation of the rods, which was mainly limited to chipping of part of the mushroom for the FNC samples.

The deformation profiles of each type of rod were measured after a classic Taylor experiment, figure 6.2.2. The SAC underwent more deformation over the length considered. The FNC rod deviated from its original diameter only in the 15 mm nearest to the impact face. Clearly, FNC was found to be more brittle than SAC in the classic Taylor set-up.

Optical microscopy made post-impact showed similar deformation mechanisms for both alloys. Tungsten grains were found to be deformed but still intact with the greatest level of deformation being at the impact face itself (figure 6.2.3). Any cracking observed was inter-granular (figure 6.2.4).

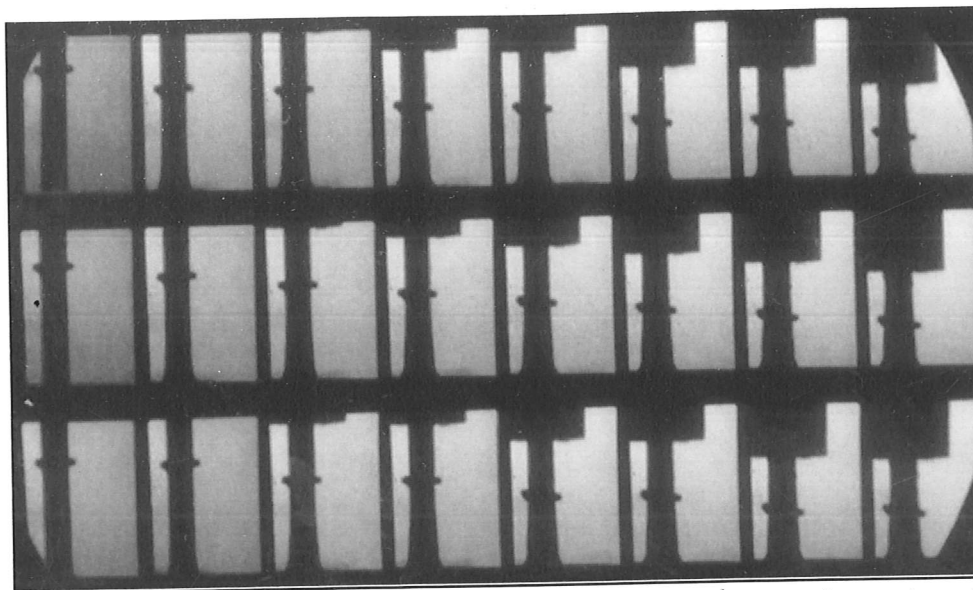


**Figure 6.2.1** SAC classic Taylor impact, velocity  $208 \text{ m s}^{-1}$ . Inter-frame time  $4 \mu\text{s}$ , exposure  $500 \text{ ns}$ . Note the rigid, target is horizontal at the bottom of each frame. A fiducial marker has been attached  $25 \text{ mm}$  from the impact end of the rod. A dove prism has been used to rotate each image by  $90^\circ$ . Refer to figure 3.6.1 for frame ordering.

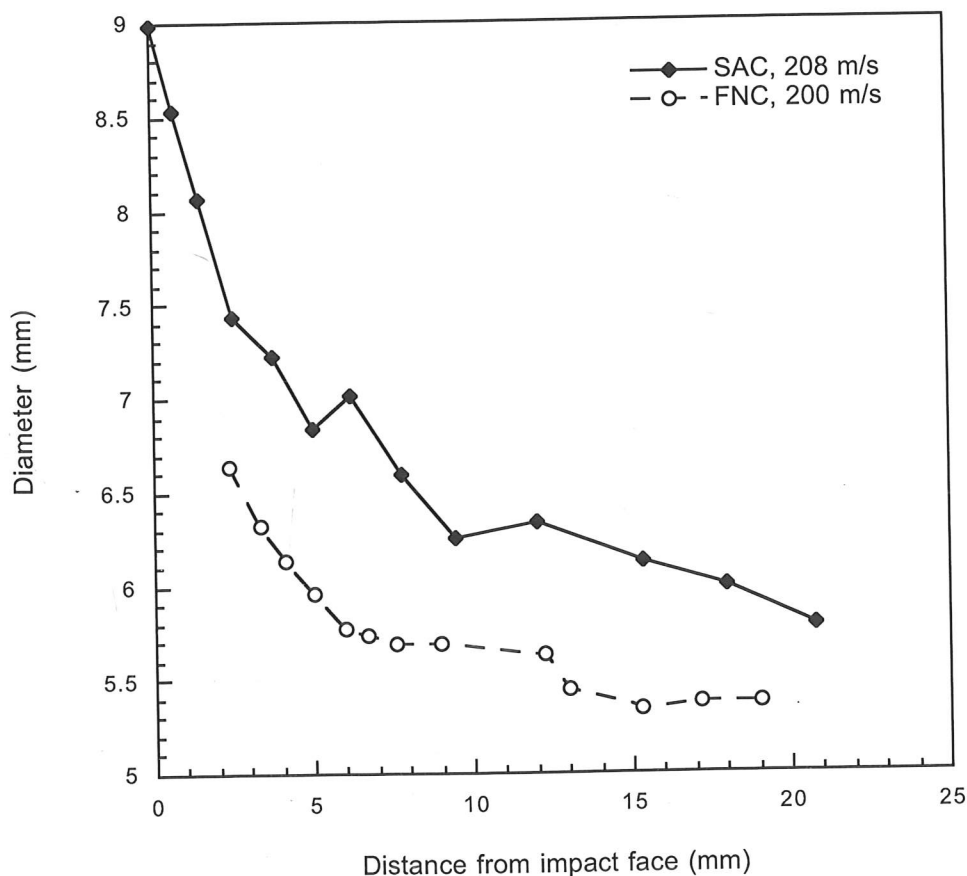


**Figure 6.2.2** Deformation profiles for both FNC and SAC after classic Taylor impact. Note part of the FNC rod's impact face was chipped off so there are no measurements for the first  $2 \text{ mm}$  from the impact face.

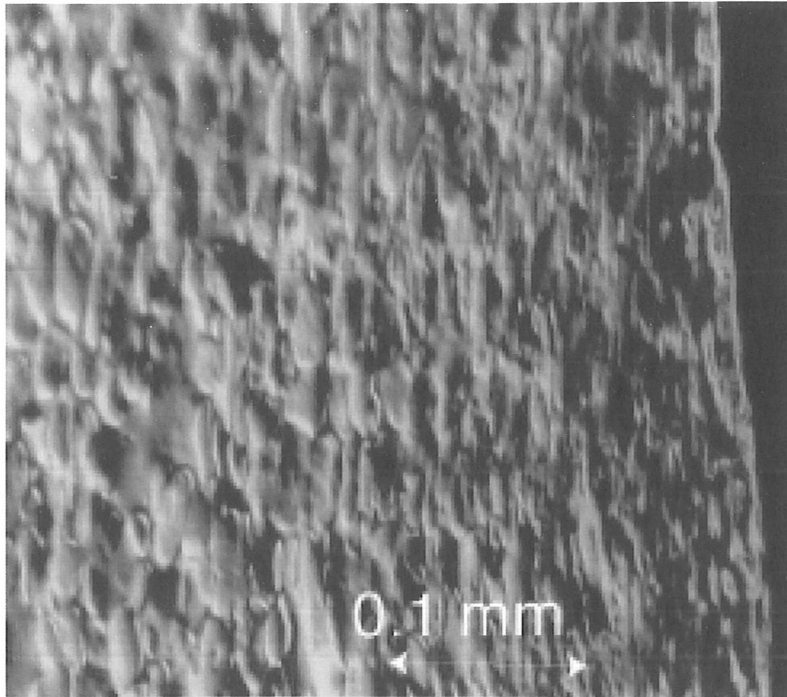


*Figure 6.2.3 Deformed grains at the impact face (right hand side of figure) in FNC rod post Classic Taylor impact at  $200 \text{ m s}^{-1}$ .*

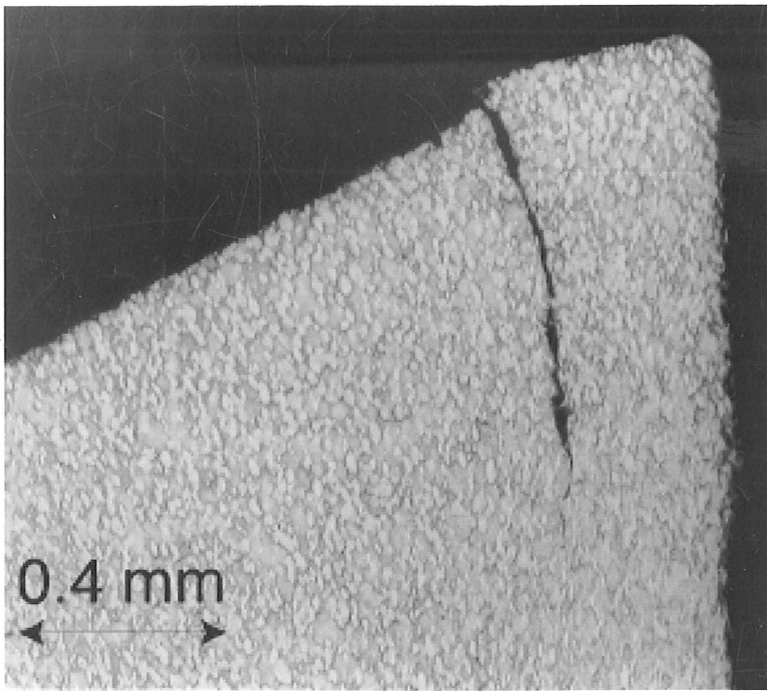


*Figure 6.2.4 Inter-granular crack near impact face (right hand side of figure) in SAC rod post Classic Taylor impact at  $208 \text{ m s}^{-1}$ .*

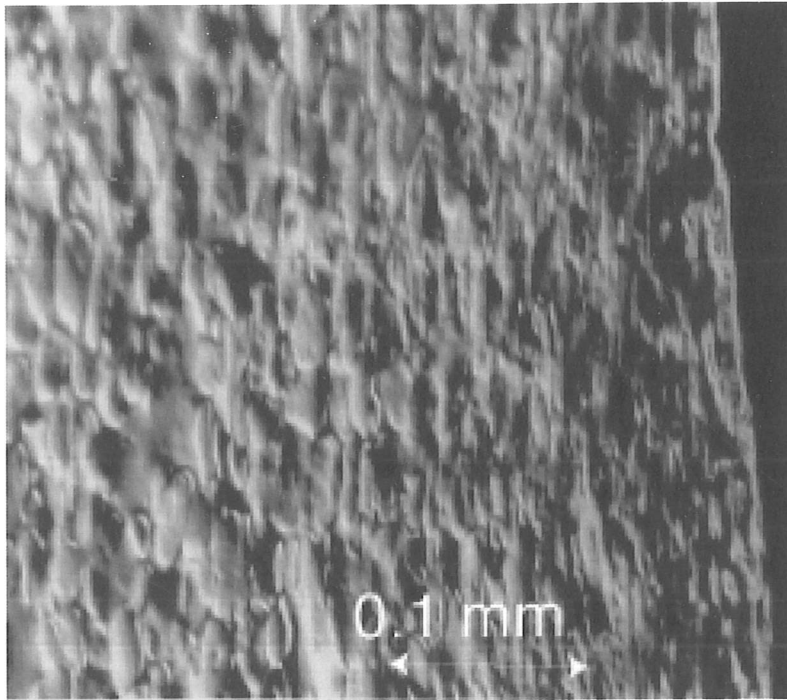


*Figure 6.2.3 Deformed grains at the impact face (right hand side of figure) in FNC rod post Classic Taylor impact at  $200 \text{ m s}^{-1}$ .*

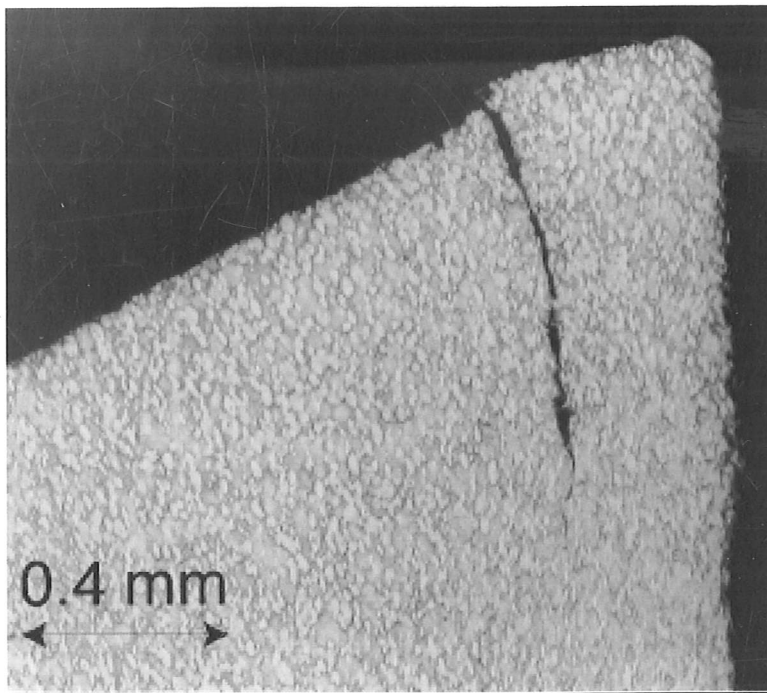


*Figure 6.2.4 Inter-granular crack near impact face (right hand side of figure) in SAC rod post Classic Taylor impact at  $208 \text{ m s}^{-1}$ .*

### (b) Symmetric Taylor tests with normal impact faces

Five instrumented symmetric Taylor impact tests were carried out on FNC rods, four near  $300 \text{ m s}^{-1}$  and one at  $370 \text{ m s}^{-1}$ . In addition, one shot was carried out using rods whose faces had been machined to  $45^\circ$ , in order that the direction of bend of the rods during the impact was predetermined. Longitudinal strain records, from only two of these experiments, are displayed in figure 6.2.5. For all experiments, traces exhibit an initial compression, which is consistent with the elastic precursor. After this, pairs of traces tend to diverge, which is indicative of rod bending, this is most evident for shot 020507b in which the rods had angled faces.

Four instrumented symmetric Taylor impact tests were carried out on SAC rods, three at  $300 \text{ m s}^{-1}$  and one at  $370 \text{ m s}^{-1}$ . One of the strain gauges failed; a selection of the seven remaining strain histories are displayed in figure 6.2.6. Again all traces exhibit an initial compression, relating to the elastic precursor after which pairs of traces tend to diverge again, indicative of bending of the rod.

All impacts were monitored by high-speed photography and an example of a sequence is given in figures 6.2.7. This is a well-aligned symmetric impact, velocity  $302 \text{ m s}^{-1}$ , of FNC rods. From these records, the alignment of each shot can be measured and bending of rods and any debris ejected can be observed. The measured offsets were compared with the onset of bending and values of strain obtained; refer to table 6.1.

It was found that the values of strain are not the same for nominally identical impacts. One reason for this is that the strain gauges were not necessarily in the same plane as the bending. It could also be due to the scatter in the strength of the sintered material leading to the position of fracture being unpredictable.

High-speed photography showed that bending tended to occur in the vertical plane, so gauges were placed accordingly on the uppermost and lowest side of the rod. The FNC strain traces show maximum strains of 3 % and minimum of -5 %. The traces are relatively noisy, and this is thought to be due to the very brittle nature of the fracture process in this material. The SAC traces show extremes of almost 5 % and

-7.5 %. SAC rods tended to exhibit greater bending before fracture, although when failure did occur it was by the same brittle mechanism.

In general, the SAC material behaved in a less brittle fashion than FNC, in the nature of the debris collected. All rods that were subjected to symmetric impact exhibited a smooth fracture face many with fragments removed but the deformation here was dominated by the frictional rubbing of the two rods. Further along the rod, bending resulted in brittle fracture in some SAC rods and in most FNC rods. This trend in the materials' behaviour was also exhibited by the classic Taylor samples, where negligible bending observed in high-speed-photography and recovered fragments. Fracture tended to occur in the mushroom and was more prevalent in FNC.

When the impact velocity was increased to  $370 \text{ m s}^{-1}$ , the level of fragmentation observed was similar. However, in both cases both the strain gauges went into compression and bending was not observed until later in the impact process.

When the direction of bend was pre-determined by machining  $45^\circ$  faces onto the two rods, the amount of bending observed was increased, the compressive strain was -8.8 % and the tensile strain was greater than 4 % even though this was the more brittle of the two materials. In this experiment, the onset of bending was earlier than observed in other experiments.

Microstructural examination of the fracture faces showed that rods, which had fragmented along their length tended to exhibit brittle fracture surfaces on which the grains and matrix were clearly seen. Cracks propagated mainly through the matrix. Figure 6.2.8 is an example of a micrograph showing typical intergranular cracking and figure 6.2.9 shows an inter-granular fracture face. Other microscopy provided evidence that some grains had been fractured. In general, SAC rods did not exhibit fracture to the extent found in FNC rods. Both materials exhibited similar microstructural damage near to the impact face with the initially spherical grains distorted and the matrix exhibiting ductile flow. Where fracture occurred, it was by a brittle intergranular mechanism. Figure 6.2.10 shows a pair of rods recovered after a

symmetric Taylor impact at  $299 \text{ m s}^{-1}$ . For a tungsten alloy, it exhibits an enormous plastic deformation without fracture.

Examination of the impact faces showed that a large amount of plastic flow of the matrix had occurred and some of the tungsten grains also appeared to have fused. The impact faces appeared to be similar for both FNC and SAC rods.

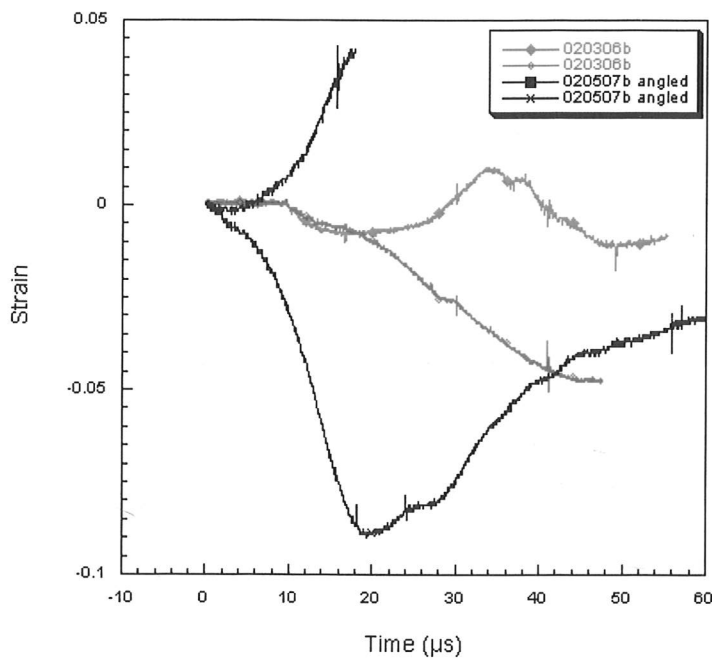


*Figure 6.2.5 Strain histories for two symmetric Taylor tests, one with normal and one with angled faces, impact velocity  $300 \text{ m s}^{-1}$ , on FNC rods.*

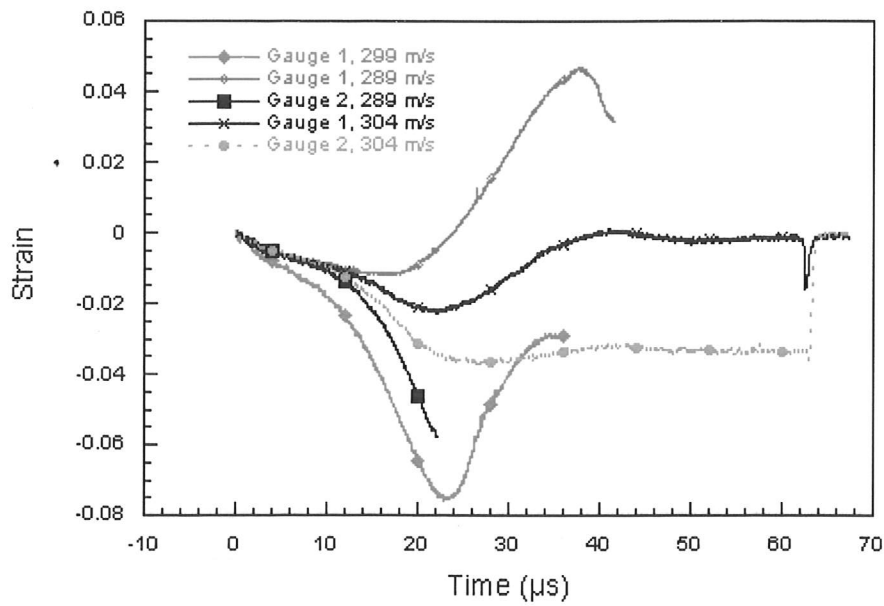


*Figure 6.2.6 Strain histories from two separate symmetric Taylor shots on SAC rods.*

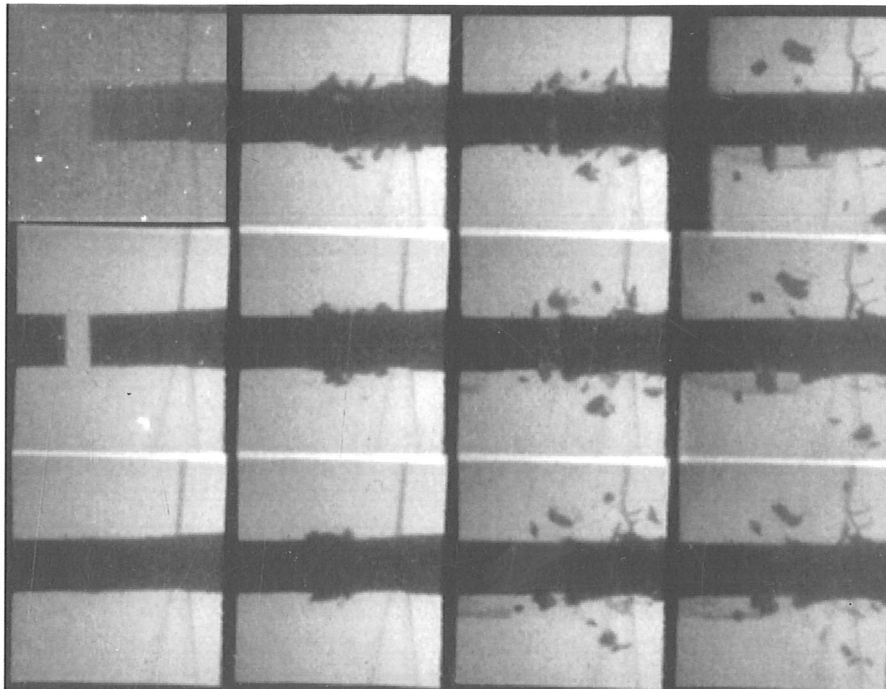


*Figure 6.2.7 FNC symmetric Taylor impact; velocity  $302 \text{ m s}^{-1}$  (shot 020307b). Interframe time  $10 \mu\text{s}$ , exposure  $1 \mu\text{s}$ . The target rod is on the right.*

Shot number	Comments	Material	Offset /rod diameter	Approx. Time to bending ( $\mu$ s)	Maximum strain (%)	Minimum strain (%)
020228a	301 m s <sup>-1</sup>	FNC	0.27	15	3.1	-3.0
020304a	295 m s <sup>-1</sup>	FNC	0.20	15	*	-3.8
020306b	299 m s <sup>-1</sup>	FNC	0.20	25	1.0	-4.8
020307b,	302 m s <sup>-1</sup>	FNC	0.01	>90	2.5	-5.1
020506c	370 m s <sup>-1</sup>	FNC	0.01	>90	-	-
020507b	324 m s <sup>-1</sup> , angled faces on rods	FNC	0.13	10	-	-8.8
020304b	299 m s <sup>-1</sup>	SAC	0.27	10	Gauge failed	-7.5
020306a	289 m s <sup>-1</sup>	SAC	0.16	15	4.7	-5.7
020307a	304 m s <sup>-1</sup>	SAC	0.12	20	0.0	-3.7
020507a	372 m s <sup>-1</sup>	SAC	0.06	35	-2.8	-1.4

\*Both gauges exhibited negative strains. In this instance the gauges were placed on the sides of the rod and not the top and bottom as used in all other shots.

**Table 6.1** The offsets, approximate times to rod bending and extreme values of strain for the symmetric Taylor shots. Positive values of strain means the material is in tension.

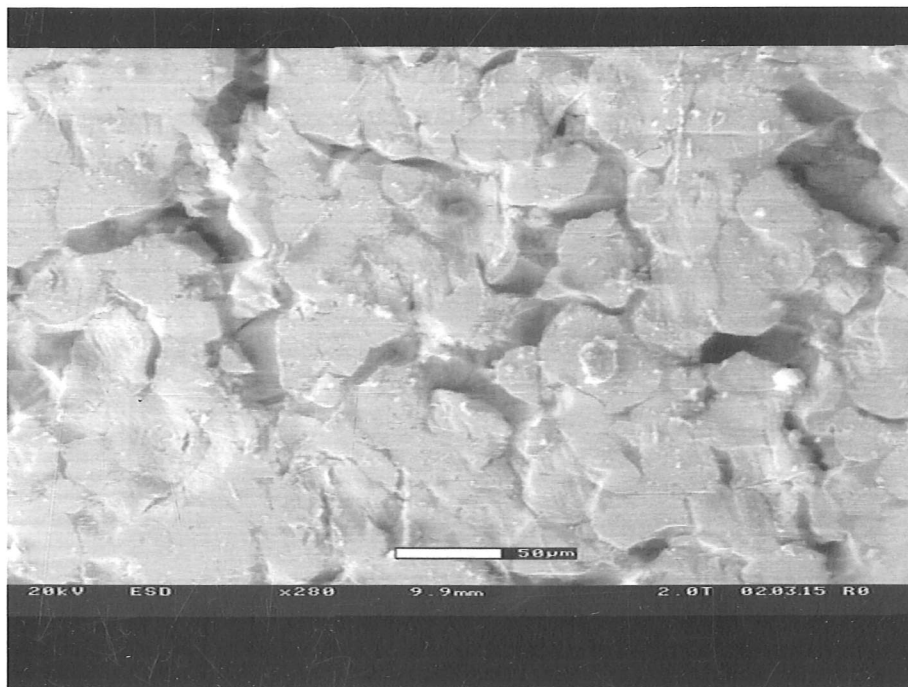


**Figure 6.2.8** Micrograph from a Symmetric Taylor impact of SAC rod, velocity 280 m s<sup>-1</sup>, showing intergranular cracking.

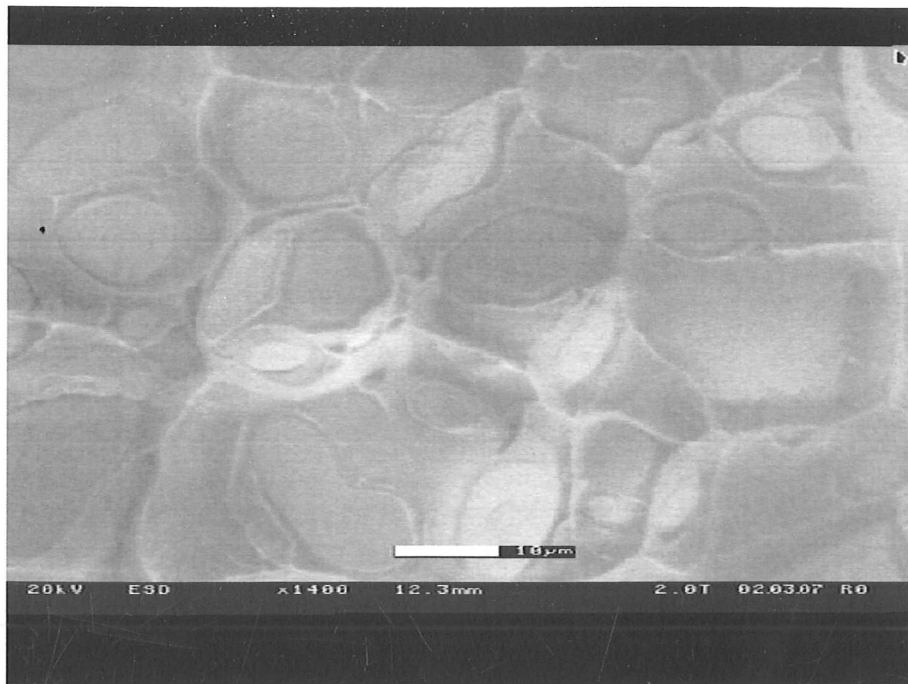


*Figure 6.2.9* Micrograph of brittle fracture face from FNC rod showing intergranular failure, Symmetric Taylor at impact velocity  $301 \text{ m s}^{-1}$  (shot 020228a).

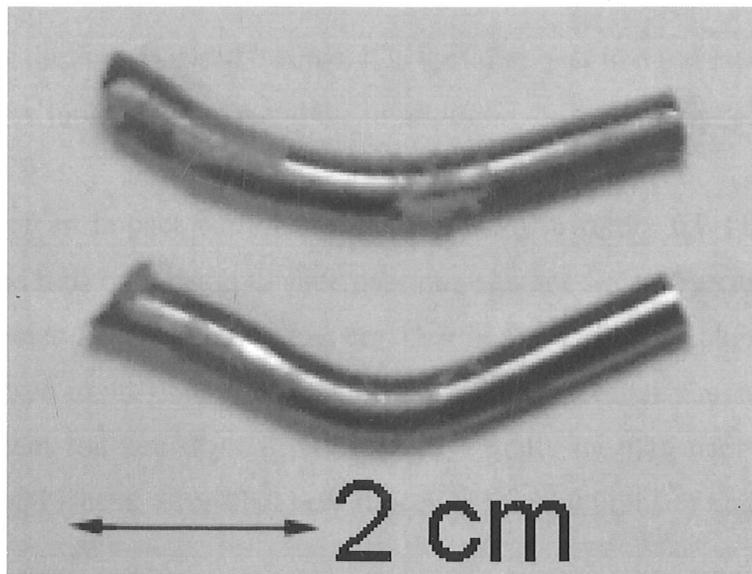


*Figure 6.2.10* Recovered FNC rods following symmetric Taylor impact at  $299 \text{ m s}^{-1}$ .

### (c) Symmetric Taylor tests with angled impact faces

In order to increase the accuracy of alignment of impacts between angled faced rods, a square barrel (internal side 20 mm) was fitted to the smaller of the two gas guns. This prevented rotation of the projectile rod during its passage along the barrel.

All the projectiles used in these experiments had impact velocities of circa  $300 \text{ m s}^{-1}$ . Rods had impact faces with angles of either  $45^\circ$  or  $60^\circ$ . Again some of the target rods were instrumented with strain gauges. Examples of strain traces are given in figure 6.2.10.

The time taken for the stress wave to propagate along the length of a rod, away from the impact face, and be reflected from the other end back to the impact is circa  $20 \mu\text{s}$ . It is difficult to determine this accurately as accounting for the angled impact face is complex. Behind the projectile, there was circa 5 mm of nylon in the projectile. The sabot had been hollowed to reduce mass behind this. Therefore the reflected pulse from this part of the sabot would trail the main longitudinal wave back down the rod by around  $4 \mu\text{s}$ .

When viewing these high-speed records, it is useful to bear in mind that the target rod is the one on the top of the frame and the impactor on the bottom.

An example of an impact with  $45^\circ$  faces is shown in figure 6.2.11. This is well aligned and the rods only begin to slide over one another circa  $12 \mu\text{s}$  after the impact (frame 6). Frames 12 to 14 show some cracking in the impact rod along its axis, this was not observed in previous shots of this kind in this research. Frames 16 onwards show the impact rod actually lost two pieces; usually the fragment lost appeared whole in the high-speed record but here it is clear that the tip itself had fractured and detached.

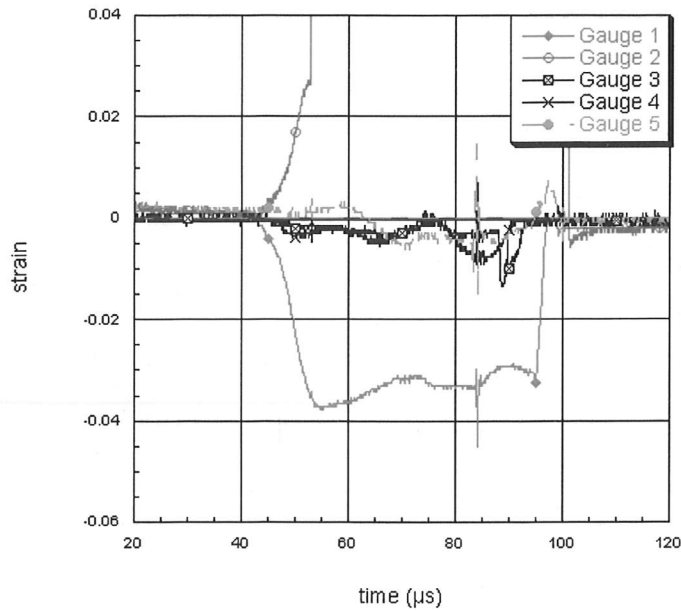
Figure 6.2.12 is a high-speed record of a symmetric Taylor impacts with  $30^\circ$  angles machined on each of the tungsten alloy rods. The fracture and deformation is characteristic of this angle of impacts. It is an excellent overall view of the rods without any detail being obscured by gauges and leads. The tips of the rods can be

seen to break off prior to further fracture. The rods then fracture 2 to 3 diameters of length from their tip, the first part of this fracture travels perpendicular to the axes of the rods and then parallel to, before finally breaking off. The remainder of the two rods is then left in a well-aligned normal symmetric Taylor impact.

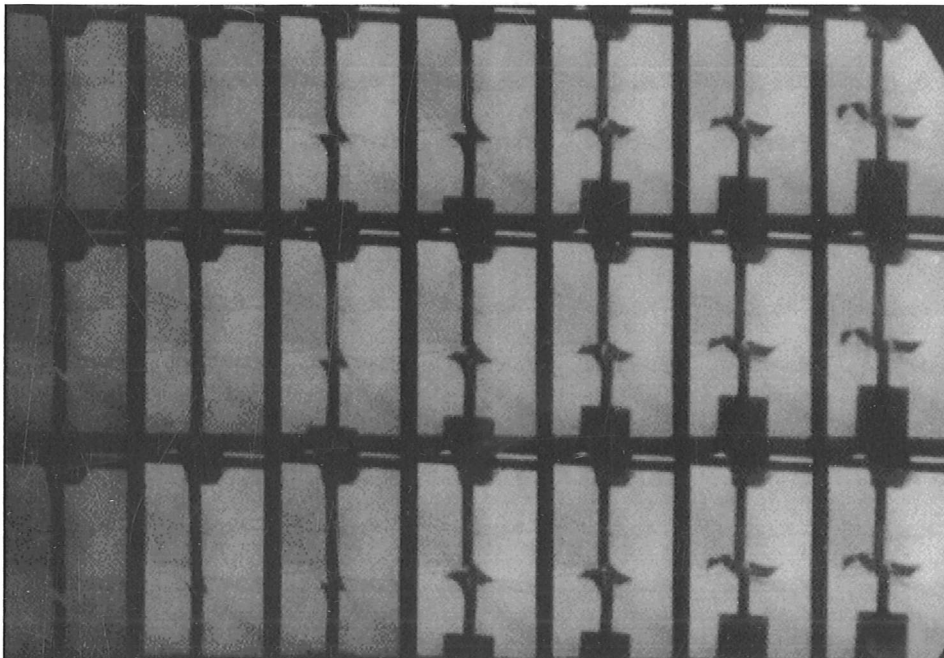
It is interesting to compare the experiments discussed so far with those shown in figures 6.2.13 and 6.2.14. In the former, PMMA rods of identical aspect ratio, with  $45^\circ$  faces were photographed through crossed polarisers that were situated on either side of the chamber. Unfortunately the residual stresses in the windows of the chamber cloud the images somewhat, and any birefringent effects in the PMMA are unclear. However, it does show crack growth rather well. From frame 10, it is clear that crack growth in the target (lower) rod is underway. By frame 12, the fragment begins to leave the rod. Although it is not visible in the high-speed record, the impactor is likely to have shown the same behaviour as the impact proceeds in a fairly symmetrical manner. Frame 17 shows the first indication that the impactor was also cracking radially further down its length. By frame 24, this crack has propagated through the whole diameter and the fragments are beginning to slide over one another.

Figure 6.2.14 is a high-speed record from an experiment in which the PMMA rods had  $30^\circ$  faces. This was much more successful in recording the position of the stress wave within the rod. The polarisers were placed inside the impact chamber in order to eliminate any clouding effects due to the residual stresses in the windows. Full extinction polarisers were used and these proved to be much more effective at looking at changes in the stress state in the rod. Because the exposure time had to be increased to  $1 \mu\text{s}$ , the time resolution of the photographs is not as good. The stress wave was measured to travel away from the impact at  $1.1 \pm 0.1 \text{ mm } \mu\text{s}^{-1}$  in the target rod and  $1.0 \pm 0.1 \text{ mm } \mu\text{s}^{-1}$  in the impact rod. Given the bulk longitudinal sound speed in PMMA is quoted as  $2.72 \text{ mm } \mu\text{s}^{-1}$  and the shear wave speed as  $1.36 \text{ mm } \mu\text{s}^{-1}$  (Marsh 1980), this suggests that we are observing flexural waves. Although the flexural wave speed is not precisely known, this is roughly what would be expected (Kolsky 1963; Ward 1983). There are dark lines travelling back towards the chamfered ends of the rods later in the impact event, these could be release waves from the other end of the

rod. It would be interesting to spend more time analyzing this image. Using a quarter wave plate might further help as any isoclinics could be avoided.



*Figure 6.2.10 Strain gauge traces from shot S030402a, 30° angled faces on FNC rods.*



*Figure 6.2.11 45 degree faces. Shot S030408b. Interframe time 6 μs, exposure 500 ns.*

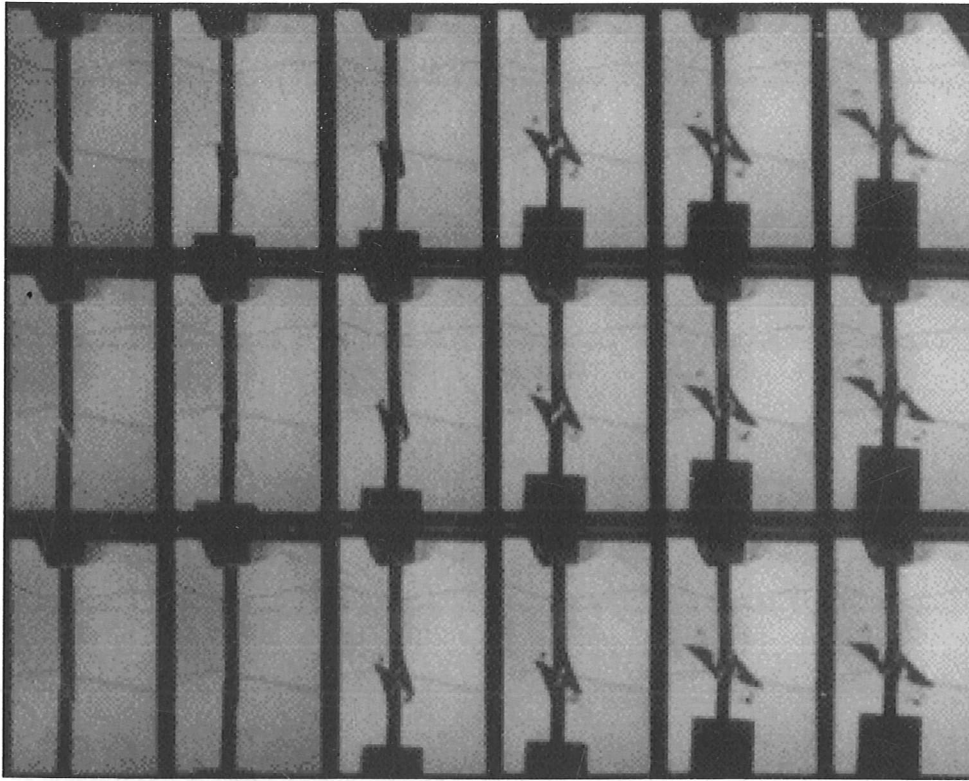


*Figure 6.2.12 30 degree faces. Shot S030408a. Interframe time  $6 \mu\text{s}$ , exposure 500 ns.*

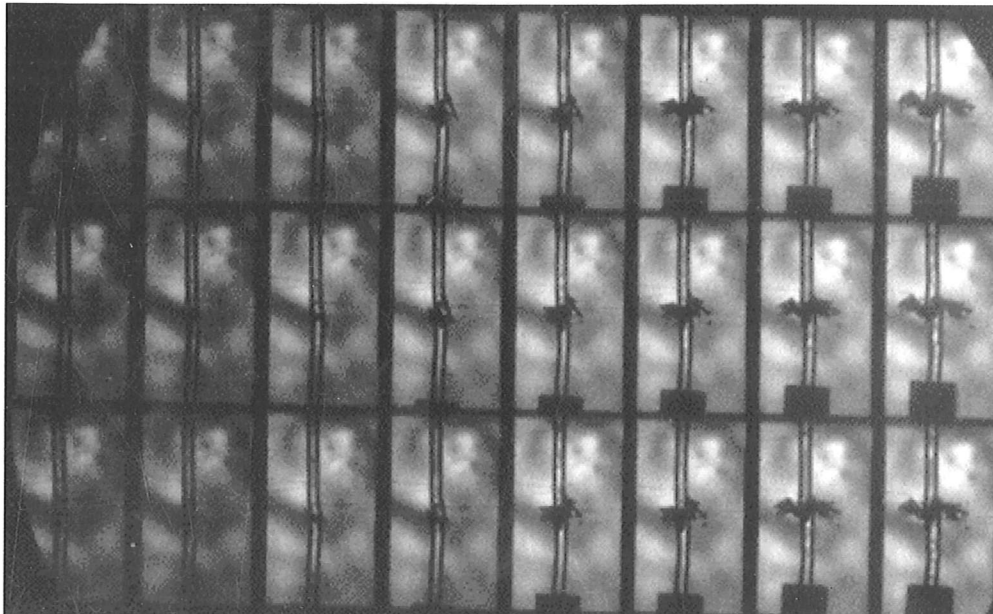


*Figure 6.2.13 PMMA rods, 7 mm diameter, 70 mm length, 45 degree faces. Shot S030409a. Interframe time  $4 \mu\text{s}$ , exposure 500 ns. Viewed through crossed polars.*

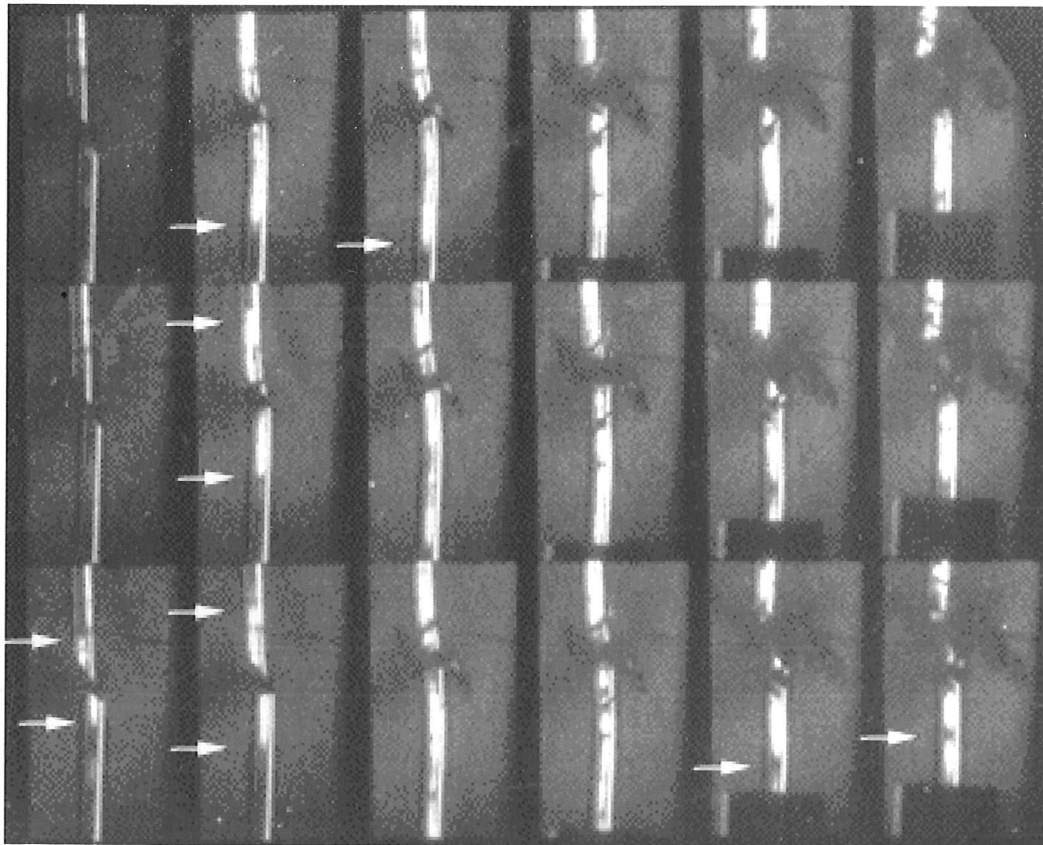


**Figure 6.2.14** PMMA rods, 7 mm diameter, 70 mm length, 30 degree faces. Shot S030409b. Interframe time 4  $\mu$ s, exposure 1  $\mu$ s. Viewed through full extinction crossed polars. Arrows indicate position of flexural waves.

## 6.3 Conclusions

Two sintered tungsten alloys were impacted in both the classic and symmetric impact test Taylor geometries. High-speed photography gives direct visual information on the deformation and fracture processes and gauges recorded the strains at chosen positions on the rods. The amount of strain induced in such brittle materials was surprisingly large, much larger than that induced by quasi-static loading. Strains of nearly 5 % in tension were recorded.

FNC was found to be more brittle than SAC, though microstructural damage mechanisms appeared similar in both materials: The strain histories recorded for symmetric Taylor impact showed compression in the early stages of impact caused by the elastic wave and then bending waves. The magnitude of strains was found to be greater in the SAC (for values, refer to table 6.2.1).

The FNC rods tended to exhibit brittle fracture at these lower strains. SAC exhibited less brittle fracture. Fragmentation of the corners of the mushroom (classic Taylor) and impact face (symmetric Taylor) was more prevalent in the FNC than the SAC samples. The higher impact velocity impacts were not found to dramatically increase fragmentation.

Optical microscopy revealed that both materials exhibited similar microstructural damage. Near to the impact face, the initially spherical grains were distorted and the matrix exhibited ductile flow. Where fracture occurred, it was by a brittle intergranular mechanism.

The geometry for Taylor tests is relatively simple, making them suitable for computer modelling. The data presented in this chapter would be ideal for code validation. There have been many attempts to date, with varying degrees of success. The visual and quantitative deformation and strain data obtained in this research should allow models to be tested and improved.

Generally, the newly designed square section barrel proved to be a success in terms of alignment of these experiments. Fracture and deformation of the two different geometries was recorded using high-speed photography. There were definite preferred places of fracture for each of the two geometries tested. The rods with  $45^\circ$  faces tended to fracture about three rod diameters from their tip. The  $30^\circ$  ones tended to fracture in two places, once about two to three rod diameters from their tip and the other about half way along their chamfered face.

Strain gauges showed that there was very little rod bending outside of the front portion of the rod, this was always released upon fracture. This is indicative of good alignment in the horizontal (perpendicular to the photographs) direction.

Experiments involving PMMA rods of the same geometries were very useful to observe both the cracks but also the propagation of the stress waves. Measured velocities suggested that flexural waves were dominant.

## References

- Bourne, N. K., Z. Rosenberg, J. N. Johnson, J. E. Field, A. E. Timbs and R. P. Flaxman (1995). "Design and Construction of the UK Plate Impact Facility." Meas. Sci. Technol. **6**: 1462-1470.
- Chang, S. N. and J. H. Choi (1997). High strain rate response of a tungsten heavy alloy. APS Topical Group on Shock Compression of Condensed Matter, AIP.
- Furnish, M. D., D. H. Lassila, L. C. Chhabildas and D. J. Steinberg (1995). Dynamic material properties of refractory metals: tantalum and tantalum/tungsten alloys. APS Topical Group on Shock Compression of Condensed Matter, Seattle, Washington, AIP.
- Kennedy, C. and L. E. Murr (2001). "Comparison of tungsten heavy-alloy rod penetration into ductile and hard metal targets: microstructural analysis and computer simulations." Mat. Sci. & Eng. A **A325**: 131-143.
- Kolsky, H. (1963). Stress waves in solids. New York, Dover Publications Inc.
- Marsh, S. P. (1980). LASL Shock Hugoniot Data. Berkeley, California, University of California Press.
- Pappu, E., S. Sen, L. E. Murr, D. Kapoor and L. S. Magness (2001). "Deformation twins in oriented, columnar-grained tungsten rod ballistic penetrators." Mat. Sci. & Eng. A **298**: 144-157.
- Satapathy, S., J. Cazamias, S. Bless, R. Monfredo Gee, L. Meyer and N. Brar (1999). Dynamic strength of tungsten-nickel-cobalt alloys. 11th APS Topical Group on Shock Compression of Condensed Matter, Snowbird, Utah, AIP.
- Ward, I. M. (1983). Mechanical properties of solid polymers, John Wiley & Sons.

## Chapter 7

### Technique Development

This chapter covers areas of research into increasing the stress range over which manganin stress gauges can be used. It is based on (Hammond et al. 2003) but also includes some further research.

#### 7.1 Dependence of measured lateral stress on thickness of protective “padding” around gauges

Measuring both the dynamic lateral and dynamic longitudinal stresses in a material allows calculation of the dynamic shear strength, which is a useful property to take into account when designing armour. Generally, it is thought, the higher the shear strength the better the armour. It is therefore important that a wide range of lateral stress levels can be measured. Previously it has been found that such measurements were not possible above the phase transition in bainitic steels (chapter 5) even with 50  $\mu\text{m}$  mylar padding on either side of the lateral gauges.

With increased protective padding, it was thought that the stress level at the gauge would be reduced. This, therefore, needed to be investigated before further measurements could be carried out.

#### Experimental

The lateral stress measured with a variety of thicknesses of polycarbonate or mylar padding ranged from samples that were entirely mild steel (En3B), to one that was entirely polycarbonate. A projectile velocity of 400  $\text{m s}^{-1}$  was chosen as the resultant pressure in steel is well within the range of the unprotected gauges. The flyer plate on the projectile was 10 mm copper for all experiments discussed here. For these impact conditions, we expect the dynamic longitudinal stress to be around 7 GPa (Millett et al. 1997).

Lateral gauges were embedded within the sample at 2 mm and 5 mm from the impact face as shown in figure 7.1.1. The gauge calibration was taken from (Rosenberg et al. 1980), but also included additional recent correction procedures (Rosenberg and Brar 1995). The thickness of padding around the gauge,  $d$ , represents material on one side, see figure 7.1.1, so that the total padding thickness is  $2d$ .

Other workers (Feng and Gupta 1997) have suggested that the gauge calibration needs to be specific to each material tested. The focus of this chapter however is how the packaging affects the gauge signal in a fixed system.

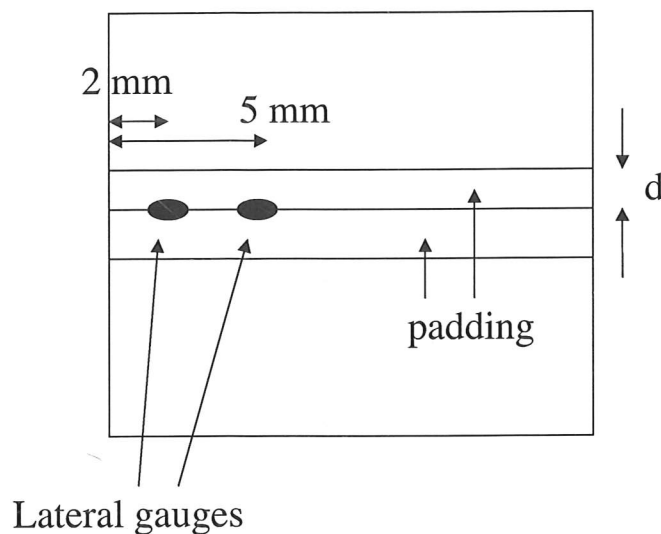


**Figure 7.1.1** Position of lateral gauges within sample. The impact face is on the left in this diagram. The thickness of the padding on each side of the gauge is  $d$  giving a total padding thickness of  $2d$ .

## Results and discussion

One measurement of longitudinal stress, with no padding at these conditions was found to be 7.13 GPa. Figure 7.1.2 shows both the VISAR and longitudinal gauge traces for this experiment. The VISAR trace, having greater time resolution, shows the HEL. The two traces are offset simply because the measurements are taken in different positions, the gauge being embedded in the mild steel and the VISAR being a rear surface measurement. A selection of pairs of lateral gauge traces is given in figure 7.1.3 (note  $\Delta R/R_0$  is given here in order to eliminate any errors in the

interpretation of the gauge output). Each pair is offset on the time axis for clarity. The plateau values of the traces decreases as more padding is incorporated in the sample. Figure 7.1.4 is a plot of  $\Delta R/R_0$  against  $d$ , respectively. There is an initial drop in  $\Delta R/R_0$ , followed by a plateau up to a  $d$  of about 0.5 mm. It is difficult to choose a valid threshold value of  $d$  due to this initial drop.

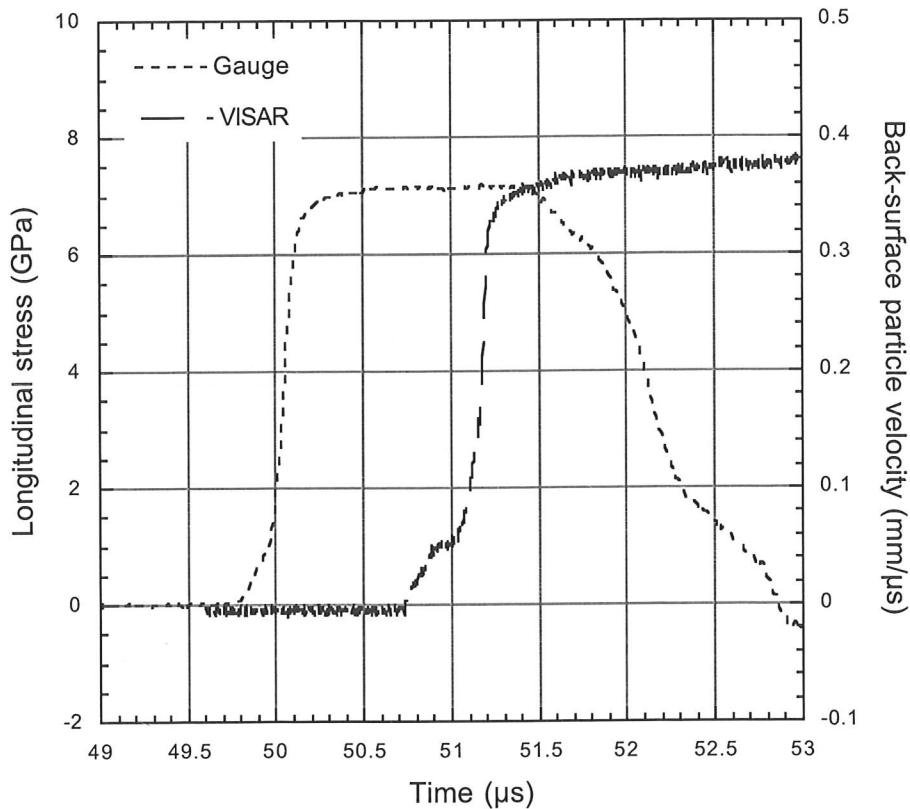


*Figure 7.1.2 Longitudinal gauge and VISAR traces for experiment with zero gauge padding. Impact velocity of  $389 \text{ m s}^{-1}$ .*

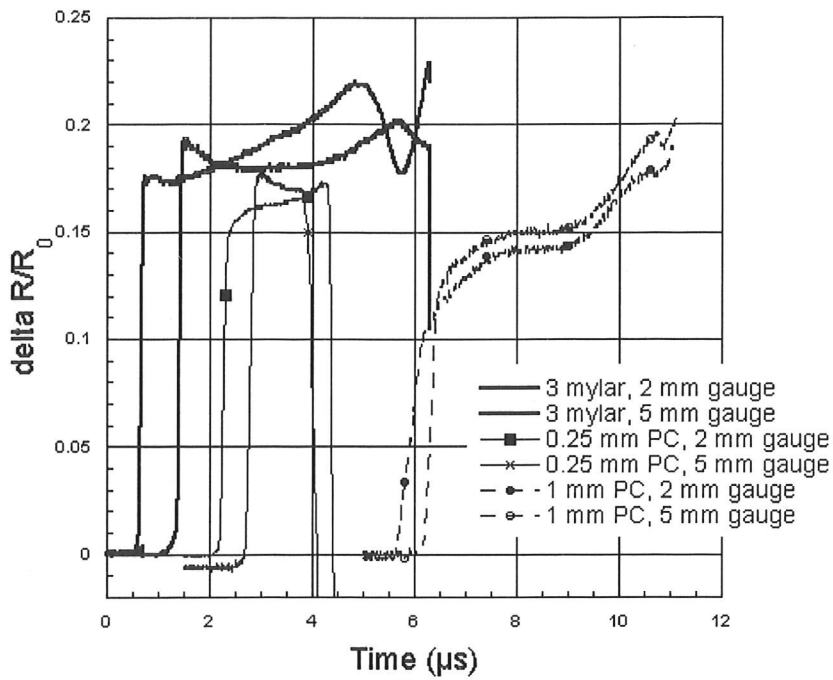


Figure 7.1.3 Lateral gauge traces for a selection of the lateral gauge shots. Note, the traces are offset on the time axis for clarity. Each sheet of mylar is 25  $\mu\text{s}$  thick.

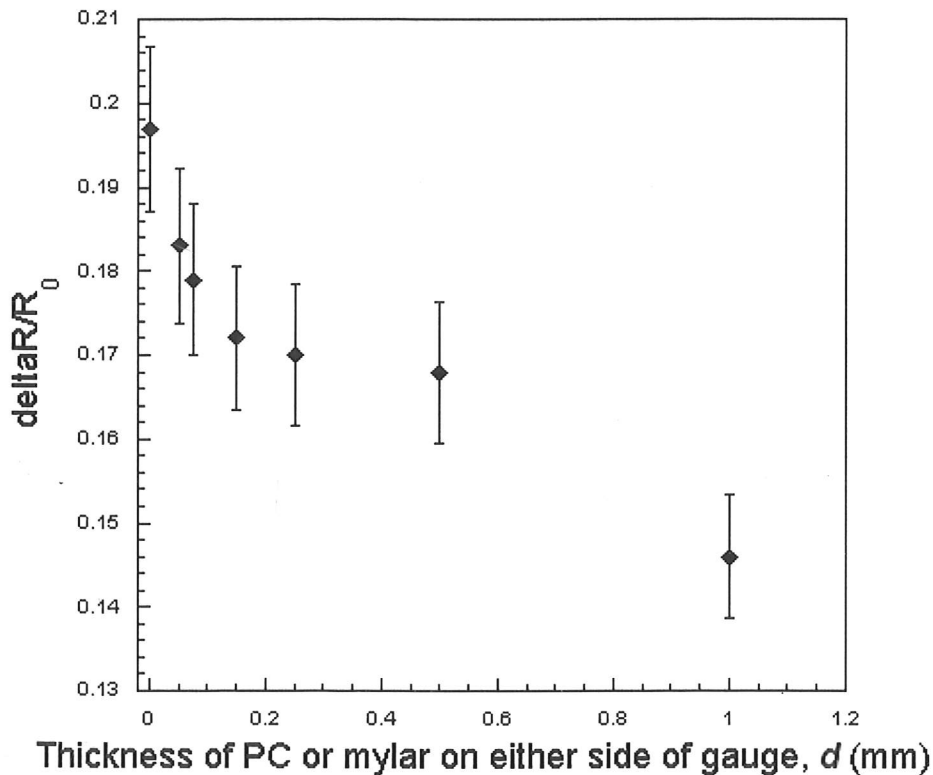


Figure 7.1.4 Plot of  $\Delta R/R_0$  measurements, against padding thickness,  $d$ . Note the lateral stress range here is from 4.5 to 6.5 GPa.

## **Modelling**

The simulation studies were performed using the in-house QinetiQ Eulerian hydrocode GRIM3D. Both this and the model used to represent the lateral gauge are discussed in (Church et al. 2003). The code was able to predict the longitudinal stress to within about 3% of the quoted experimental value, based on VISAR measurements. Prediction of the overall trend of how the lateral stress measured varies with thickness of the packaging agreed with the experimental data. However, the simulations were consistently at least 15% higher than the lateral stresses measured.

## **Conclusions**

The degree of padding obviously does affect the dynamic lateral stress measured and this has been quantified. The research shows that some degree of padding can be incorporated into a test provided that the results are treated with some caution. If this allows higher pressure data to be recorded then that in itself is a step forward.

The survivability of these gauges, both with and without the padding, at higher pressures is discussed in the following section of this chapter.

Values for the lateral stresses from the simulations are consistently higher than the experiment, resulting in a lower value of shear stress. A reason for this might be assumptions made in the model, this will require further research to resolve.

## 7.2 Does this protective “padding” actually improve the survivability of lateral gauges?

Experiments were carried out under higher stress impact conditions. A value of 0.5 mm was chosen for the padding thickness,  $d$ . Initially, 6 mm copper impactors were used at velocities of 854 and 900 m s<sup>-1</sup>. The longitudinal stresses expected for these impact conditions on mild steel are circa 15 and 17 GPa respectively. Lateral gauges survived sufficiently well to give a useful trace in both of these experiments (figure 7.2.1).

In order to achieve even higher stresses, one experiment was carried out at 943 m s<sup>-1</sup> using a 5 mm tungsten alloy impactor. This gives impact conditions of around 27 GPa of longitudinal stress. Again the gauge appeared to yield a valid trace, pairs of traces are given in figure 7.2.1, these have been offset along the time axis for clarity.

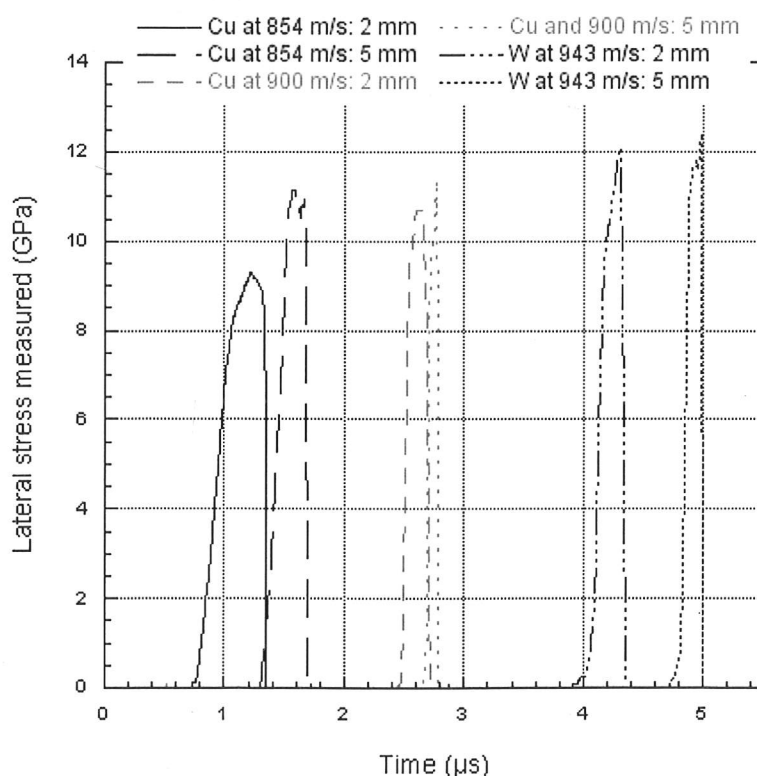


*Figure 7.2.1 Lateral gauge traces from study on survivability. Note the timescales have been shifted for clarity.*

## **Discussion and conclusions**

There is normally an error of  $\pm 10\%$  associated with using these gauges. Pairs of traces from the same experiment are consistent with one another within this large experimental scatter. This indicates that the gauges are measuring something particular rather than yielding random values. However, when the longitudinal stress is as high as 27 GPa, the mild steel should be a lot nearer hydrodynamic behaviour than it appears to be. If a material is in a hydrodynamic regime, it has no strength, given the shear strength of the material is equal to half the difference between the longitudinal and lateral stresses, the longitudinal and lateral stress measured should be equal. Clearly, in this research the material isn't close to hydrodynamic behaviour at 27 GPa longitudinal stress. Turning to the modelling, using the same set up as discussed briefly in section 7.1, the mild steel is predicted to be almost hydrodynamic at a longitudinal stress of 27 GPa. Perhaps the gauges are not in fact reaching a stable level. It is unclear from the traces if this is the case.

The gauges have been surviving reliably at much higher pressures than they had without this additional padding. The resulting stress measured is not what would be predicted in the mild steel. Further modelling needs to be undertaken in order to interpret the stress that is measured in terms of the mild steel response.

## References

- Church, P. D., A. Grief, K. Tsembeles, W. G. Proud and N. H. Murray (2003).  
Experiment and simulation of the lateral gauge in glass targets. APS, Portland, Oregon.
- Feng, R. and Y. M. Gupta (1997). "Determination of lateral stresses in shocked solids: Simplified analysis of piezoresistive gauge data." J. Appl. Phys. **83**(2): 747-753.
- Hammond, R. I., P. D. Church, A. Grief, W. G. Proud and J. E. Field (2003).  
Dependence of measured lateral stress in thickness of protective "padding" around gauge. APS, Portland, Oregon.
- Millett, J. C. F., N. K. Bourne and Z. Rosenberg (1997). An investigation of the alpha-epsilon phase transition in shock loaded EN3 mild steel. APS Topical Group on Shock Compression of Condensed Matter, AIP.
- Rosenberg, Z. and N. Brar (1995). "The influence of the elasto-plastic properties of piezoresistive gauges on their loading-unloading characteristics as lateral shock stress transducers." J. Appl. Phys. **77**(4): 1443-1448.
- Rosenberg, Z., D. Yaziv and Y. Partom (1980). "Calibration of foil-like manganin gauges in planar shock wave experiments." J. Appl. Phys. **51**(7): 3702-3705.

## Chapter 8

### Conclusions and further work

This dissertation presents data relating to both the shock and ballistic properties of bainitic steels and reports the dynamic behaviour of two sintered tungsten alloys. By studying material properties over a wide range of strain rates, a greater understanding of its behaviour can be found. Shock data can be used in simple models which can subsequently be extended to cover the more complex three-dimensional situations than might be encountered in ballistics experiments.

The shock properties in compression, both longitudinal and lateral, and tension of two bainitic steels have been measured. The Hugoniot and shear strengths of the two bainites were found to be similar to those of mild steel. The HEL of the lower temperature and upper bainites was found to be  $3.5 \pm 0.5$  GPa and  $2 \pm 0.5$  GPa respectively. Lower temperature bainite was found to have a phase transition at  $13 \pm 0.5$  GPa. The phase transition was not observed for the upper bainite.

The dynamic tensile or spall strength of a material generally influences the performance of that material in an armour application. It was therefore important to measure these values given the bainites are under consideration as armour material. The spall strength of the lower temperature bainite was about 1.9 GPa across the stress range considered here. The spall strength of the upper bainite was found to be about 2 GPa below the phase transition stress. However, above this stress level it dropped significantly. The reason the phase transition is suppressed or non-observable for one bainite and not the other is almost certainly explained by the microstructural differences between the two forms of bainite. Microhardness traverses were carried out on recovered material and it was found that the pressure of the shock wave has more effect than its duration on the microhardness. Further microstructural work, X-ray diffraction, microscopy and hardness testing, could look for an explanation of the suppression or non-observation of the phase transition.

A material very similar to the low temperature bainite considered earlier in this research was compared to both RHA steel and mild steel in ballistic experiments. The tests involved unconstrained plates and depth of penetration studies. The RHA steel failed by plugging in the unconstrained plate set-up, the bainite also showed signs of plugging. The mild steel failed either by spall or plugging and was certainly not shown to be suitable as an armour material. The main difference between the other two materials is the bainite exhibited a lot of fracture after impact whereas the RHA steel was deformed plastically. The depth of penetration tests did not show the differences between the materials to be particularly significant. Future research is needed at full ballistic velocities in order to determine which material is most suitable for an armour application.

Classic and symmetric Taylor tests were carried out on two sintered tungsten alloys in order to try to characterise their behaviour under dynamic loading. This in turn, helped the interpretation of the ballistic experiments. Surface tensile strains of up to 5 % were recorded. Optical microscopy revealed that the initially spherical grains were distorted and the matrix exhibited ductile flow. Any fractures occurred by a brittle intergranular mechanism.

The final experimental chapter in this dissertation describes research into developing the techniques already used in gauge technology. By addition of extra "padding" around a lateral gauge, the survivability is increased. Measurements of lateral stress can be extended into stress ranges not considered before. However, this extra "padding" affects the stress that is recorded at the gauge. This effect has been quantified.

Research of the type described in this thesis is costly; it uses expensive equipment such as high-speed cameras, VISAR and the plate impact facility. Each experiment has involved a number of expensive consumables as well as a lot of time. Therefore the series of tests described in this work have been kept to a realistic minimum. However, the costs are relatively modest when compared with full-scale ballistics trials. An attraction of the data, are that they are in a form which modellers can use. Once models are satisfactory, a small number of full-scale ballistics trials can be

carried out. Overall costs are minimised by a co-ordinated program of experiments and modelling.

There are clearly a few unanswered questions remaining. The absence of a detectable phase change for one of the bainitic steels is one. The "gap" between experiment and modelling with the "padded" gauges is another. However, the quantities of material available for making samples were restricted since our immediate sponsor themselves had budget restraints.

Clearly, more samples for future studies would help, and certainly more of the upper bainite would enable a deeper investigation into the phase change.

This thesis shows that the bainites have attractive properties for ballistic applications and it is hoped that the present dissertation will stimulate further research.